THESIS

END-GAS AUTOIGNITION PROPENSITY AND FLAME PROPAGATION RATE MEASUREMENTS IN LASER-IGNITED RAPID COMPRESSION MACHINE EXPERIMENTS

Submitted by

Andrew Zdanowicz

Department of Mechanical Engineering

In partial fulfillment of the requirements

For the Degree of Master of Science

Colorado State University

Fort Collins, Colorado

Summer 2019

Master's Committee:

Advisor: Anthony Marchese

Bret Windom
Greg Hampson
Ken Reardon

ABSTRACT

END-GAS AUTOIGNITION PROPENSITY AND FLAME PROPAGATION RATE MEASUREMENTS IN LASER-IGNITED RAPID COMPRESSION MACHINE EXPERIMENTS

Knock in spark-ignited (SI) engines is initiated by autoignition and detonation in the unburned gases upstream of spark-ignited, propagating, turbulent premixed flames. Knock propensity of fuel/air mixtures is typically quantified using research octane number (RON), motor octane number (MON), or methane number (MN; for gaseous fuels), which are measured using single-cylinder, variable compression ratio engines. In this study, knock propensity of SI fuels was quantified via observations of end-gas autoignition (EGAI) in unburned gases upstream of laser-ignited, premixed flames at elevated pressures and temperatures in a rapid compression machine. Stoichiometric primary reference fuel (PRF; n-heptane/isooctane) blends of varying reactivity ($50 \leq \text{PRF} \leq 100$) were ignited using an Nd:YAG laser over a range of temperatures and pressures, all in excess of 545 K and 16.1 bar. Laser-ignition produced outwardly-propagating premixed flames. High-speed pressure measurements and schlieren images indicated the presence of EGAI. The fraction of the total heat release attributed to EGAI (i.e., EGAI fraction) varied strongly with fuel reactivity (i.e., octane number) and the time-integrated temperature in the end-gas prior to ignition. Flame propagation rates, which were measured using schlieren images, did not vary strongly with octane number but were affected by turbulence caused by variation in piston timing. Under conditions of low turbulence, measured flame propagation rates agreed with the theoretical premixed laminar flame speeds quantified by 1-D calculations performed at the same conditions. Experiments were compared to a three-dimensional CONVERGE$^{\text{TM}}$ model with reduced chemical kinetics. Model results accurately captured the measured flame propagation rates, as well as the variation in EGAI fraction with fuel reactivity and time-integrated end-gas temperature. Model results also revealed low-temperature heat release and hydrogen peroxide formation in the end-gas upstream of the propagating laminar flame, which increased the temperature and degree of chain branching in the end-gas and ultimately led to EGAI.

ACKNOWLEDGEMENTS

Dr. Anthony Marchese, thank you for your limitless patience, reciprocated respect, and persistent encouragement. Your passion for the sciences has been energizing, while your hands-off management style has allowed me to grow and think for myself. In pressing times, you always offer a well-adjusted perspective and it is clear that you have the best interests of your students in mind. I could not have asked for a better advisor and am forever grateful.

Dr. Bret Windom, Dr. Greg Hampson, and Dr. Ken Reardon, your expertise and guidance are invaluable. Thank you for agreeing to take on the responsibilities that come with serving on my advisory committee. Dr. Jessica Tryner, I can only hope that I have absorbed some of your clarity, intensity, and attention to detail. Thank you for your kindness and continuous support.

Jeff Mohr, your role in this work was substantial. Thanks for being my voice of reason and for offering your empathy as someone else who deals with the frustrations of working with the RCM on a daily basis. Colin Gould, a big thanks is also owed to you for showing me the ropes. Kara Gustafson, thank you for spending countless hours helping me gather experimental data and performing all of the monotonous tasks that I did not want to do myself. I know you'll be successful with whatever you set out to do.

Siddhesh Bhoite, Dr. Ciprian Dumitrache, Andrew Boissiere, Dr. Marc Baumgartner, and everyone else who came before me, this research would not have been possible had it not been for your hard work and ingenuity. Thank you.

Last, to the many lifelong friends that I have made throughout my time in Colorado, I would not have made it alone. Thank you for being my support system – helping me to maintain my sanity and find balance in life.

DEDICATION

To my parents. Your hard work built the foundation of my opportunity. Thank you for your unwavering support, even when I wanted to quit.

TABLE OF CONTENTS

LIST OF TABLES

LIST OF FIGURES

CHAPTER 1 – INTRODUCTION

1.1 Motivation

Driven by increasingly stringent emissions regulations and customer performance expectations, the internal combustion engine (ICE) industry has collectively explored means of maximizing thermal efficiency and cleanliness of combustion systems for decades. These initiatives have been foremostly limited by the onset of engine knock in spark-ignited (SI) engines. Most broadly, engine knock is the severe manifestation of end-gas autoignition (EGAI) – a phenomenon characterized by uncontrolled ignition of the unburned premixed "end-gases" ahead of the propagating flame [1]. Knock is capable of causing severe engine damage over time and, as such, is commonly avoided to the detriment of efficiency. Continued advancement of SI engine performance, efficiency, and emissions requires the development of a more thorough understanding of, and established control over, the EGAI processes that govern knock.

There are two competing initiatives in the design of any combustion system. The first is to achieve consistent, predictable, controlled combustion – converting the fuel's chemical energy into heat/work. The second is to maximize the thermal efficiency of that energy conversion processes. A tradeoff exists between these initiatives in ICEs, as the conditions most favorable to higher thermal efficiencies are also those most conducive to abnormal combustion phenomena. Abnormalities in the combustion behavior, like EGAI, impede efforts of achieving predictable energy conversion and can initiate further abnormalities (e.g. local autoignition can cause secondary autoignition events in adjacent sites). Such behavior results in the breakdown of the thermal boundary layer that ordinarily protects in-cylinder components from exposure to combustion radical species and extreme temperatures, leading to surface corrosion, overheating, and potential part failure with time [1,5].

To better understand the EGAI governing phenomena, the simplified case of a homogenous reactive gas mixture at constant elevated temperature is considered. For any such mixture, there exists a finite period over which slow initial chain-propagation reactions transition into exponentially faster chain-branching reactions that constitute combustion [2]. This period is termed the "critical chemical kinetic induction period" and represents an ignition delay such that, if the reactive mixture is held at the elevated state for this period of time, it will autoignite and volumetrically combust. Expanding the case to account for transient thermodynamic conditions, Livengood and Wu suggested that autoignition will occur if the time integrated, inverse induction period reaches unity – see Equation 1 [3].

$$Autoignition\ Condition\colon\quad \int \frac{1}{\tau}\, dt \;\; \geq \;\; 1 \tag{1}$$

Here, τ is the induction period for the instantaneous thermodynamic and reactive state at time t and is a most strongly a function of the activation energy of the reactive mixture and the temperature at a given instant.

Many factors control the induction period in a real engine. Not only do the operating conditions of the engine (e.g. speed, load, boost pressure) influence the state of the unburned gases, but so do the combustion characteristics of the spark-ignited flame itself. As the spark-ignited premixed flame propagates away from the ignition site, it compresses and heats the unburned end-gases upstream, thereby affecting their critical induction period and potentially leading to autoignition. Add to that the influence of cooling brought about by the expansion stroke, heat transfer to the chamber walls, and uncontrolled potential ignition sources (e.g. residual gases, oil droplets, and thermal hotspots [4,5]), and the question of whether autoignition will occur in the end-gas becomes challenging and convoluted.

Two conventional avenues for establishing control over EGAI and knocking events exist for SI engines. One is reactionary, in which engine control systems identify knock with onboard diagnostics and make the necessary changes to the operating conditions to mitigate knock. That is, if a knock event is detected, the spark timing is retarded (most common), the boost pressure is decreased, or the air/fuel ratio is increased [1]. These changes inherently sacrifice engine performance in favor of reliability. The other avenue for knock mitigation and control is proactive, in which a fuel's suitability for a given engine configuration and set of operating conditions is assessed with a knock propensity metric - octane, cetane, and methane numbers [6–8]. These knock propensity metrics, their measurement, and the potential to improve upon them will be the central focus of this thesis.

1.2 Fuel Reactivity Metrics – Measurement Standards and Shortcomings

The conventional quantifications for the propensity of a liquid SI fuel to autoignite are the research and motor octane numbers (RON and MON) [6,7]. RON and MON describe a fuel's resistance to knock and thus determine its suitability for a given engine and set of operating conditions. They represent a comparison of the tested fuel's combustion characteristics to those of a reference fuel blend of which the combustion properties are well known. The comparison is focused on the fuel's critical compression ratio (CR), defined as the CR at which "incipient" knock is detected in a variable compression ratio engine under standardized operating conditions. These tests are carried out in purpose built, single-cylinder, variable compression ratio Cooperative Fuels Research (CFR) engines.

The primary reference fuels (PRFs) isooctane (C_8H_{18} – 2,2,4-trimethylpentane), a common surrogate for gasoline, and n-heptane (C_7H_{16}), a common surrogate for diesel fuel, are blended in varying proportion to provide a range of fuel reactivity and knock propensity for comparison with the test fuel. Isooctane is the lesser reactive of the PRFs and in its pure form serves as the upper limit of the octane number scale; liquid isooctane has an octane number (ON) of 100. Pure n-heptane serves as the lower limit on the other end of the scale with an ON of 0. PRF blends are denoted by a PRF number, such that the mole fraction of isooctane in the fuel blend is given and the n-heptane making up the remaining fraction is implied (e.g. PRF 80 is comprised of 80% isooctane and 20% n-heptane by volume). It follows that the octane number for a PRF blend is the same as its PRF number (e.g. PRF 80 has an octane number of 80), and the PRF blend that exhibits the same critical compression ratio as the test fuel in the CFR engine designates the test fuel's octane number.

ASTM standards specify the CFR engine operating conditions at which the critical compression ratios are measured for the RON and MON metrics [6,7]. The RON and MON metrics target specific end-gas conditions and together provide a representation of a test fuel's knock propensity in a typical SI engine. RON is measured at an engine speed of 600 RPM with an intake air temperature of 52 ˚C and a constant ignition timing of 13˚ before top dead center (BTDC). MON is measured at 900 RPM at 38 ˚C with variable ignition timing, mapped to the compression ratio.

Despite their apparent similarities, there is no direct correlation between the two metrics, as they represent distinct end-gas conditions spanning the negative temperature coefficient (NTC) region of hydrocarbon fuels [9]. Ordinarily, the ignition delay of a reactive gas mixture will become shorter with increasing temperature. NTC regimes are characterized by a reversal of this trend, in which ignition delays will in fact become longer with increasing temperature [2,10]. This is accepted to be the result of low-temperature chemistry (LTC) that volumetrically produces combustion radical species such as formaldehyde (CH_2O) and hydrogen-peroxide (H_2O_2) which are more stable at the temperatures in the NTC regime. The RON and MON metrics are designed to account for the NTC regimes as they can be influential to the onset of EGAI for a given end-gas state. It is important to consider that fuels which do not exhibit substantial NTC behavior will have nearly identical RON and MON, such that their sensitivity (S), defined by Equation 2 is near zero [11].

$$S = RON - MON \tag{2}$$

It is common practice to combine RON and MON in weighted proportion to account for sensitivity and best represent how a test fuel will behave in a real engine. In the United States, the posted octane number at gas filling stations is simply the average of the RON and MON [11]. Elsewhere, only the RON is reported.

Further complicating the matter, MON may be an outdated metric altogether, as it seems to be a weak predictor of a fuel's knock propensity for modern SI engine platforms [9,12]. Modern engines subject fuels to more extreme in-cylinder conditions relative to what is represented by the MON standard. In an extensive review of modern engine performance on a range of fuels of varying reactivity, Kalghatgi et. al. found that under certain operating conditions, using fuels of higher MON reduced the knock-limited spark advance (KLSA) of the tested engine [9,11,12]. Such a result implies that the performance of the engine is increasingly limited by knock with increasing MON of the fuel - the opposite trend of what the metric is supposed to represent. Kalghatgi proposes the use of an octane index (OI) instead (Equation 3 below) to better predict a fuel's combustion behavior for a given engine [9]:

$$Octane\ Index = RON - kS \tag{3}$$

Here, the sensitivity (S) of the fuel is multiplied by an engine specific constant k, that effectively adjusts the relative weight of the RON and MON metrics to best predict a fuel's knock propensity for a given engine configuration and set of operating conditions.

Despite these improvements, there exists demand for a knock propensity metric that can be measured without the use of an engine. Efforts to produce novel fuels typically yield very small, costly quantities, of which little is known about their pertinent combustion properties. Measurement of the fuel's octane number at an early stage development would be prohibitively expensive due to the amount of fuel that would be required to run the engine. Further, CFR engines are far from the ideal instrument to conduct fundamental combustion studies. Given the complexity of the system, it is difficult to isolate the chemical kinetics from the other thermal, fluid, and mechanical factors governing combustion. Benchtop cetane number (CN) measurement instruments, like the ignition quality tester (IQT) and the fuel ignition tester (FIT), have been developed in response [14,15], but an alternative standardized method for measuring ON has yet to be developed [12,16–18].

1.3 Knock Propensity Measurement Potential of a Rapid Compression Machine

A rapid compression machine (RCM) has several advantages as an instrument for studying EGAI and measuring knock propensity through alternative means. An RCM (1) can safely reach a variety of temperatures and pressures consistent with end-gas conditions in current and future engines, (2) requires substantially less fuel than engine testing, (3) is optically accessible, and (4) can be more accurately modeled than an internal combustion engine because of precise knowledge of the initial conditions and the absence of turbulent flow [13,14].

Qi et al. used a single-piston RCM to examine conventional knock and superknock of a stoichiometric isooctane/air mixture at three different compression ratios using a conventional j-gap spark plug [15]. More recently, Dumitrache et al. [16] developed a technique to produce laser-generated sparks in an RCM. After compression to elevated temperatures and pressures, the laser spark initiates ignition and produces an outwardly propagating flame. Bhoite [14] performed CFD computations of the laser-ignited methane/air experiments of Dumitrache et al. [16] with detailed chemical kinetics and also predicted the presence of EGAI for computations performed with PRF fuels.

1.4 Objectives and Overview

The objective of this thesis is to advance methods for quantifying the EGAI propensity of SI fuels. This is done by observing EGAI in the unburned gases upstream of laser-ignited, premixed flames at elevated pressures and temperatures in an RCM. PRF blends of varying reactivity ($50 \leq ON \leq 100$) were ignited by a laser spark in a dual-piston RCM. High-speed pressure measurements and schlieren images were used to characterize the combustion processes, approximate flame speed, and quantify the magnitude of potential EGAI events. To elucidate the underlying phenomena that lead to EGAI and develop a better understanding of the experiment, results were compared to transient, three-dimensional computational models with detailed chemical kinetics developed using CONVERGE^{TM}.

As an overview of this document, Chapter 2 provides a detailed description of the experimental apparatus and its associated equipment. Chapter 3 covers the methods behind the utilization of the laser-ignited RCM platform as a means to study SI combustion phenomena. Here, the alternative metrics developed to quantify EGAI magnitude are also introduced. Chapter 4 describes the construction of the three-dimensional CFD models and their verification. Chapters 5 and 6 present the findings of the experiments and simulations, inclusive of discussion of the validity of the methods employed and a detailed interpretation of the results. Finally, the RCM's aptitude as a knock propensity measurement instrument is reviewed in Chapter 7, along with the offering of recommendations for future work.

CHAPTER 2 – EXPERIMENTAL EQUIPMENT AND INSTRUMENTATION

All work presented in this thesis was performed at the Powerhouse campus of Colorado State University's (CSU's) Engines and Energy Conversion Laboratory (EECL). The Powerhouse hosts a variety of research initiatives, mostly centered on clean and efficient power generation and use. The CSU rapid compression machine (RCM), with which all of the experimental data in this work was collected, situates itself as one of CSU's primary instruments for performing fundamental combustion studies. This chapter is dedicated to describing the RCM and its associated equipment, while Chapter 3 expounds the orchestration of the systems and how they are used to measure EGAI propensity.

2.1 Rapid Compression Machine

The CSU RCM is a unique dual-piston machine that was manufactured by Marine Technology, LTD of Galway, Ireland. It was purchased and installed in 2014 in the Combustion and Laser Sensing Laboratory of the Powerhouse. The machine is capable of achieving compression ratios of 11.8:1 in under 15.0 ms while minimizing the fluid dynamic disturbances associated with compression.

The system is composed of two hydraulic-pneumatic drive cylinder assemblies that face each other and provide the compressive force, as shown in Figure 1. The two cylinders are electronically coupled and share the same high-pressure air and hydraulic source lines. The compressive force is provided by high-pressure air bellows on the backsides of the piston/plunger assemblies and the timing of compression is controlled through the release of the hydraulic locks that keep the pistons in their retracted positions prior to compression.

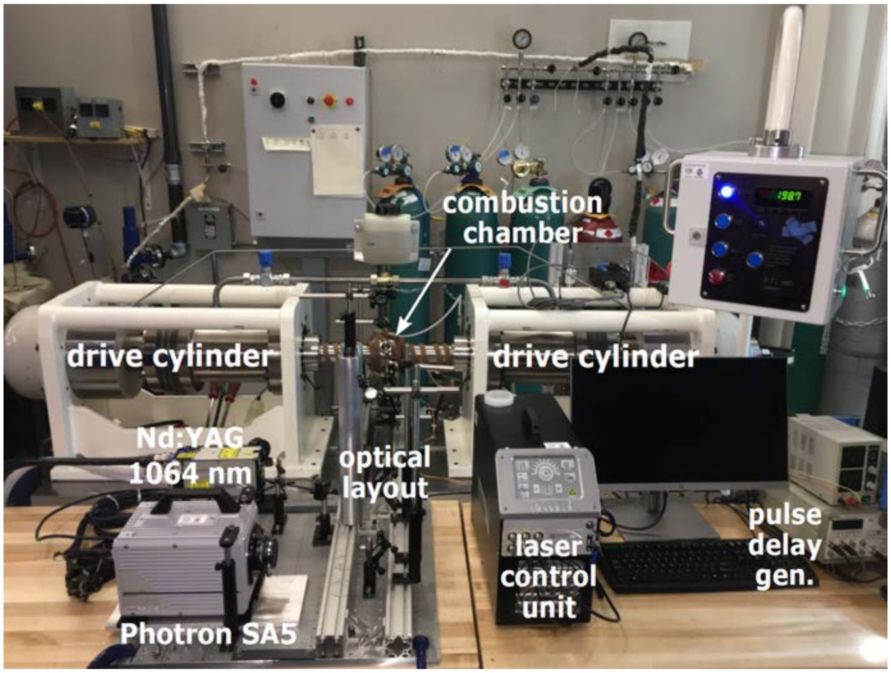

Figure 1. Picture of the rapid compression machine and associated equipment in the experimental setup.

Central to the RCM's value as a research instrument are its creviced pistons. Represented graphically in Figure 2, these pistons feature a T-shaped profile with a secondary "crevice volume" on the backside of the piston face that is connected to the main chamber via a narrow channel on the outside periphery of the piston. To understand their function, the dynamics of a normal flat-faced piston must first be considered (also featured in Figure 2). In the theoretical case in which a contained gas mixture remains perfectly homogenous throughout compression and piston motion is much slower than the mean velocity of the average gas molecule, closed-chamber compression with a flat piston would result in a higher packing density with no significant increase in turbulence level. However, inhomogeneities do arise during real-world compression events due to transient temperatures and the thermal boundary layer that develops adjacent to the chamber wall. This cool boundary layer is collected by the moving flat piston and redirected into the core gas volume via convection, producing a "roll-up" vortex that causes heavy turbulence [17]. In contrast, the narrow channel on the outer rim of the creviced piston allows the thermal boundary layer to pass into the crevice volume during compression, effectively avoiding roll-up vortex formation and mitigating fluid dynamic disturbances.

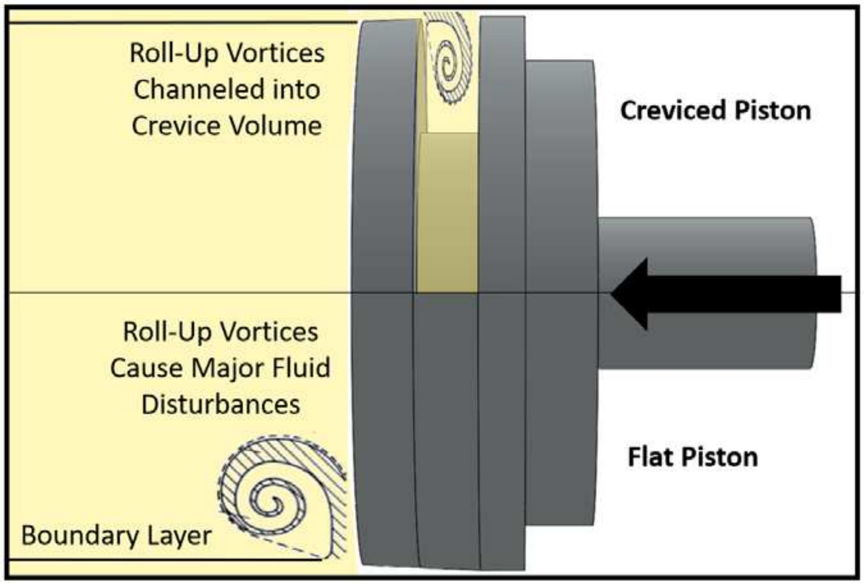

Figure 2. Illustration of creviced and flat piston designs. Piston profile is split to facilitate comparison between the two designs. The thick outer box represents the cylinder sleeve and the piston motion is depicted by the black arrow. The compressed gases are shown in yellow and the atmoshpheric gases are shown in white.

The creviced piston design lends itself particularly well to the RCM's *homogeneous autoignition mode*, wherein autoignition is achieved without an external ignition source. In homogeneous autoignition mode, initial conditions are typically selected such that the fuel-oxidizer mixture autoignites within 5 to 200 ms after the end of compression. Creviced pistons minimize disturbances in the compressed volume and thereby allow for the "adiabatic core" assumption to be made [17]. That is, the compressed core has minimal temperature gradients and approaches a 0D condition. These tests are mostly focused on measuring ignition delay period using high speed pressure data.

The CSU RCM can also operate in *laser-ignition mode*, which enables measuring flammability limits, minimum ignition energy, flame speed, and EGAI propensity of fuel-oxidizer-inert mixtures at elevated pressures and temperatures. In laser spark mode, a laser-generated spark is used to initiate ignition in the center of the adiabatic core of the gas mixture at a specified time after compression. Measurements of flame front propagation rate and EGAI propensity are obtained via a combination of Schlieren imaging and high-speed pressure measurements. The latter are used to calculate apparent heat release rates which indicate the combustion mode (propagating flame vs. end-gas autoignition).

At the beginning of every test, regardless of mode, the machine's pneumatic bellows are evacuated, forcing the piston/plunger assemblies to their bottom dead center (BDC) positions. The hydraulic cylinders are then pressurized, acting on the reverse side of the plungers to lock the assemblies in their fully retracted positions. Atmospheric or exhaust gases from the previous test are evacuated from the combustion chamber via a fill port on the top face of the chamber. A fresh reactive mixture is then drawn in from the liquid mixing tank (described in §2.2) and the fill port is closed off with a ball valve. After the gas exchange process, with the hydraulic locking system pressurized, the pneumatic bellows are filled to 200 psi with compressed air to provide the pressure differential needed for compression. Upon firing, the hydraulic lock is depressurized and the piston/plunger assemblies are forced through the hydraulic fluid until they reach the end of their stroke. Here, they are stopped by a hydraulic chamber trapped between the cylinder cap and the drive plunger, which prevents high-velocity metal-to-metal contact. The pistons are held at the fully extended TDC position by the drive force for the remainder of the test, forming a constant volume chamber.

The opposed piston design of the CSU RCM allows the machine to achieve much faster rates of compression than comparable configurations. However, the lack of a mechanical coupling between the drive assemblies allows for slight asymmetries during compression. Upon firing, the pistons do not begin to move until the pneumatic force contained in the air bellows is able to overcome the static friction between the piston assemblies and their housing seals. Friction is a stochastic phenomenon and, as such, there exists unpredictable and inconsistent differences between when each piston begins to move, and an asymmetric compression event can result (e.g. one piston reaches TDC before the other even begins to move). The resulting time difference used to quantify the severity of the compression asymmetry is termed "piston offset" - the temporal difference in piston position during compression. This is an important parameter as the proper function of the creviced pistons depends upon the symmetry of the compression event. Smaller pistons offsets indicate more symmetrical compression events that have lower levels of turbulence in the flow field after compression. As will be discussed at length throughout this document, piston offset is closely tied to the thermodynamic and fluid dynamic state of the gas after compression and, as such, is a parameter of critical importance.

2.2 Mixing Tanks

The reactive gas mixtures that are to be tested in the RCM are first formed in bulk quantity in mixing tanks. The tanks were designed and fabricated by Marc Baumgardner to facilitate the evaporation and mixing of liquid fuels with gases [18]. They feature external heaters and an internal magnetic stir bar to promote mixing. The tank walls are capable of withstanding the pressure rise brought about by detonation of the contained reactive gases, up to an initial unburned tank fill pressure of 2.000 bar. In addition, the tanks have been outfitted with burst discs to vent the high-pressure gases in the event that detonation occurs and the pressure exceeds the tank structural pressure limit.

Mixing test charges in the tanks, rather than in the RCM combustion chamber directly, increases mixture composition accuracy and consistency. This topic is discussed ad nauseam in

Appendix C. In short, the tanks offer added confidence in the temperature and pressure measurements used to infer the molar composition of the mixed gas. The tanks' internally mounted thermocouples and digital pressure gauges are far superior to the RCM chamber's external thermocouple and pressure gauge that is isolated from the main chamber by 0.5 m of tubing. Further, the substantial volume of the tanks (19.23 L) allows for tens of replicate trials to be carried out before mixture depletion – a disadvantage if mixture composition is to be varied, but a strong advantage for ensuring composition consistency among replicate trials.

The tanks are fully evacuated and heated to the target temperatures prior to filling. Liquid fuels are injected under vacuum, such that the vaporization pressure of the fuel at the tank temperature is far greater than the pressure inside the tank. Immediate, complete evaporation is assumed to occur. Tanks and fill lines are heated to 42°C such that condensation is avoided. Gaseous fuels, inert gases, and oxygen are then added in sequence. Mixture composition is indicated by the liquid volume of the injected fuel and the partial pressure of each constituent gas added to the tank. Temperature transients during filling are accounted for using the ideal gas law. See §3.1 for a description of the mixtures formed using this apparatus and Appendix C for the methodology.

2.3 Laser-Ignition, Schlieren Imaging, and Pressure Measurement Systems

Laser-ignition in the CSU RCM was first achieved by Dumitrache et. al. [16] in 2015. The original system was developed around a Q-switched, Nd:YAG 1064 nm Big Sky Ultra laser head with a pulse duration of 12 ns. Pulse energy was adjusted using a series of polarizers and a waveplate acting as a variable attenuator, and the beam was split to direct a small fraction to a photodiode to measure pulse timing. The majority of the beam was steered towards the combustion chamber, where it was passed through a focusing lens (*f* = 25 mm) in an optical plug. The lens was installed such that its focal point aligned with the center of the chamber and a spark was formed at this location for sufficiently high pulse energies. Dumitrache carried out minimum ignition energy (MIE) and minimum spark energy (MSE) studies for gaseous hydrocarbon fuels using the newly developed ignition system [19].

Preliminary laser-ignition experiments were carried out for PRF blends in 2017, but the laser head was repurposed for other projects shortly thereafter. In 2018, a water-cooled 1064 nm Nd:YAG Quantel Q-Smart 100 was purchased and now serves as the dedicated ignition source for RCM SI experiments. The laser's flash lamps are externally triggered by the RCM's pulse-delay generator and q-switching is achieved by the control unit's internal trigger. Similar to the original optical layout design, the laser first passes through a beam splitter that diverts a small fraction (~5%) to a photodiode used to measure the relative timing of the laser spark and the compression event. A second beam splitter diverts a portion of the remaining beam to an Ophir PE25BF energy sensor to indirectly measure the energy delivered to the combustion chamber via the spark. The remainder of the beam (~90%) is passed through a converging plano-convex lens (*f* = 50 mm) just before entering the RCM's combustion chamber. A laser-induced spark is formed at the focal point of the lens, aligned to the center of the chamber. The beam path as described is shown in red alongside the optical path for the Schlieren imaging system shown in green in Figure 3.

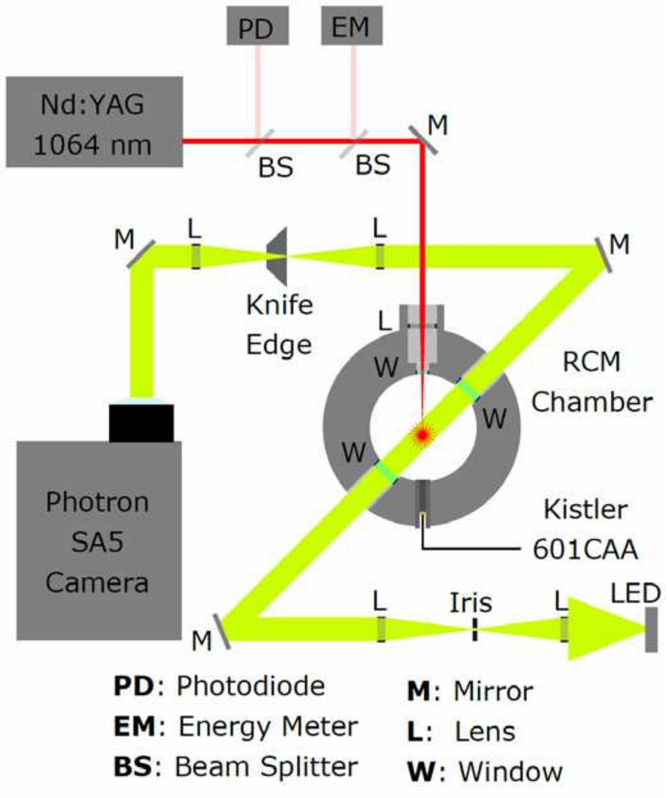

Figure 3. Schematic diagram of the RCM optical layout. Schlieren collimated light pathway shown in green. Nd:YAG 1064 nm laser pathway shown in red.

Combustion phenomena in the RCM are observed via a schlieren imaging system. This system is composed of a series of lenses and mirrors that direct collimated light through the combustion chamber and then to a high speed camera. It was also first implemented by Dumitrache et. al. in 2015 [19]. The optical path for the Schlieren system is depicted alongside that of the laser-ignition system in Figure 3. Light from a near ultra-violet LED is focused and passed through a mechanical iris to create a point light source. That light is then collimated and directed through the combustion chamber's opposing sapphire windows using a series of lenses and mirrors. Upon exiting the chamber, the light is focused to a point where it is aligned to partially interfere with a knife edge, such that approximately half of the light is blocked, and the other half is allowed to continue. This is essential to the Schlieren technique and accentuates density gradient visualization, allowing for clear identification of combustion phenomena, as described in more detail below. The light is recollimated, filtered, and directed towards a high-speed Photron SA5 camera. Figure 4 features a picture of the camera alongside an example Schlieren image, capturing fluid dynamic disturbances and a multi-lobal propagating flame shortly after ignition. This multi-lobal flame growth is characteristic of premixed laser-ignition and has been found to be of negligible influence to the experimental results [19].

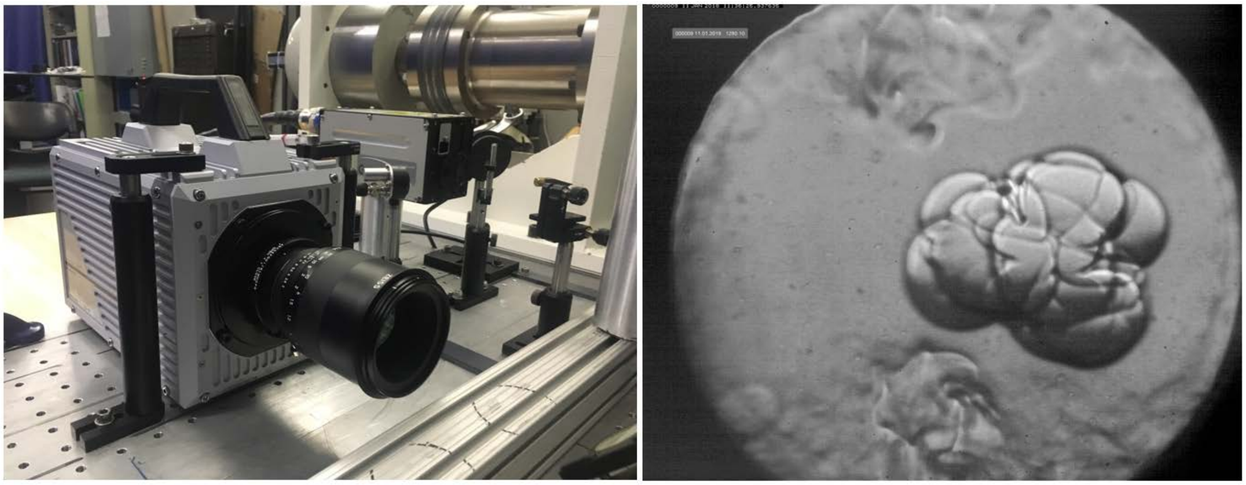

Figure 4. (a) Photron SA5 high-speed camera (b) example Schlieren image of a propagating flame shortly after laser-ignition.

Schlieren imaging is founded on the principle that collimated light will be refracted to a degree proportional to the gas density along the line of sight through the medium of interest. Compression often results in density gradients brought about by fluid motion. Combustion produces temperature inhomogeneities and species concentration changes that result in the formation of density gradients across burned and unburned regions. The proportional refraction of the collimated light allows for the visualization of these density gradients, and thereby the fluid-dynamic disturbances, flame fronts, and volumetric combustion events that produce them.

In 2018, the original PCO camera was replaced with a Photron SA5, capable of shooting up to 700,000 frames per second (fps) compared to the PCO’s 499 fps. This upgrade allowed for extreme temporal resolution. Most experiments presented in herein feature a frame rate of 50,000 fps, which was determined to be the optimal balance between file size and fidelity.

In-cylinder transient pressure measurement in the RCM is achieved via a piezoelectric transducer mounted internal to the combustion chamber. The Kistler 601CAA transducer is housed in a custom machined adapter plug that allows for easy installment, as pictured in Figure 5.

Figure 5. Kistler 601CAA piezoelectric pressure transducer and adapter plug. Pictured outside of its adapter housing (left), fully assembled (center), and mounted to combustion chamber (right).

Circuitry internal to the transducer compensates for temperature transients during testing. This means that the combustion chamber, and thereby the transducer, can be heated without affecting the accuracy of the pressure readings. The effect of the short-duration, extreme temperature transients brought about by combustion is not as well understood, but is assumed to be minimal, as the body of the transducer is not thought to physically experience those extreme transients.

Electrical signals produced by the transducer's piezoelectric crystal are amplified by a Kistler 5018 Charge Amplifier. The amplifier's range and sensitivity charge are set to 250.0 bar and -37.69 pC/bar according to the manufacturer's recommendation for the 601CAA transducer. Its time response constant is set to 10 s and the measurement signal output voltage to 25.00 bar/V. DC drift is accounted for by pegging the output signal to the initial pressure measured by the dual-capacitance manometer at the start of every test.

The output signal from the charge amplifier is collected by a Picoscope 4424 data acquisition system, along with the voltage signals produced by the laser timing photodiode and the linear variable differential transformers (LVDTs) measuring the piston stroke positions with time. Data is recorded at a sampling rate of 2 MHz and processed with in-house MATLAB software described in detail in Appendix D.

A pulse/delay generator is responsible for the orchestration of the laser-ignition and Schlieren imaging systems with the firing of the RCM. The unit gates the output voltage signal from the Kistler charge amplifier such that a threshold chamber pressure rise of 10 bar (0.40 V signal) activates the system. After prescribed delay periods, the camera and laser are triggered in sequence with +5 V pulses. The camera trigger delay is set to the smallest possible value, while the laser trigger is set to a 14.0 ms delay resulting in a 10.0 ms after top dead center (ATDC) ignition timing on average. Separate from the pulse/delay generator, the Picoscope DAQ is activated by a 20% percent change in signal voltage from the LVDT measuring the linear position of the left piston/plunger assembly.

Images recorded by the high-speed camera are mapped to their time-corresponding pressure measurements for the given experiment in post-processing. Given that the camera and DAQ system are triggered by different signals, they have their own separate time registries that must be aligned. The laser spark, manifesting as a voltage spike in the photodiode channel of the DAQ system and a distinct bright spot in the series of images, serves as an event for which the time of occurrence can be clearly identified in both acquisition systems. Thus, the spark event serves as an anchor point around which the time registries can be aligned and the recorded images can be mapped to the pressure trace.

Pressure data is recorded in a CSV file along with the piston positions and photodiode signal with time. These data are imported to an in-house MATLAB processing software (described in Appendix D) that is responsible for noise filtering and making the pertinent measurements (e.g. peak pressure, piston offset, EGAI timing if applicable, etc.). All raw, filtered, and measured data are saved along with the user-inputted initial conditions (e.g. test gas composition, chamber temperature) in a MAT file specific to that trial. Structuring the data in this manner allows for easy management of and access to the greater data set.

CHAPTER 3 – EXPERIMENTAL METHODS

Exploring alternative methods for the quantification of SI fuel knock propensity is central to the larger scope of this project. Towards this end, the RCM and its associated systems, described in Chapter 2, were employed to study PRF blends of varying reactivity in premixed SI conditions. This chapter describes the execution of laser-ignited experiments in the RCM, inclusive of the techniques used to control thermodynamic conditions after compression, identify characteristic apparent heat release rate (AHRR) signatures, quantify EGAI magnitude, and estimate flame propagation rate. Validity of the experimental methods is also discussed briefly.

3.1 Initial Condition Selection and Experiment Grouping

Operation of the CSU RCM in laser-ignition mode offers high-temperature, high-pressure conditions within which single-point ignition is achieved. Ignition occurs in a location where symmetrical compression creates a local stagnation region around which the temperature and velocity gradients are minimized. Such conditions lend themselves to fundamental SI combustion studies and are otherwise not found in the literature.

Test conditions that promoted EGAI ahead of the flame front were favorable to the defined objectives of the research. Homogenous autoignition RCM experiments were first performed to identify initial conditions for which a PRF blend with ON 100 would be just on the verge of autoignition, but would require the presence of a propagating flame to trigger volumetric heat release. Laser-ignition experiments were performed with similar initial conditions to these to study the onset of EGAI.

The initial conditions used in the laser-ignited RCM experiments are presented in Table 1, with the oxidizer/inert composition and initial pressure designated by an initial condition index by which they will be referred to throughout the remainder of this document. The initial external temperature of the RCM chamber was maintained at 300 +/- 2 K throughout. The thermodynamic conditions after compression were controlled by adjusting the initial pressure or by lowering the test gas mixture's specific heat capacity ratio. The latter was accomplished by displacing the inert mixture's nitrogen with carbon dioxide (note that argon could be used to raise the specific heat ratio). All experiments were performed with the fuel and oxidizer components in stoichiometric proportion. The fuel blends are designated by PRF number, such that the mole fraction of isooctane in the blend is given and the remaining fraction of n-heptane is implied (e.g., PRF 80 is composed of 80% isooctane and 20% n-heptane by mole).

Accuracy of the temperature estimations depends heavily on the accuracy of the compression ratio estimation for the machine. The ratio has been measured directly using the fluid displacement method and indirectly via a combination of isentropic compression correlations and computational modeling. In its current configuration, the compression ratio is 11.8:1, though this number is highly subject to the proper installation of RCM components (e.g. piston face position relative to the drive assembly) and combustion chamber accessories (e.g. recession depth of windows).

The RCM's primary purpose is to raise the temperature and pressure of a test gas mixture, but the consistency by which it does so needs further consideration. Piston offset, introduced in §2.1 is a stochastic phenomenon in the CSU RCM, and causes significant variation in the compression speed and symmetry which subsequently affect the chamber pressure, temperature, turbulence levels, and TDC timing from one trial to the next. Piston offset presents a significant challenge to experimental repeatability, seeing that combustion phenomena are highly sensitive to temperature. Amongst a group of experimental trials with the same initial conditions, temperature at TDC can vary by as much as 80 ˚C, and such extreme variability prevents experiments from being grouped by their initial conditions.

Table 1. The six initial conditions used for the laser-ignited RCM tests. TDC temperatures were estimated using the ideal gas law with the known gas composition, initial temperature, pressure, and specific volume with time. For experiment indices 1-3, thermodynamic conditions were altered by adjusting the initial pressure prior to compression. For indices 4-6, conditions were altered by adjusting the inert composition. All experiments performed with stoichiometric fuel/oxidizer blends. Physical changes were made to the combustion chamber fill valve during the tests performed under experiment index 5. These changes increased the compression ratio from 11.6:1 to 11.8:1. Initial pressure was lowered to achieve similar TDC conditions to those of experiment index 4.

Index	Initial Pressure	Oxidizer/Inert Blend Composition (mole %)			Compression Ratio	TDC Temp. Range	TDC Press. Range
	(bar)	O2	N2	O2	(-)	(K)	(bar)
1	1.000 ± 0.001	21%	79%	-	11.6:1	729 - 887	24.9 - 27.8
2	0.900 ± 0.001	21%	79%	-	11.6:1	730 - 867	22.7 - 25.7
3	0.750 ± 0.001	21%	79%	-	11.6:1	725 - 873	18.8 - 22.9
4	1.000 ± 0.001	21%	67.1%	11.9%	11.6:1	698 - 829	24.4 - 26.2
5	0.975 ± 0.075	21%	67.1%	11.9%	11.8:1	702 - 817	24.5 - 25.8
6	1.000 ± 0.001	21%	39.5%	39.5%	11.6:1	691 - 775	23.2 - 24.4

It is of interest to group experiments by the actual compression temperatures that the contained gases have been exposed to, rather than by their initial conditions alone (i.e. group experiments based on their TDC conditions rather their BDC conditions). One possible method for accounted for compression temperature differences between experiments is through single point temperature sampling, in which temperature criteria are established at single point in the temperature time history (e.g. at TDC or at the time of ignition). This method is represented in the example compression temperature profile of Figure 6 by the temperature sample point at TDC. Though this method is an improvement over grouping experiments by their initial conditions, it has proved insufficient, as significant variability in heat transfer rates brought about by piston offset have also been observed. Heat transfer is the primary driver behind temperature variability after the pistons reach TDC, and thereby has a strong influence over the temperature time history. To account for the variability more completely, the estimated temperature profile is integrated from 10.0 ms before ignition (near the time of TDC) to the time of ignition, and experiments are grouped by that integrated value, in units of Kelvin-seconds (Ks), that is returned. This method is depicted in Figure 6 by the shaded region under the temperature profile.

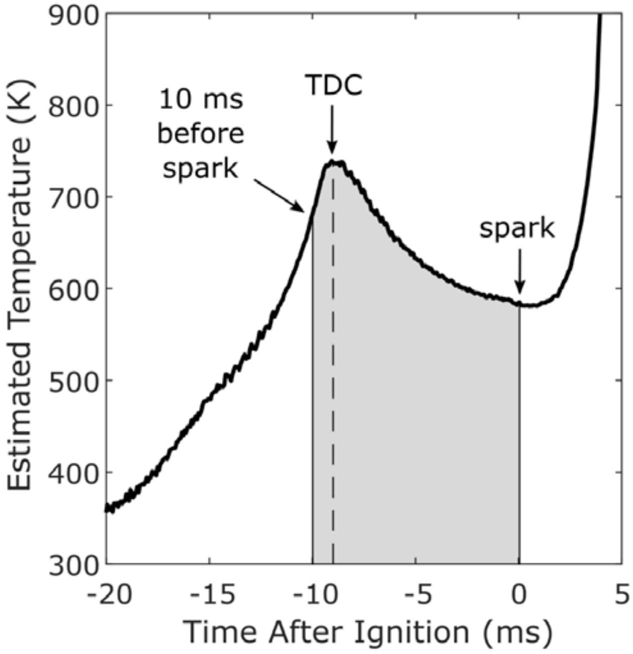

Figure 6. Illustration of the TDC temperature integration characterization described. The test's integrated temperature refers to the shaded area depicted.

The time bounds of the temperature history integral are established so as to minimize the time sensitivity of the groupings. Reaction rates are exponentially sensitive to temperature, but not time. Should the temperature history integral be evaluated for the entire profile up until the time of ignition, the time sensitivity would be exaggerated, and compression variability would make the temperature history integration groupings nonsensical. The same is true for evaluating the integral from TDC to the time of ignition, as the timing of TDC is also variable. The time bounds of the integral are somewhat arbitrary, so long as the integral is evaluated over the same time period for all experiments in the data set.

Piston offset also determines the relative turbulence of the flow field after compression. Turbulence has been found to strongly influence the propagation rate of the premixed SI flames which in turn affect the severity and timing of the volumetric combustion events. In a similar way to the time integrated temperature histories, piston offset is bounded to define selection criteria. The two grouping methods are combined to create a map of TDC conditions for all experiments, represented by the integrated temperature and piston offset in Figure 7.

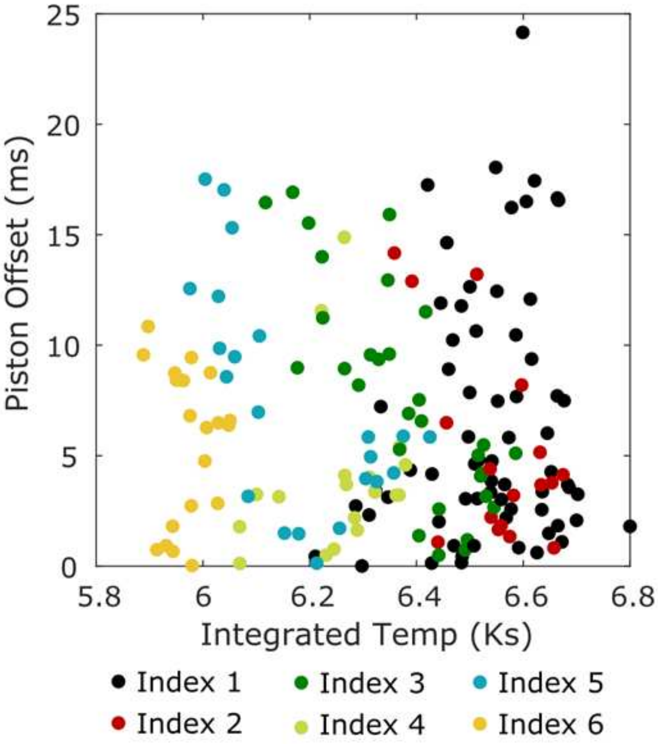

Figure 7. TDC condition characterization of all experiments performed herein. Integrated temperature and piston offset used to denote temperature history and relative turbulence level of the flow field after compression. Experiment indices refer to those listed in Table 1. Shown here to illustrate the apparent lack of connection between initial condition and TDC condition.

Data point proximity on this map represents the similarity of the TDC conditions amongst the experiments. The effects of compression inconsistency are clearly illustrated by the overlap of the initial condition index groupings. Prior to this study, it was thought that the TDC temperatures and pressures for a given set of initial conditions were fairly consistent and each initial condition represented a discrete test condition. This is no longer the case. Experiments are now grouped by the region of the TDC conditions map (Figure 7) that they occupy, regardless of their initial condition, to provide a more accurate representation of the TDC conditions after compression. It is argued that this method of grouping is far superior to the method of grouping by initial condition, as it reveals the fundamental combustion sensitivities that are of interest.

There has been much dispute about this grouping method, and it's worth elaborating on further. The RCM is an obscure machine that serves no practical value other than in conducting fundamental combustion studies. It should be thought of as a machine used only to create a product that is to be studied. That product in this case is a high-temperature, high-pressure reactive gas mixture with known composition. The conditions of the reactive gas after compression are what is of interest, not the method by which the machine achieves those conditions. To group trials by their initial conditions would be to assume that there is value in studying the RCM as a machine and not the high temperature gases it produces. This of course can be true if it is of interest to improve the performance of the machine, but that is not the focus of this study. This study is combustion centric. Compression inconsistency is a known problem that causes vast differences in the TDC conditions of the gases. It would entirely shift the focus of the study to the performance of the RCM itself if those inconsistencies were not accounted for.

3.2 Apparent Heat Release Rate Derivation and Data Filtering

Combustion phenomena in the RCM experiments are characterized by their apparent heat release rates (AHRRs). The heat release rate (HRR) is representative of the rate at which chemical energy in the reactive charge is released (i.e. the rate of combustion). Experimentally, this rate of energy conversion cannot be directly measured and is instead indicated by a change in a property than can be measured – pressure. At a given instant, the rate of change in the chamber pressure is a function of the energy conversion rate and the rate at which energy is leaving the system via heat transfer to the chamber walls. The measured pressure rise is the net result of the pressure rise due to combustion and the pressure decrease due to heat transfer. Using the net change in chamber pressure to estimate the HRR in this way results in an apparent term – the AHRR.

Derived from the first law of thermodynamics, the apparent heat release rate for an ICE is a function of both the change in volume and the change in pressure with crank angle as shown in Equation 4 [1], where Q is heat in J, θ is the crank angle in degrees, γ is the ratio of specific heats of the mixture, P is the pressure in Pa, and V is the chamber volume in m^3.

$$AHRR = \frac{dQ}{d\theta} = \frac{\gamma}{\gamma-1} P \frac{dV}{d\theta} + \frac{1}{\gamma-1} V \frac{dP}{d\theta} \tag{4}$$

RCM experiments feature a constant volume chamber after the compression event, making $\frac{dV}{d\theta}$ equal to zero during combustion and eliminating the first term in the AHRR relation. Equation 4 is modified further to be time based rather than crank angle based, and takes on the simplified form in Equation 5 below. The resulting AHRR is measured in W, with t representing time in s.

$$AHRR_{CV} = \frac{1}{\gamma-1} V \frac{dP}{dt} \tag{5}$$

The specific heat ratio, γ, of the mixture varies with composition and temperature. For convenience in its estimation, the mixture composition is assumed to be constant, despite the fact that it is changing substantially over the course of the chemical reaction. The specific heat ratio of the constant composition mixture is approximated using specific heat ratio temperature correlations for the mixture constituents and the temperature estimations made via the ideal gas law with time.

The importance of evaluating the AHRR lies in the identification of the unique AHRR signatures that distinct combustion phenomena exhibit. Figure 8 features an example AHRR profile within which three modes of combustion have been identified. The low-level AHRR rise from 0-2 ms is indicative of a propagating flame. That flame gives rise to a pressure increase which then triggers low-temperature chemistry (LTC) in the end-gas, revealed by the local peak at ~2.3 ms, which soon after gives rise to a high-magnitude AHRR spike indicating EGAI. This AHRR profile is plotted amongst other trials in a greater data set to depict how the unique AHRR signatures vary across cases of varying reactivity and thermodynamic conditions.

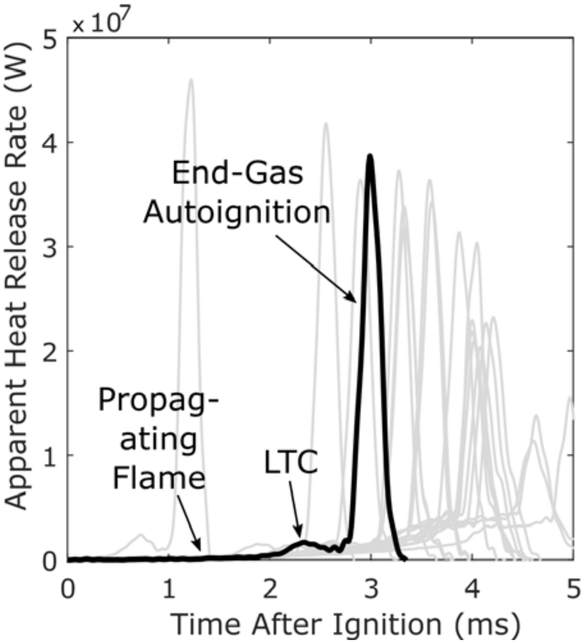

Figure 8. Example of the AHRR profiles and the unique peak signatures that are characterstic of distinct combustion phenomena.

AHRR profiles that allow for identification of the combustion mode in this way depend upon data filtering techniques. EGAI can, and often does, result in heavy pressure oscillations that disrupt the evaluation of the AHRR at a given time. Since AHRR is at its essence the derivative of the pressure curve, any measured pressure drop brought about by these oscillations will result in a negative AHRR value of proportional magnitude. Though this is not as negligible as signal "noise," it is a non-physical result with regard to the energy release rate that it is meant to represent – i.e. the chemical reactions do not momentarily reverse.

Both pressure and AHRR data have been filtered in all data presented in this work, unless otherwise stated. The raw pressure signal is processed with an infinite impulse response (IIR) low-pass filter with a half-power frequency of 0.01. The filtered pressure data is used to calculate a raw AHRR, that is then passed through a moving average filter of 350 points for a sample rate of 2.0 MHz to produce the final AHRR profiles that are depicted. Striking a balance between minimizing oscillations and retaining real response data is challenging. Filter types and settings have been selected somewhat subjectively, but much attention has been paid to ensuring that the data has not been over filtered (see §5.5).

3.3 Quantification of End-Gas Autoignition Magnitude and Propensity

Towards the goal of establishing an alternative SI knock propensity metric, methods have been developed to quantify the magnitude of EGAI events based on the derived AHRR profile. The consistency of the AHRR signatures used in the RCM to identify combustion mode, and therefore detect EGAI, allow for the derivation of mode specific combustion power ratio terms. These power ratio terms are used to quantify a specific combustion mode's contribution to the total AHRR profile that is measured. That is, the measured AHRR profile is postulated to be the result of a convolution of multiple lower magnitude AHRR profiles from specific combustion phenomenon that could be acting in the chamber at a given time. Deconvolution of the AHRR profile in this way is an established method in dual-fuel engine combustion research for estimating the heat release brought about by the diffusion and premixed flames individually [20]. Specific to the laser-ignited RCM experiments, this convolution theory implies that the AHRR spike denoting

EGAI is in fact the combined result of the volumetric heat release event and the propagating flame that was established by the laser-spark at the start of the test. Figure 9 features an example of how the measured AHRR profile can be deconvoluted into the component AHRR profiles that compose it.

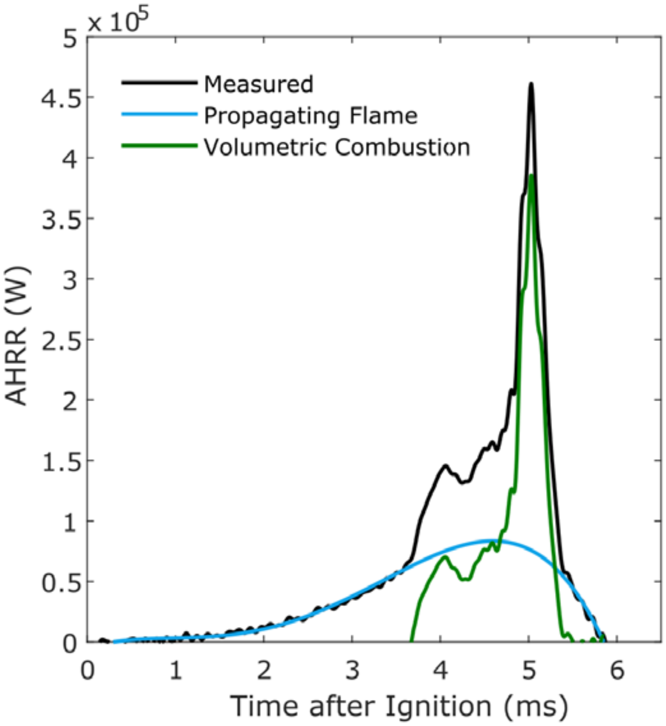

Figure 9. Deconvolution of the measured AHRR profile into its components - the propagating flame and volumetric combustion events. Volumetric combustion includes the heat released by both LTC and EGAI.

Integration of the component AHRR profiles results in the estimated energy released by each combustion mode. However, the magnitude of the AHRRs measured depends on the data filtering methods used, and the power and energy values derived must therefore be normalized. This is accomplished using ratios, such that the apparent amount of energy released by a specific combustion mode is compared to the total amount of apparent energy released during the experiment. Thus, the magnitude of an EGAI event is characterized by its energy ratio term, defined as the EGAI heat release fraction, f_{EGAI}, as follows:

$$f_{EGAI} = \left[\int \frac{dQ}{dt}\right]_{EGAI} \Big/ \left[\int \frac{dQ}{dt}\right]_{Total} \tag{6}$$

Here dQ/dt is the apparent heat release rate in W. The numerator is integrated heat release during EGAI in J, and the denominator is the integrated total heat release in J.

An example AHRR profile is shown in Figure 10 to illustrate how deconvolution and evaluation of f_{EGAI} are done. To isolate the AHRR contribution of the EGAI event, a quadratic function is fit to the AHRR profile before and after EGAI. The AHRR profile is thus deconvoluted into two the heat release profiles - that of the propagating flame and of the EGAI event. The f_{EGAI} is evaluated as the integral of the isolated EGAI AHRR profile (i.e., the area between the AHRR curve and quadratic fit function).

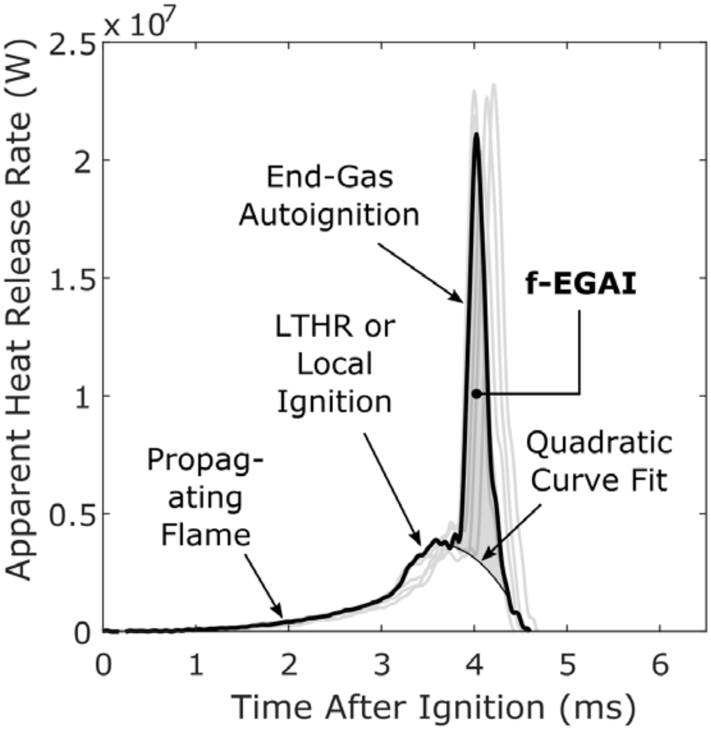

Figure 10. Illustration of the quadratic curve fit method for AHRR deconvolution and EGAI fraction evaluation for example AHRR profile. Representative trial presented with its replicates shown in gray.

Arguments can be made for why f_{EGAI} should be evaluated without deconvolution of the AHRR profile. These avenues have been explored quite extensively, and the method of deconvolution prior to the integration of the AHRR profile has proven to be the most fair, consistent, and robust means of quantifying EGAI magnitude in this experimental apparatus. Section 5.5 discusses the possibility of combustion in the crevice volumes behind the piston faces after or during the EGAI event. Though it is unclear whether this is occurring, such behavior would be unfairly characterized as volumetric heat release if not for the deconvolution method. Further, deconvolution has been found to enhance the f_{EGAI} difference between fuels of different reactivities, and thus lends itself as an EGAI propensity measurement technique with improved resolution.

3.4 Flame Propagation Rate Measurement

In addition to providing supporting optical evidence for combustion mode identification, the high speed Schlieren imaging system is used to approximate flame propagation rate. Image post-processing software was developed in MATLAB for this purpose. It is able to properly identify the captured flame surface over a wide range of conditions (e.g. window cleanliness, turbulence levels, framerate, position, focal depth, etc.) and make the necessary conversions and calculations to return the approximate unburned, zero-stretch propagation rate for a given trial. This code is described at length in Appendix B. Here, the general methodology will be presented, inclusive of the measurement technique, the burned to unburned rate conversion, and the extrapolation of the measured data to the zero-stretch condition.

Premixed flame propagation rate is governed by the speed at which the deficient reactant can diffuse into the flame front. As such, it is highly sensitive to temperature and turbulence levels, which can vary both spatially and temporally in the RCM experiments. It follows that the local propagation rate and direction are often not representative of the other portions of the flame in the domain, and it is of interest then to capture the average propagation rate over the entire flame surface, rather than simply track the propagation distance with time in one direction.

Average propagation distance at a given instant is estimated using the projected area of the flame surface on the two-dimensional Schlieren image in which it is captured. That projected flame area is equated to a circle of the same geometric area, and the radius of the circle is taken to be the average propagation distance of the flame surface from the location of ignition for the time at which the image was taken. This process is illustrated in Figure 11. When it is repeated over the entire sequence of images, a time history of the flame's propagation distance results and a propagation rate can thus be approximated.

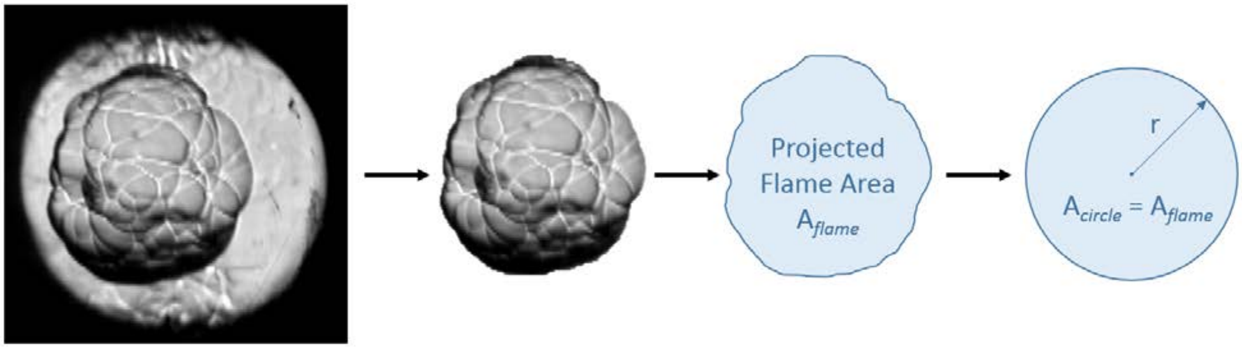

Figure 11. Illustration of the projected flame area method for approximating flame propagation distance, r, with time.

Second-order polynomial regressions are fit to the propagation distance time histories to eliminate measurement noise, as shown in the example of Figure 11. Curvature in the distance time profile is thought to be the result of flame stretch rather than of increasing gas density ahead of the flame front. Outward propagation of the flame compresses the upstream unburned gases, and an apparent deceleration of the flame front will eventually result. However, just before the outer perimeter of the flame leaves the field of view, the flame encompasses a mere 7% of the chamber volume. This is considered sufficiently small such that the deceleration caused by increasing upstream density is negligible.

Flame stretch, on the other hand, was not found to be negligible. As characterized by the geometric “flattening” of the surface as the flame sphere becomes larger, flame stretch is much more prominent in smaller flame volumes. The zero-stretch limit is reached with an infinitely large spherical flame volume, as the curvature of the surface at that point is null. Flame stretch is a function of the propagation rate and instantaneous radius for spherically expanding flames, as given by Equation 7 [10].

$$k = \left(\frac{2}{r_f}\right)\left(\frac{dr_f}{dt}\right)\ [s^{-1}] \tag{7}$$

Where k is the stretch rate, r_f is the flame radius, and $\frac{dr_f}{dt}$ is the measured propagation rate. To approximate the zero-stretch condition, the trend between stretch and propagation rate over the time interval for which the measurements were taken can be assumed to be linear, as Equation 8 denotes [10].

$$S_b = S_b^0 - \ kL_b \ \ \left[\frac{cm}{s}\right] \tag{8}$$

Here, S_b is the measured burned propagation rate, S_b^0 is the extrapolated burned propagation rate for the zero-stretch condition, and L_b is the Markstein length. S_b^0 and L_b are found by fitting the stretch versus propagation rate data with a linear regression. However, Kelley and Law developed an alternative extrapolation strategy, able to correct for nonlinearities that could be brought about by high stretch rates or non-equidiffusion conditions in cases with a non-unity Lewis number [21]. The non-linear extrapolation equation that they developed is presented in Equation 9 below.

$$S_b = S_b^0 t + cr_f + 2L_b \ln\left(r_f\right) - 4\frac{L_b^2}{r_f} - \frac{8}{3}\frac{L_b^3}{r_f} \tag{9}$$

Where t is time and c is a measurement constant. To extrapolate S_b^0 from this equation, initial values for S_b^0, L_b, and c are inputted into a numerical solver that minimizes the error between the measured and the calculated flame radius for a given time. The difference between the zero-stretch burned propagation rate derived by this equation and by the linear extrapolation method was found to be minimal in this study, as depicted in the example of Figure 12. Nevertheless, Kelley's non-linear extrapolation method was employed for all flame propagation rate measurements presented herein.

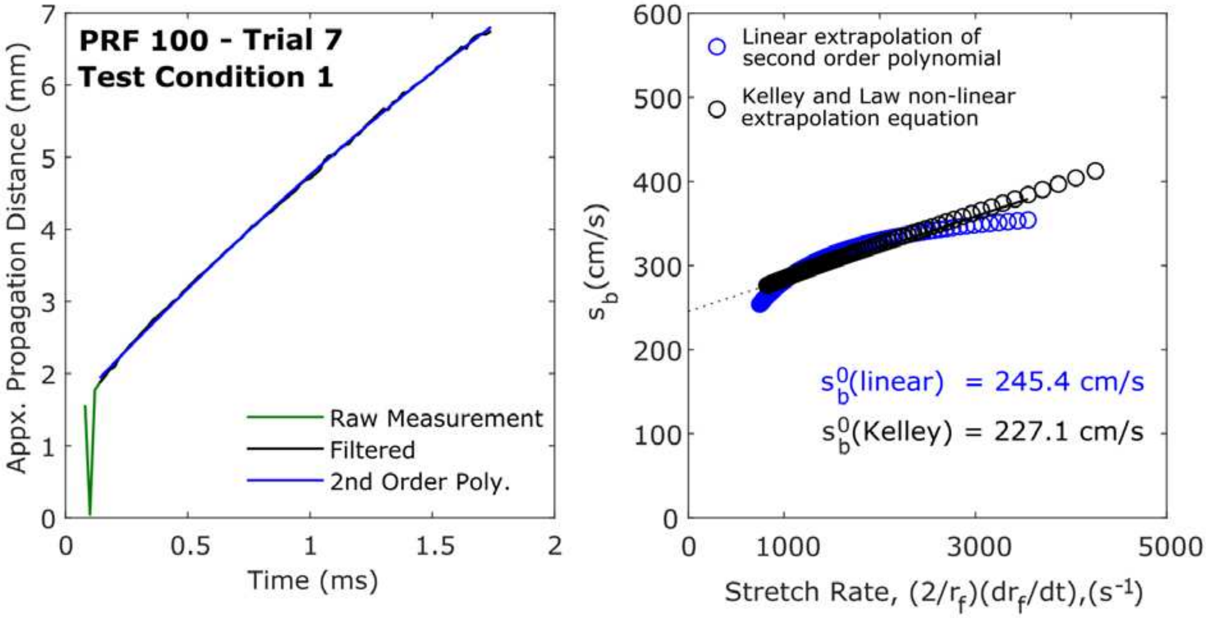

Figure 12. Example flame propagation rate measurement. The propagation distance measurement history is shown in the left plot. Raw measurements are filtered to eliminate images in which the flame surface was misidentified. A second order polynomial is fit to the filtered measurements and used to derive the trends between stretch and propagation rate that are shown on the right. The blue markers on the right plot represent stretch and propagation rates calculated using the polynomial. The black markers represent those rates as derived by the non-linear Kelley extrapolation method. The dotted black line is a linear regression fit to the *blue* markers and is used to extrapolate to the burned propagation rate of the zero-stretch condition. The zero-stretch propagation rate of the black markers is one of the equation constants that defines the curve itself.

The zero-stretch burned propagation rate is next converted to the zero-stretch unburned propagation rate to facilitate a fair comparison with literature. This is done to correct for the expansion of the flame surface caused by the density gradient between the burned and unburned regions. Combustion products left behind by the flame exhibit extreme temperatures and are much less dense than their unburned counterparts upstream. This results in a substantial difference in density across the flame front and in order for the pressure to equalize throughout the chamber, that flame surface must expand. Note that this expansion is distinctly different from the propagation brought about by reactant diffusion. The propagation rate observed in the experiment is the combined result of the flame expanding and its consumption of unburned reactants – the burned flame speed. It is standard practice in reporting flame speeds to correct for this density change and report the unburned flame speed, provided by Equation 10 below [9]. Here, s_u and s_b are the unburned and burned flame speeds and ρ_u and ρ_b are the unburned and burned gas densities. The burned flame speed is measured directly, while the propagation rate and the burned and unburned densities are estimated using the pressure and temperature at the time of ignition and the adiabatic flame temperature for the reactive mixture.

$$s_u = s_b(\,\rho_b/\rho_u\,) \tag{10}$$

A final distinction to make is that between the unburned flame propagation rate, of which is derived through this process, and the unburned laminar flame speed. Though a perfectly symmetrical compression event can result in a nearly quiescent flow field, even the mildest of fluid dynamic disturbances can affect the rate at which a flame propagates. For this reason, propagation rates measured in spark-ignited RCM experiments are expected to be considerably higher than laminar flame speeds reported in literature.

CHAPTER 4 – COMPUTATIONAL MODEL DESIGN

Reactive computational fluid dynamic (CFD) models serve to inform experimental observations and elucidate combustion physics that underlie EGAI in laser-ignited RCM experiments. Given the inherent variability of RCM compression, constructing a predictive CFD model is an arduous and inconsequential task. The scope of the modeling efforts presented herein is limited to: (1) informing experimental findings via the construction of models specific to individual experimental trials and (2) depicting the influence of fuel reactivity and thermodynamic condition on combustion phenomena via the utilization of a more general model. This section gives an account of the motives behind this approach and the methodology of the RCM computational model construction.

4.1 Model Selection and Strategic Approach

Computational models were constructed using CONVERGE CFD software. CONVERGE was selected for its grid modification superiority and specificity to IC engine modeling. Siddhesh Bhoite created the first CSU RCM models in 2016 [14], from which the current models are derived, though substantially modified and optimized.

All simulation work presented herein features k-ε RANS turbulence and SAGE combustion modeling. Standard k-ε RANS was selected for its numerically robust performance in modeling contained turbulent flows in which mixing rate prediction is of primary concern [22,23]. SAGE combustion with reduced chemical kinetics was chosen for its approach that centers on chemical reaction modeling rather than on constructed correlations with experimental data.

SAGE combustion is grid cell specific. Chemical reactions in a single cell are modeled in zero dimensions using rate constants calculated for the instantaneous species compositions and temperatures of the given cell [22]. Species concentration changes within the cell are caused by the modeled chemical reactions, but are also affected by molecular diffusion from adjacent cells. In this way, three-dimensional combustion modeling with SAGE is simply the orchestration of many 0D chemistry models acting on the individual grid cells.

This “chemistry first” approach is dependent on the chemical kinetic mechanism file that houses the combustion relevant reactions and their rate constants. Typical chemical mechanisms feature several hundred species that interact with one another through thousands of reaction pathways. Using such a mechanism in a three-dimensional CFD simulation would be cumbersome and likely unnecessary. As an alternative, the most relevant species and reaction pathways are identified for a particular circumstance with a reduction and verification method. Those relevant species and reactions are isolated into a “reduced” mechanism that is a fraction of the size of the parent, yet exhibits similar predictive capability. Throughout this study, two externally developed chemical kinetic mechanisms were used – a 72 species, 296 reactions mechanism from the Wang group at University of Wisconsin - Madison (Wang – 72) and a 121 species, 538 reactions mechanism from the Lu group at University of Connecticut (Lu – 121) [21, 22]. Both were reduced for conditions specific to high-temperature, high-pressure PRF blend combustion.

The RCM computational models are categorized by the approach taken to simulate the compression events. Nominally, they are split into two categories: symmetric and asymmetric. Both are sector domains that are radially mirrored about the central axis using periodic boundaries to reduce domain size. Symmetric models utilize a $1/8^{th}$ sector domain mirrored about the central axis plane, such that the motion of a single piston represents the average volume change with time during compression. Thus, the compression event is assumed to be symmetric and only the left or right half of the machine is modeled. This approach minimizes computational expense and modeling effort to the detriment of accuracy. Asymmetric models do away with the mirrored plane and model the motion of both pistons in a 1/4th sector domain. Here, the effects of piston offset can be accounted for, thereby potentially increasing the agreement between the model's pressure/temperature time profiles with what is observed in an individual experiment. The modeling effort expended is much higher with this method, as the measured position of both pistons over time for the selected representative experiment must be imported (see §4.3). The computational expense is also much greater as it increases proportionally to the domain size which is twice as large as the symmetric model domain. The symmetric and asymmetric domains as rendered in the CONVERGE user interface are presented in Figure 13. Boundaries are identified by type for the symmetric domain in Figure 14.

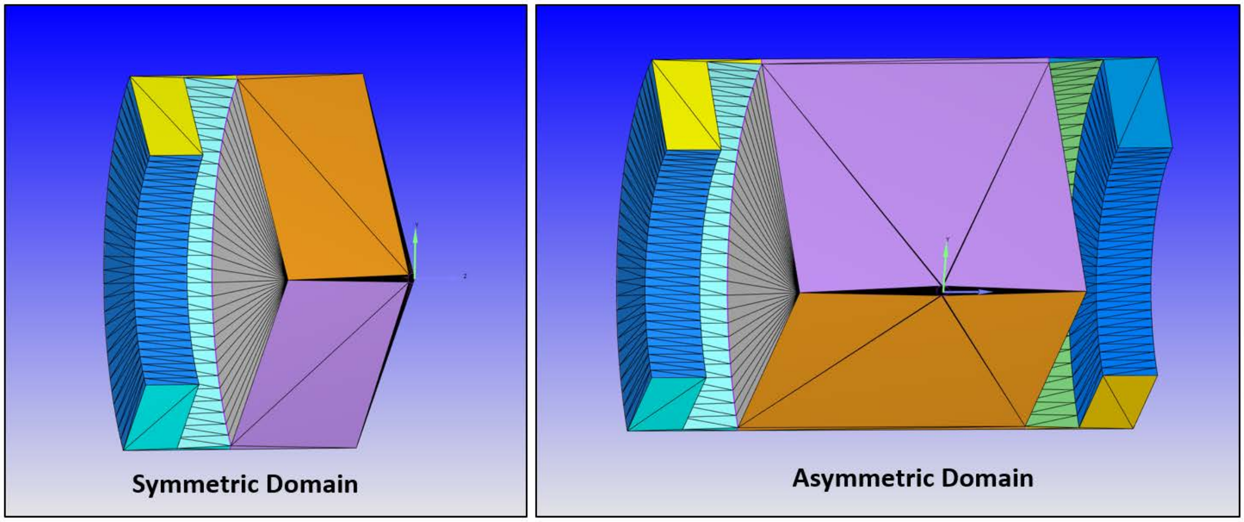

Symmetric Domain

Asymmetric Domain

Figure 13. Symmetric and asymmetric model domains as represented by their STL surface files in the CONVERGE user interface.

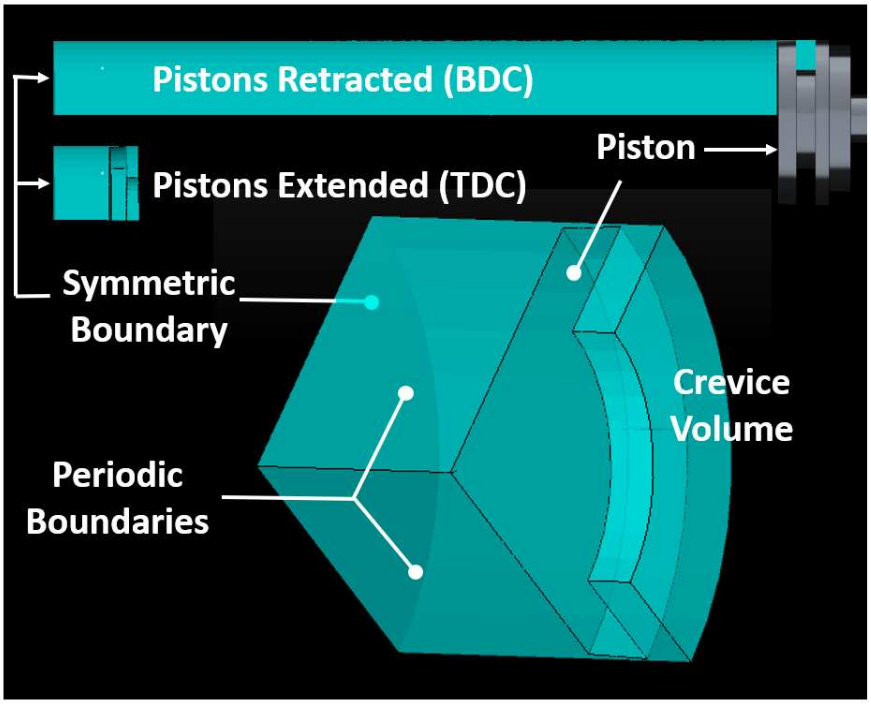

Figure 14. Symmetric model domain with periodic and mirror boundary type callouts. Volume change associated with compression depicted by the BDC and TDC domains at the top of the image.

Accurate representation of the RCM's trapped mass and compression ratio is most essential to ensuring accuracy of computational model results. Despite best efforts to measure chamber volume directly, a fair amount of uncertainty still surrounds the actual values of these parameters. Frequent servicing of the RCM's combustion chamber introduces the possibility of unintended variation in the chamber volume and compression ratio. For example, chamber windows could be installed at slightly different depths or the piston/shaft seals could cause the pistons to extend slightly further than they did in the previous installation. Nevertheless, the compression ratio, as informed by fluid displacement volume measurements and isentropic compression predictions, is thought to be 11.8:1 in the RCM's current configuration.

The modeled compression ratio and trapped mass reduce directly to the BDC and TDC volumes of the computational domain. These volumes must be inclusive of the dead volumes associated with chamber accessories (e.g. recessed windows, fill-port ball valve, etc.). It is in the interest of computational expense to assume perfect cylindrical symmetry so that periodic sector domains can be implemented. Thus, the dead volume in the chamber fill-port valve (~1.3 mL), that in reality creates a condition of asymmetry as it is connected to the main chamber on its top side via a narrow channel, must be accounted for in a perfectly cylindrical model domain. This is achieved through modification of the model's piston spacing (i.e. the distance between the piston face and the central axis plane at BDC or TDC). A target TDC volume inclusive of all dead volumes is specified, and a piston spacing that maintains that volume is calculated from the specification rather than being measured directly on the machine. In the perfectly cylindrical model, the piston spacing is 10.6 mm, where in reality, the pistons are closer together with a spacing of 9.8 mm with various asymmetric protrusions making up the remainder of the volume. In a similar fashion, the piston spacing at BDC is calculated for using the specified TDC volume and compression ratio target values.

The strategic approach taken to computational modeling accords with the tasks outlined at the start of this chapter. Symmetric models are employed to analyze how changes to fuel reactivity or thermodynamic condition can affect the resulting combustion phenomena, absent variability in compression. Asymmetric models aim to match the temperature and pressure time histories of an individual representative experimental trial as closely as possible. In doing so, the model results can inform the experimental observations made during that specific experiment, and can be extended to others of a similar sort.

4.2 Grid Design and Resolution Sensitivity

Central to any CFD modeling campaign are efforts of ensuring that the mesh design and resolution are sufficient for the selected turbulence model, while optimizing the domain such that computational expense can be minimized. This section presents the methodology behind testing the quality of the computational domain, through exploring the effects of reducing the chamber's geometry to a sector and ensuring that the mesh can properly resolve the length and time scales of turbulence and combustion. The live mesh modification techniques that have been utilized are also discussed.

Past RCM models tended to exhibit non-physical flame propagation behavior near periodic and mirrored domain boundaries. To investigate this abnormality's effect on the overall heat release, a simplified cylindrical domain was constructed for isolated testing along with an equivalent 1/8th sector. The two domains are pictured in Figure 15 and served as the foundation upon which the majority of grid design and modification strategies could be tested. The 1/8th sector domain was constructed with both periodic and symmetric mirror boundaries in a similar fashion to the final RCM models.

To maximize the relevancy of the sector symmetry sensitivity tests, the domains were of similar dimension to the RCM combustion chamber, initiated with premixed air and fuel, and ignited via spark at the center of the chamber. Baseline tests were performed with a stoichiometric isooctane/air mixture at 1 bar and 298 K, using the 73 – Wang reduced mechanism. The spark was modeled with a thermal hotspot, and adaptive mesh refinement (AMR) with fixed embedding techniques were applied. The average pressure trace results from the two domains are presented in Figure 16. Differences between the two cases exist and are likely due to cell count limitations imposed. For the same resolution, the 1/8th sector requires substantially fewer cells in the grid compared to the full domain. The error introduced by utilization of the periodic and symmetric boundaries can be considered negligible in light of the considerable computational savings.

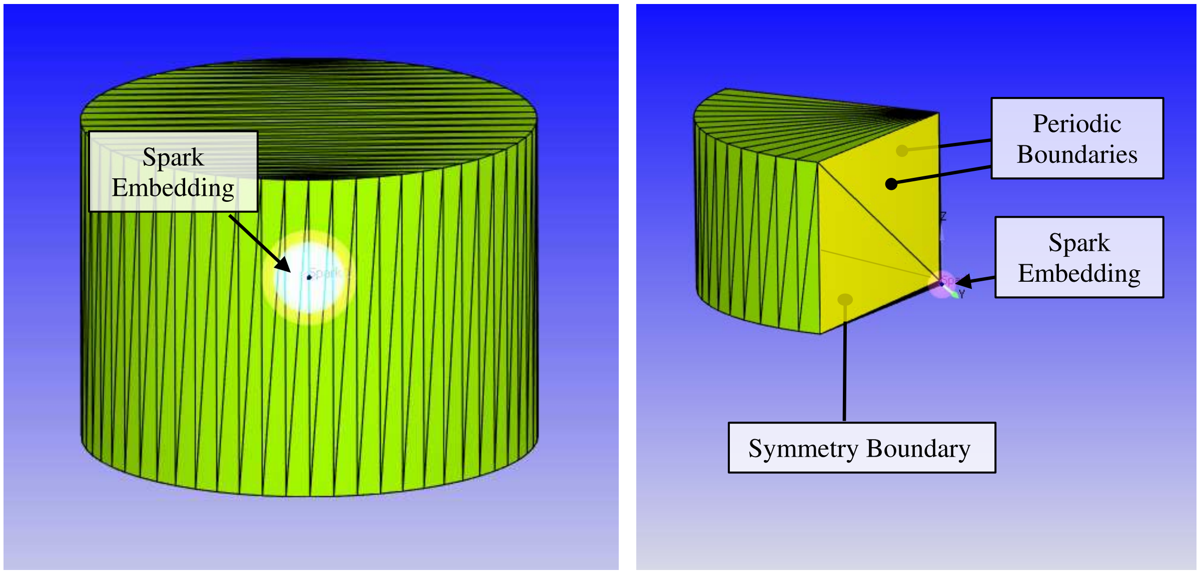

Figure 15. Full scale and 1/8th sector computational domains used for grid design and testing.

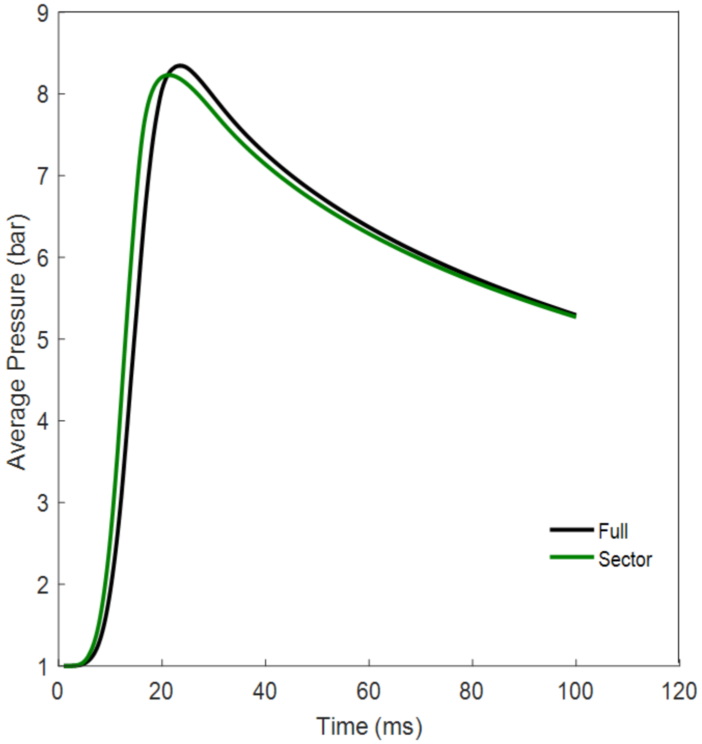

Figure 16. Premixed spark-ignited pressure trace results for the full and 1/8th sector domains. Initial pressure and temperature at 1 bar and 298 K. Ignition occurs at t = 1.0 ms.

Turbulence modeling weighs heavily on the resolution and quality of the grid. A mesh must be capable of resolving the required turbulent length and time scales of the implemented turbulence model. Reactive CFD introduces the added challenge of ensuring that the grid can resolve combustion phenomena at the length and time scales required by the selected combustion model. For premixed propagating flames, this means that the grid must be sufficiently resolved across the thickness of the reaction zone (i.e. the flame). Neither the turbulence nor the combustion model grid resolution requirement can be determined a priori, however. An initialization model must be run first, in order to have an idea of the length and time scales that govern the resolution requirements. Ensuring sufficient grid resolution is therefore an iterative process.

CONVERGE CFD software is structured around its automatic orthogonal generation schema. The grids are modified by the user via specification of the base cell dimension, adaptive mesh refinement (AMR) level, and fixed embedding. AMR uses a tracking parameter (e.g. temperature or velocity difference between two adjacent cells) to identify areas in which the grid is too coarse and to automatically increase the resolution in those regions [22]. Fixed embedding instructs CONVERGE to force an increased resolution criterion where necessary (e.g. next to the wall or in the area of the spark). AMR and fixed embedding levels are set such that the n^{th} level will decrease the base grid cell side length by an order of 2^n in the region of interest. That is, if AMR is set to level 3 for a base grid cell of 1 mm side length, activation of AMR will result in a refined cell size of 1 mm $/(2^3)$ – or 0.125 mm. AMR is activated for nearly all of the simulations presented herein using adjacent cell temperature, velocity, and concentration difference as the tracked parameters. The autoignition precursor species formaldehyde (CH_2O) and hydrogen peroxide (H_2O_2) were monitored as part of the concentration difference AMR strategy.

The simplified cylindrical sector domain is used once again to determine the appropriate base grid cell size and AMR level for premixed SI combustion in the RCM. Of primary concern is the ability to fully capture the behavior of the chemical reactions and their effect on the thermodynamic and fluid dynamic conditions of the rest of the chamber. It is of interest to optimize the base grid cell size, AMR level, and overall domain cell limit. A preliminary test was run with the same conditions from the sector geometry legitimacy test to determine an approximate flame thickness of 3-4 mm. A somewhat arbitrary initial target mesh resolution of 10-15 grid cells across the flame thickness was determined and from it, a starting base cell side length of 0.3250 mm. SI simulations were run with incrementally increasing AMR level and domain cell count limit, as specified in Table 2.

Table 2. Grid resolution sensitivity analysis case points. AMR level varied with base grid size and cell limit to promote load balancing.

Case	AMR Level	Base Grid (mm)	Max Resolution (mm)	Cell Limit
1	0	0.3250	**0.3250**	Fixed: 237,000
2	1	0.4330	**0.2165**	250,000
3	2	0.4330	**0.1083**	500,000
4	3	0.4330	**0.0541**	1,000,000

Case 4, featuring the highest AMR and cell count limit of the set, resulted in a resolution of 14 cells across the reaction zone, as depicted in Figure 17. This resolution is assumed to be sufficient for accurate prediction of species diffusion and chemical reaction rates and serves as the baseline case for the other lower resolution cases to be compared to. Figure 18 depicts how the pressure and HRR predictions vary with grid resolution.

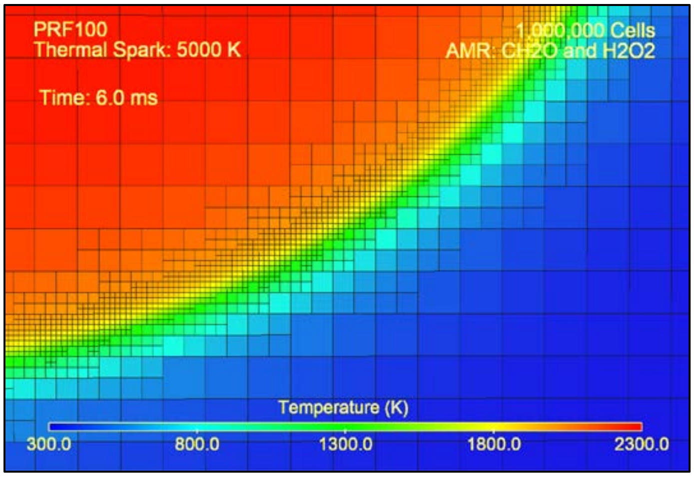

Figure 17. Two-dimensional cross-section view of a spherical propagating flame in premixed stoichiometric isooctane and air. Zoomed view to better depict the resolution in the area of the reaction zone. AMR level: 3. Cell count limit: 1,000,000. Orthogonal mesh represented by black grid lines. Image colored by temperature.

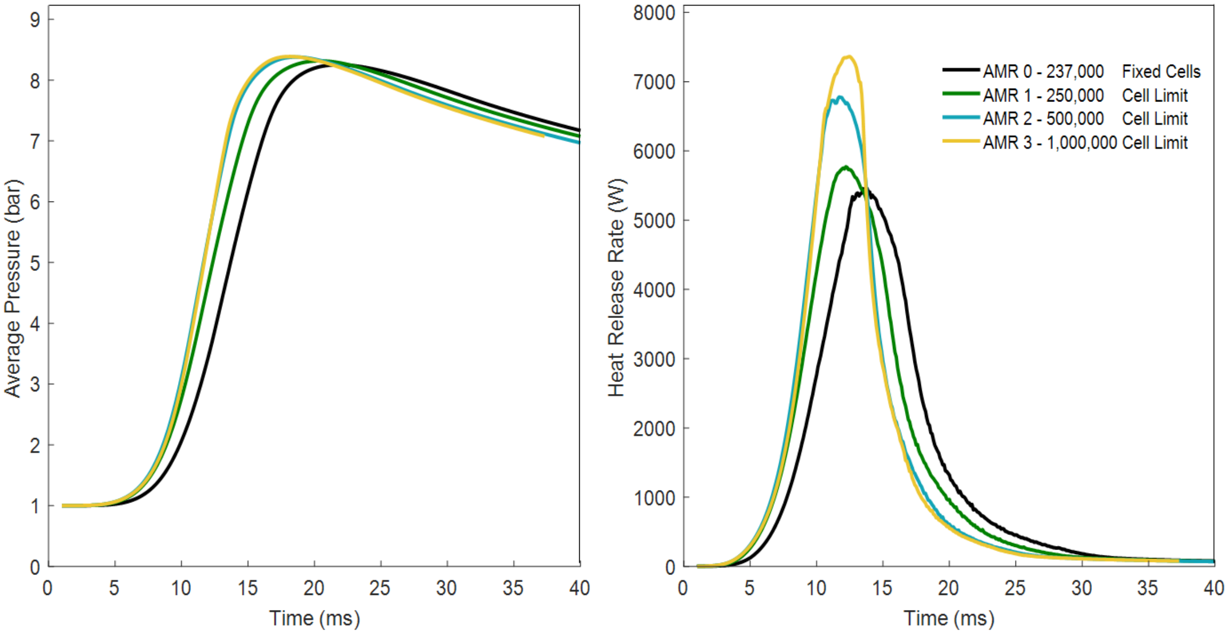

Figure 18. Pressure and HRR predictions of the four cases in the grid resolution sensitivity study.

The model's sensitivity to grid resolution is apparent, with higher resolution cases predicting higher peak HRRs and faster pressure rise rates. As resolution is increased to the extreme, differences between cases begin to diminish – a strong indication that sufficient grid resolution has been reached. Of most significance is the convergence of predicted pressure and

HRR profiles for the cases featuring AMR levels of 2 and 3 (cases 3 and 4 in Table 2). Here, the lower resolution AMR 2 case returns nearly the same result as the baseline AMR 3, but with half the resolution and therefore significantly less computational expense. From this sensitivity study, it was determined that a base cell dimension of 0.433 mm with level 2 AMR is most appropriate for the RCM simulations.

To ensure that the grid could appropriately model the boundary layer for the turbulent length scales near the chamber walls, level 2 fixed embedding was activated at a depth of two cell layers adjacent to every chamber surface. Preliminary RCM compression simulations were run and the resulting wall y+ values measured. Target y+ values for the k-ε turbulence model are less than 10 [22]. Cells at the crevice volume channel inlet exceeded the y+ target bounds during compression in the preliminary run. Fixed embedding was increased to level 3 in these regions in response, which brought y+ values into the appropriate range. Modifying grid resolution near the chamber boundaries affects the modeled volume and therefore trapped mass contained within the chamber. After the fixed embedding levels were finalized, the TDC and BDC chamber volumes were checked to ensure that trapped mass and compression ratio were maintained to an acceptable degree.

4.3 Compression Event Modeling

Combustion phenomena in both the experiments and models were found to be extremely sensitive to the pressure/temperature history of the compression events. As such, the quality with which the compression events are modeled directly determines the resulting agreement between the models and experiments. This section discusses the strategies implemented for matching compression pressure time histories in both the symmetric and asymmetric models.

Symmetric models use the motion of only one piston to simulate the volume change with time during a compression event that in reality is caused by the motion of two pistons. Piston offset cannot be accounted for in this way, so modeling efforts are directed to experimental trials that feature minimum piston offset (less than 1.0 ms). The user defined function (UDF) that specifies the piston position with time (and therefore its motion) is constructed using known geometric dimensions of the combustion chamber and the isentropic compression assumption that results in Equation 11 [26].

$$\frac{P_2}{P_1} = \left(\frac{v_1}{v_2}\right)^{\gamma} \tag{11}$$

With the measured pressure time history for the compression event in the experiment discretized into a reasonable number of sample points (~50), the apparent volume during compression can be approximated. The volume is apparent, as heat transfer causes lower measured pressures for an equivalent volume change relative to the isentropic compression assumption. This assumption introduces error that must be accounted for in an iterative process. From the final apparent volume time history, the dependent position of the piston in the symmetric model is derived.

Asymmetric models are constructed with a more direct approach, using the measured piston position data for a selected representative experimental trial. The LVDTs on the backside of the piston/plunger assemblies measure the piston positions with time during the compression event. This data is imported into a MATLAB script that makes modifications to the linear position curves to correct for signal noise and measurement degradation.

The RCM's LVDTs work well to show rapid position change with time, but exhibit fair uncertainty as the pistons reach TDC and begin to slow. Third-order polynomials are fit to the curves and a fixed stroke is forced to correct for the resulting error. As such, asymmetric compression modeling is also an iterative process. To derive the third-order polynomial, the pressure history of the initial simulation is compared to that of the experiment. Differences between the two are used to derive a time correction factor for the piston positions. This is accomplished through a comparison of the time at which the simulation reaches a given pressure to when the experiment reaches the same pressure. Over the extent of the entire curve, the time differences for each discrete pressure are used to derive a third order correction equation that acts upon the time data of the simulation [13]. Figure 19 shows how error in the pressure history of the initial simulation is corrected for using this strategy.

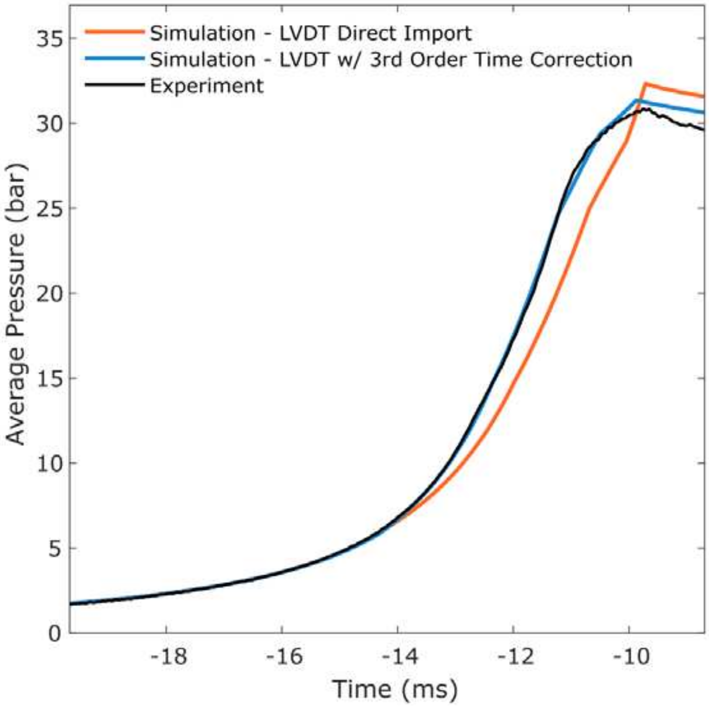

Figure 19. Example of the asymmetric compression event matching iterative process. Time axis listed as ms before spark ignition. Only the compression curve is shown. The initial simulation, shown in orange, was constructed using the LVDT piston position measurements from the experiment. The second simulation, shown in blue, features a slightly lower compression ratio, with LVDT time data adjusted via a third-order polynomial correction equation.

The result of the asymmetric compression modeling technique is highly accurate temperature history replication. Figure 20 features a comparison of the best compression pressure history matching results from the symmetric and asymmetric modeling techniques. The relative accuracy of the asymmetric modeling approach is clearly depicted. In theory, a symmetric compression model could achieve this same level of agreement with a specific experiment, but the means by which such a model would be constructed would be far more complicated and labor intensive than is the construction of the asymmetric model.

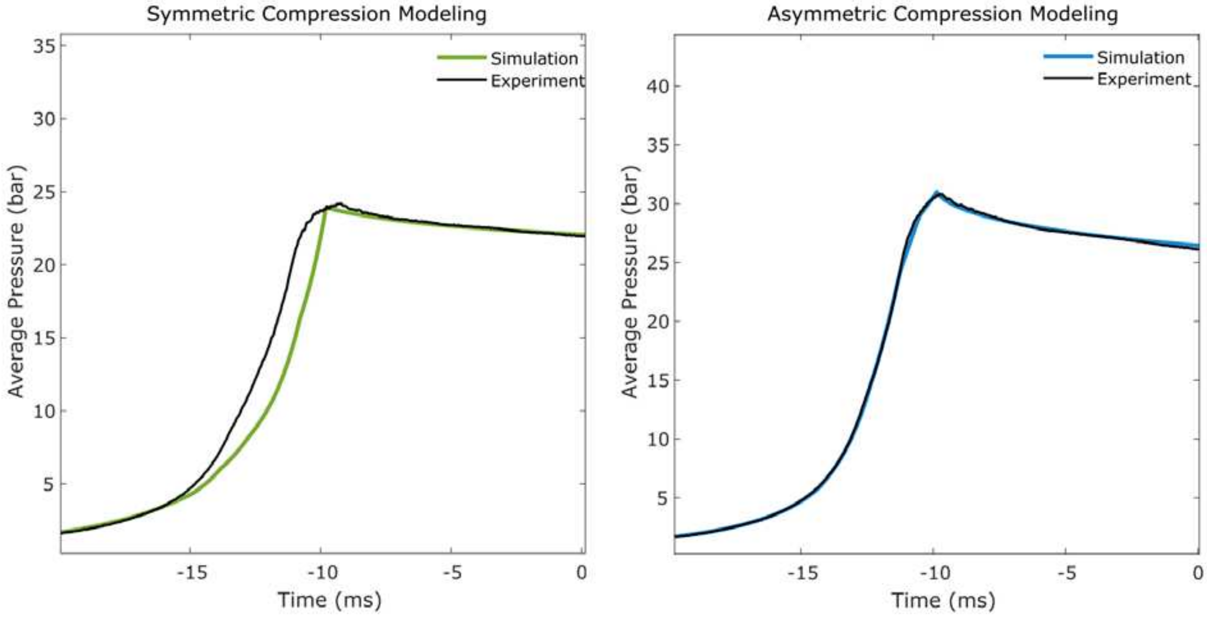

Figure 20. Comparison of the simulation/experiment agreement for the symmetric and asymmetric compression modeling strategies.

In summary, symmetric compression modeling offers the benefit of reducing the domain size and modeling effort once the general model has been constructed. This method works well for investigating how changes to thermodynamic or fuel reactivity conditions would affect combustion phenomena for equivalent compression events. It is not able to account for the differences in compression speed and symmetry that are frequently observed in RCM experiments, and thus results in noticeable differences between experimental pressure curves and those simulated. The asymmetric models require substantial modeling effort, but can closely replicate the experimentally observed results.

Mass loss during compression can be accounted for in either strategy with an energy balance or UDF in the CONVERGE interface. However, this quantity varies significantly from one experiment to another, as leak pathways in the chamber accessories and piston seals appear and are mended frequently. Measuring mass loss for every experimental trial is prohibitively time consuming and an average mass loss approach is preferred. The added degree of uncertainty introduced to the model with mass loss equations was found to be more burdensome than it was useful. It was therefore abandoned early on in the model construction process.

Also critical to matching the temperature history of a compression event are the model's heat transfer rate predictions. CONVERGE simulations are designed for steady state reciprocating engine operation in which there are high levels of turbulence. The RCM is by intention a low turbulence inducing machine and heat transfer rates tend to be underpredicted in the models, because conditions are outside the range for which the heat transfer models were tuned. The Han and Reitz turbulent heat transfer model is employed for the majority of the simulations as it was found to outperform CONVERGE's default O'Rourke and Amsden model for RCM experiments. Still, heat transfer rate calibration is necessary.

As a means of compensation for the under-prediction of heat transfer rate, turbulent kinetic energy (TKE) levels are adjusted after the pistons reach their TDC positions on the compression stroke. This is done to match the experimentally observed pressure decline rate between the times of TDC and ignition. This calibration process is ad hoc for a single experimental trial, but the factor by which TKE is adjusted remains unchanged for a larger simulation set. That is, the model is calibrated once, and then used for the other simulation conditions so as to not introduce bias into the results. Figure 21 shows a comparison of the pressure time histories for increasing levels of mapped TKE scale. With increasing TKE scaling factors, the simulated pressure curves approach those of the experiment, with increasing TKE having a diminishing effect.

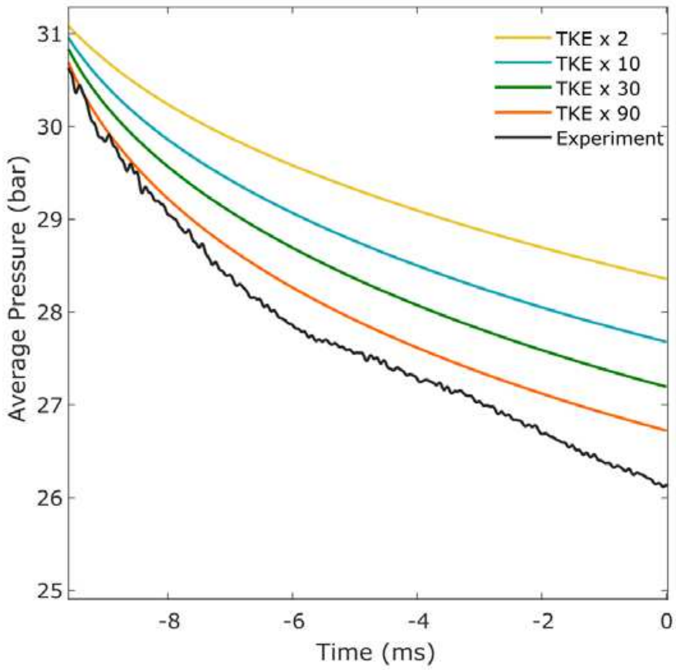

Figure 21. The effect of scaling TKE levels on heat transfer rate, as depicted by pressure decrease rates between the times of TDC and ignition.

Where this calibration technique is applied, TKE is increased by a factor of 90. This value was found to result in the closest rate of heat transfer to the experiments without introducing non-physical combustion results. Increasing TKE level was found to increase the predicted flame propagation rates, as would be expected. This, in fact, resulted in closer agreement with the experimentally observed propagation rates and as such the TKE scaling method is considered valid.

It is expected that using a more sophisticated turbulence model (e.g. large eddy simulation or direct numerical simulation) would result in more accurate TKE distributions and therefore heat transfer rates, but these methods are prohibitively expensive for the computational budget currently allotted. Adjusting the heat transfer rate constants for the models is also possible, but would perhaps diminish the physical causes of the higher heat transfer rates observed.

4.4 Spark Modeling

Two spark modeling strategies were investigated: point energy sourcing and thermal hotspot initialization. Reliable ignition is achieved using both strategies, but thermal hotspot ignition resulted in more realistic flame propagation rate behavior and was therefore used in the majority of the simulations presented herein. This section discusses the execution of both ignition strategies and their respective advantages.

Energy source ignition is achieved with built in functions in the CONVERGE platform. A finite amount of energy is introduced to a user-specified volume within the domain over time. This method is robust and widely applicable as modifications to the domain are not required for its utilization. The amount of energy added to the system via spark can easily be adjusted to match experiments and ensure that flames are not unrealistically “boosted” upon ignition. That aside, preliminary simulations revealed unusual clover shaped flame volumes resulting from the energy source method – see Figure 22.

Such flame irregularities have never been observed experimentally and seem to be the result of unevenly distributed energy sourcing or insufficient resolution of the user-specified spark volume. Both variables are outside of the user’s control, but the irregularities that are introduced are significant. Spark shape directly determines the shape of the resulting flame, which in turn impacts the dynamics of unburned reactant consumption and the amount of end-gas that will eventually undergo autoignition. It is of crucial importance, then, to establish means of ignition that result in realistic flame propagation behavior. Point energy sourcing is a convenient method of spark modeling as it requires little effort to introduce into the simulation, but because of the observed irregularities, it is not employed in any of the final models featured.

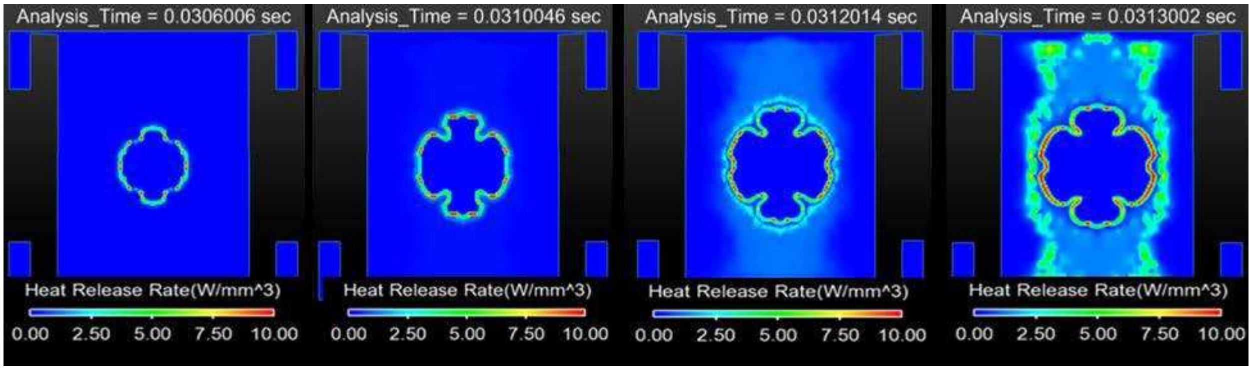

Figure 22. Example of non-physical clover shape flame propagation in early RCM models. Images colored by volumetric heat release rate to visualize combustion progression. Computations performed by Siddhesh Bhoite in 2017 [14].

Thermal hotspot initialization was found to produce more realistic flame propagation shape at the expense of increased modeling effort. The desired outcome is simple – initiate a small volume within the domain at high temperature at a specified time. The method behind doing so is complex, however, as it is not built into the CONVERGE platform like energy source modeling is. The domain is first modified with a boundary to define the spark shape. A 1.000 mm diameter sphere composed of 3712 triangles is used in the RCM model. That boundary must be continuous with all other surfaces in the domain such that the STL files that CONVERGE uses to create the grid feature no overlapping triangles at any time during the simulation. This is complicated by the changing relative distances of the spark boundary with the moving piston surfaces during compression. Figure 23 shows how the RCM domain was modified to include a spark sphere while maintaining continuity with other chamber boundaries.

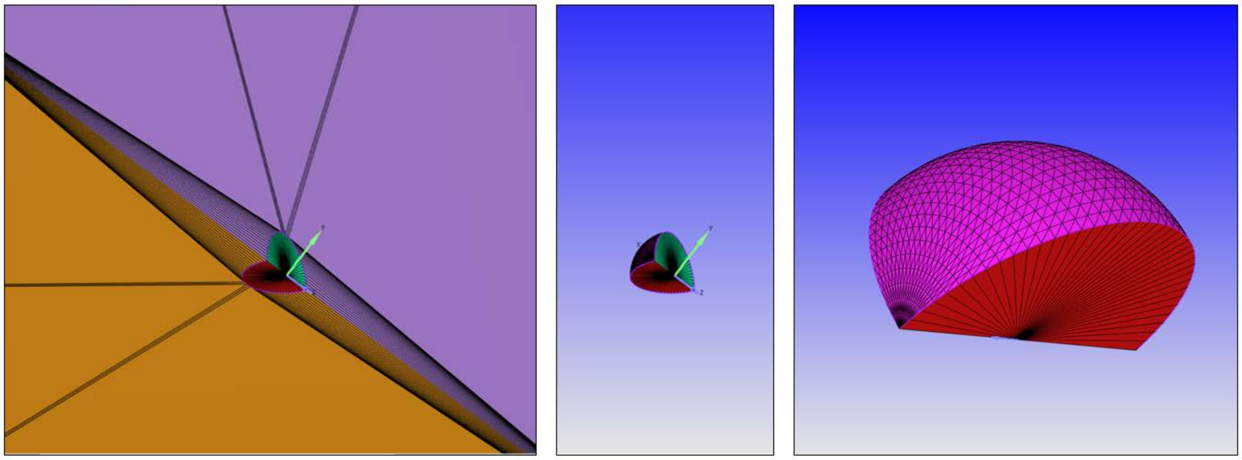

Figure 23. Spark sphere boundary modification to RCM computational domain. The sector's periodic boundaries are shown in the leftmost image in purple and orange – see Figure 13 for a more complete picture of the domain. High aspect ratio surface triangles, outlined in black, create continuity between the spark sphere and the surrounding boundaries. Spark sphere flow-through and periodic boundaries more clearly represented in the isolated and zoomed images.

The volume within the spark boundary is initialized with the rest of the chamber at the start of the simulation. It is kept open as a flow-through boundary during both compression and combustion, but at the time of ignition the spark boundary is closed, initialized with a high temperature, and then reopened. Initialization with this method is instantaneous as far as the physics are concerned, but it cannot be performed automatically. The simulation must stop just before ignition for a spatial map of the tracked variables to be recorded. A new domain is initialized with the spatial map, the spark volume temperature is set, and the simulation is restarted. This procedure is labor intensive, but the resulting combustion phenomena are absent from propagation irregularities and accord more closely with experimental observations. It is therefore the preferred ignition method and is used in all but the most preliminary of simulations.

The appropriate spark initialization temperature was determined via sensitivity analysis. Extremely high spark temperatures (> 15,000 K) create numerical instabilities in the model and prevent convergence. Conversely, low spark temperatures risk failure of combustion initiation altogether. Spark initialization temperature was swept from 1,000 to 10,000 K for a spark sphere of 1.000 mm diameter, in the test domain presented earlier. The affect of increasing spark temperature on AHRR is captured in Figure 24.

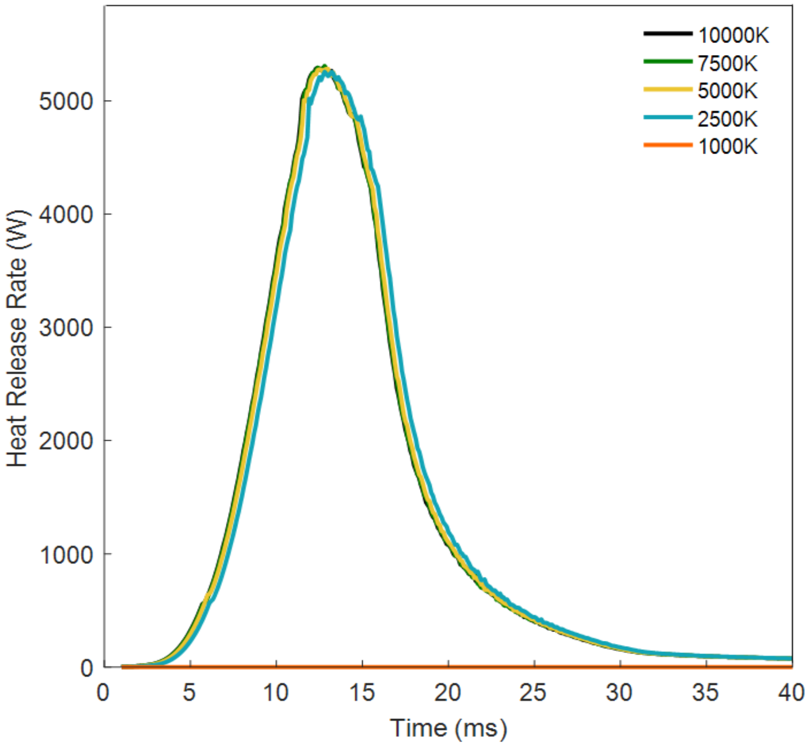

Figure 24. HRR results capturing model sensitivity to increasing spark temperature. 1/8th sector simplified cylindrical domain. Premixed isooctane and air at stoichiometric proportion with the 72 – Wang mechanism. Initial pressure and temperature at 1 bar and 298 K. Ignition occurs at t = 1.0 ms.

Increasing spark volume temperature raises the amount of energy added to the system via spark initialization, but does not seem to have much influence over the predicted HRR once spark temperature reaches a sufficient ignition temperature. It was found that reliable, numerically stable ignition is best achieved with a spark temperature of 5000 K.

4.6 Crevice Volume and Region-Specific Combustion

Crevice volume combustion is characterized by reactant consumption in the crevice volumes located behind the piston faces (i.e. combustion outside of the main chamber). Its occurrence presents a challenge to the method of identifying combustion mode with AHRR signatures, as it could potentially be misidentified as EGAI if the two combustion modes occur simultaneously. This issue is discussed at length in §5.5. Though analysis of the larger experimental data set provides no evidence of this behavior, simulations can help determine how crevice volume combustion could manifest and inform the interpretation of AHRR signatures. It is of interest, then, to develop a model in which crevice volume combustion can be prevented or allowed to occur for comparison purposes.

It is believed that a propagating flame would be quenched at the narrow channel connecting the main chamber to the crevice volume. This channel is 0.2 mm wide at its most narrow point with a depth of 4.000 mm. The RCM simulations, employing SAGE combustion models, consistently show the flame travelling through this channel unobstructed, however. Given the wealth of experimental evidence and practical reasoning to support quenching at the channel, a model must be developed that forces a quench condition at the crevice volume inlet. Region specific combustion, in which combustion modeling is independently activated or deactivated in a region, is what makes this possible. The validity of the forced quench condition will be evaluated through comparison to experimental data in §6.1 and §6.2.

Flow-through boundaries, similar to those making thermal hotspot ignition possible, are used to delimit the crevice volume region from the main chamber. Molecular diffusion, bulk fluid motion, and heat transfer are left unaffected by the flow-through boundaries, but the regions adjacent to them are considered by the CONVERGE software to be independent of one another. Once discretized, combustion modeling can be activated in the main chamber and deactivated in the crevice volume to force the quench condition at the crevice volume channel.

Other forms of crevice volume ignition physics are possible. High-temperature jets could source the crevice volumes after a strong EGAI event, such that combustion is in fact quenched at the channel inlet, but is reinitiated in the crevice volumes afterward. Fuel reactivity and thermodynamic condition could be so extreme as to cause autoignition in the crevice volumes as well. These physics will be described at length in §5.5. With region-specific combustion capability in the computational models, these phenomena can and will be investigated.

4.7 Data Analysis and Post Processing

Of final concern is facilitating fair comparison between the experimental data and simulation results. Care is taken to ensure that data is gathered and derived in the same fashion for both data sets. This matters most in the AHRR calculations that are highly sensitive to method, sampling rate, and the location at which pressure data is measured.

More information is available about the simulations than the experiments and error could result from comparison of the true HRRs of the simulations to the AHRRs of the experiments. The true HRR from the simulations can be gathered via a summation of the chemical source term throughout the domain. Alternatively, the AHRR could be more accurately derived using the actual ratios of specific heat, rather than those estimated in the experiments. To avoid error introduced by modification to derivation method, the simulation AHRRs are calculated in the exact manner as in the experiments. That is, the specific heat ratio is estimated for the instantaneous temperature and the starting molecular composition and AHRR is derived from the measured rate of pressure change with time. Data sampling rate also has a strong impact on the calculated AHRRs through its influence on the resolution of the pressure derivative. To avoid this, the simulation sampling rate is set to match that of the experiment DAQ system – 2 MHz.

Last, the default output pressure from CONVERGE is a volume averaged term taken for the entire domain. In the experiments, pressure is measured at a fixed point and the volume averaged term is unavailable. Volume averaged pressure sampling in the simulations reduces the detected pressure oscillations caused by EGAI and therefore introduces significant comparison error with the experiments. To prevent this, pressure is sampled at a fixed location on the outside periphery of the chamber domain, similar to the experiment’s pressure transducer location, and then processed via the same data filtering techniques as the experiment.

CHAPTER 5 – EXPERIMENTAL RESULTS

Laser-ignited RCM experiments were conducted for the initial conditions presented in §3.1, and reproduced below. The full data set is composed of 186 trials that collectively shed light on EGAI physics and its sensitivities. This section discusses the experiment's findings, their implications, and the remaining challenges facing the development of the RCM into an instrument dedicated to knock propensity measurement.

5.1 Pressure, AHRR, and f_{EGAI} Measurements

The initial conditions used for the laser-ignited RCM experiments are presented in Table 2 below (note that this is the same table as in §3.1 and has been included here for ease of reference). For experiment indices 1-3, the thermodynamic conditions after compression were altered by adjusting the initial pressure. For indices 4-6, conditions were altered by adjustment of the inert composition. All experiments were performed with stoichiometric fuel/oxidizer blends.

The TDC temperatures and pressures listed in Table 3 represent the range observed experimentally for the specified initial conditions. Despite the use of six discrete initial conditions, there is much overlap of the TDC temperatures and pressures. TDC condition grouping strategies are implemented to account for differences in compression temperature history and turbulence level of the flow field, as discussed in §3.1. While turbulence intensity was not quantified in the experiments, the schlieren imaging results indicated that experiments with larger piston offset had increased convective velocity in the flow field after TDC. However, the data in Figure 25 indicate that the time-integrated temperature was not found to correlate with the piston offset. Therefore, in the discussions that follow, these data are taken to be the independent variables to which the dependent variables (e.g., f_{EGAI}, flame propagation rate) are compared.

Table 3. The six initial conditions used for the laser-ignited RCM tests. TDC temperatures were estimated using the ideal gas law with the known gas composition, initial temperature, pressure, and specific volume with time.

Index	Initial Pressure (bar)	Oxidizer/Inert Blend Composition (mole %) O2	N2	CO2	Compression Ratio (-)	TDC Temp. Range (K)	TDC Press. Range (bar)
1	1.000 ± 0.001	21%	79%	-	11.6:1	729 - 887	24.9 - 27.8
2	0.900 ± 0.001	21%	79%	-	11.6:1	730 - 867	22.7 - 25.7
3	0.750 ± 0.001	21%	79%	-	11.6:1	725 - 873	18.8 - 22.9
4	1.000 ± 0.001	21%	67.1%	11.9%	11.6:1	698 - 829	24.4 - 26.2
5	0.975 ± 0.075	21%	67.1%	11.9%	11.9:1	702 - 817	24.5 - 25.8
6	1.000 ± 0.001	21%	39.5%	39.5%	11.6:1	691 - 775	23.2 - 24.4

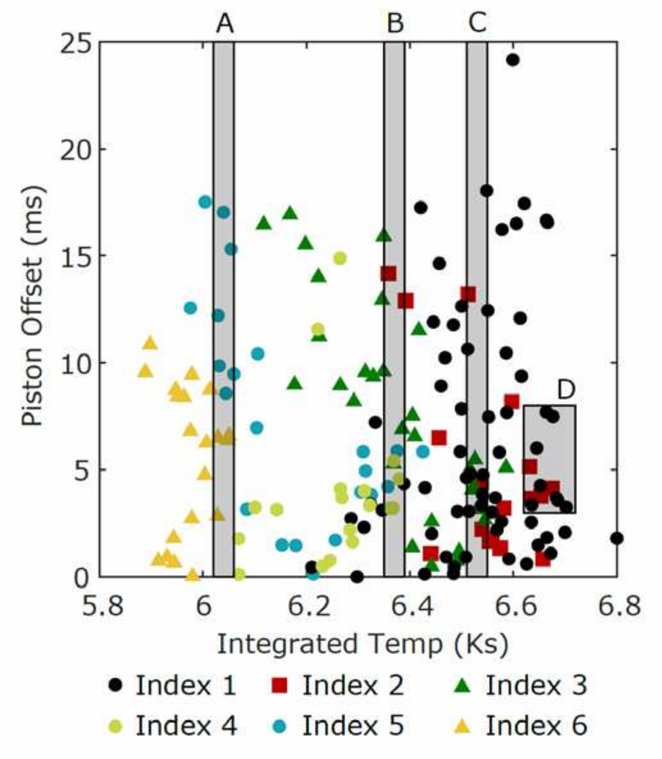

Figure 25. The TDC conditions of the entire data set, as represented by the time integrated temperature and piston offset of the compression events. Data markers colored by the initial condition indices listed in Table 3. Each data point represents a single experiment. All of the fuel blends and included. Integrated temperature summarizes the temperature history of the compression event. Piston offset indicates the level of turbulence induced by compression. The A,

B, C, and D shaded regions illustrate the TDC condition selection criteria for the data presented in Figure 26 and 27. Data points that fall within the shaded regions meet the selection criteria and are said to have been subjected to similar conditions upon compression.

Variability in TDC conditions brought about by inconsistencies in compression speed and symmetry is clearly depicted. Data point proximity on the TDC conditions plot Figure 25 is indicative of the similarity of the temperature and turbulence conditions between experiments. Experiments are grouped by the region of the plot that they occupy, and the similarity amongst the grouped experiments depends heavily on the size of the defined region. The A, B, C, and D selection criteria regions were selected so that, within each, the full range of tested fuel reactivity is represented and a sufficient number of data points is included.

Regions A, B, and C of the TDC conditions plot have been selected, as shaded, to represent how the SI combustion physics are affected by changing thermodynamic condition in the laser-ignited RCM experiments. AHRR data for PRF 100 experiments meeting the defined TDC condition criteria are plotted in Figure 26 and colored according to their respective regions.

The magnitude of the maximum AHRR for the PRF 100 fuel blend varied monotonically with the time integrated temperature of the compression event, as expected. The lower temperature experiments of Group A feature much longer combustion durations with no discernable EGAI signatures. The higher temperature experiments of Groups B and C exhibit a period of moderate AHRR followed by a dramatic change in the slope. Such behavior is indicative of an initial period in which heat release was produced by the spark-initiated propagating flame, which compressed the upstream unburned end-gases, and subsequently triggered EGAI.

It was found that SI flame propagation rate, and therefore EGAI timing, was highly dependent on the conditions of the flow field (i.e. turbulence level) as well. Region D of the TDC conditions plot enforces selection criteria for both temperature history (integrated temperature) and turbulence (piston offset). This facilitates fair comparison of the combustion characteristics of fuels with varying ON for the same set of compression conditions. AHRR data for experiments that met the Region D selection criteria are plotted in Figure 27.

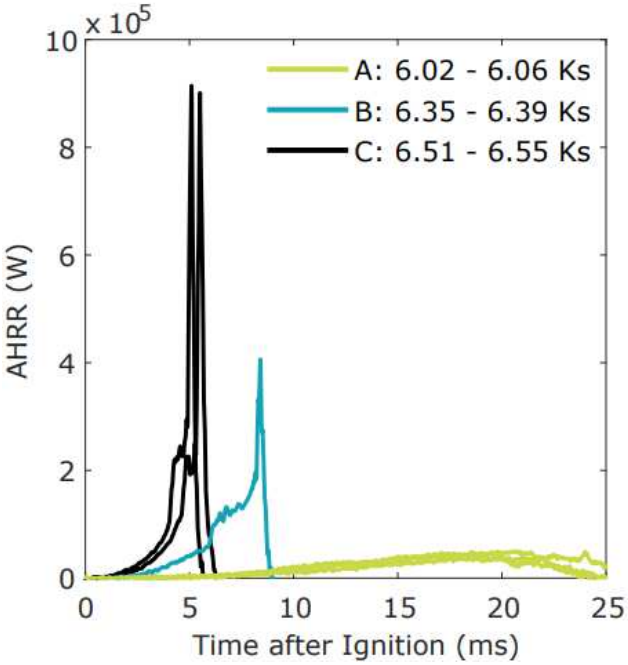

Figure 26. AHRR profiles of PRF 100 fuel blends that meet the A, B, and C TDC condition criteria defined by the shaded regions in Figure 25. Data colored according to the corresponding TDC condition region. Replicate trials shown. All initial condition indices included.

The timing of the observed EGAI events varied directly with ON and their magnitude varied inversely. Low-temperature chemistry results in two-stage ignition behavior evidenced by a local peak in AHRR prior to the primary EGAI peak. This behavior is most clearly depicted in the AHRR profiles of the higher reactivity blends. The inherent variability of the combustion phenomena, separate from compression inconsistency, is illustrated as well. Despite the installment of fairly strict selection criteria, the magnitude and timing of the volumetric heat release events is not perfectly consistent (see the PRF 70 trial that autoignites approximately 1 ms before the replicates of the group). Nonetheless, the integral role of a fuel’s knock propensity on its combustion behavior is clearly depicted. The higher the ON, the longer the autoignition chemical kinetic induction period, the more time for the SI flame to propagate prior to autoignition, and the less severe the resulting EGAI event. This effect is explored quantitatively through measurement of the EGAI fractions.

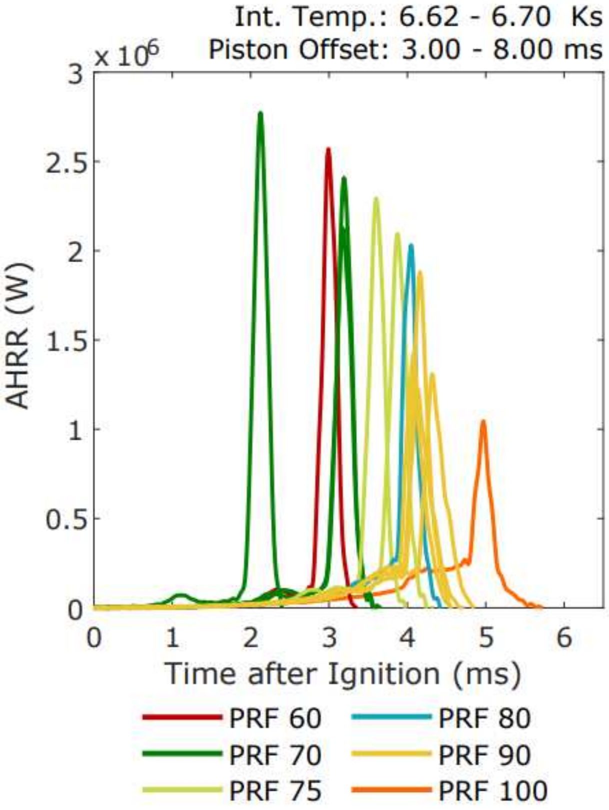

Figure 27. AHRR profiles of experiments that meet the TDC condition criteria defined by region D in Figure 25. Data colored according to the octane number of the tested fuel. Replicate trials shown. All initial condition indices included.

The fraction of the total apparent heat release attributed to EGAI, f_{EGAI}, was found to increase with increasing time-integrated temperature, Θ, and decrease non-linearly with increasing ON. EGAI fraction (f_{EGAI}) measurements for the six initial conditions listed in Table 3 are plotted independently against octane number in Figure 28. This is done in part to represent the relationship between ON and EGAI magnitude, but also to illustrate the shortcomings of the initial condition grouping method. There was an inverse correlation between octane number and f_{EGAI}, indicated by the the Spearman coefficient listed on each plot, but variability amongst trials of the same sort was present.

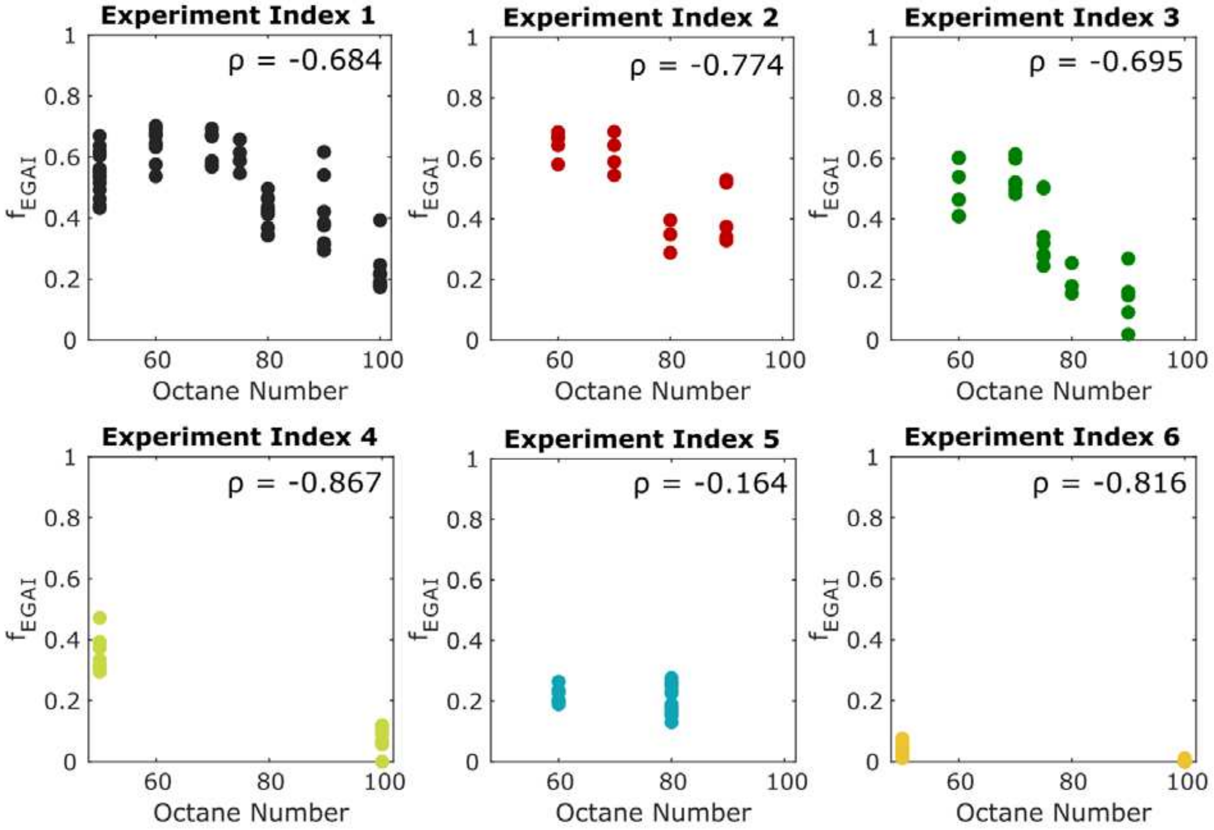

Figure 28. Variation in f_{EGAI} with octane number at each test condition defined in Table 3. Markers represent individual test replicates. The Spearman correlation coefficient is shown in the upper right corner of each graph to quantify the strength of the dependencies (note that the closer the coefficient is to 1 or -1, the stronger the dependency; the closer it is to 0, the weaker the dependency).

Here, with the experiments grouped by their initial conditions alone, the variability amongst trials of the same sort, the apparent discontinuities of f_{EGAI} between fuels of similar reactivities, and the overlap of trends of different experiment index builds a strong case for the TDC condition grouping methods. Trials do not cluster into the discrete groups that would be expected of a perfectly repeatable experiment, as the effects of initial condition and inert composition are blurred by compression inconsistency. TDC condition grouping techniques provide a much better representation of the trials that underwent similar experimental conditions.

Figure 29 includes the f_{EGAI} results for $50 < ON < 100$ for $\Theta = 6.04 \pm 0.02$ Ks, 6.37 ± 0.02 Ks, and 6.53 ± 0.02 Ks and all piston offsets (regions A, B, and C of Figure 25).

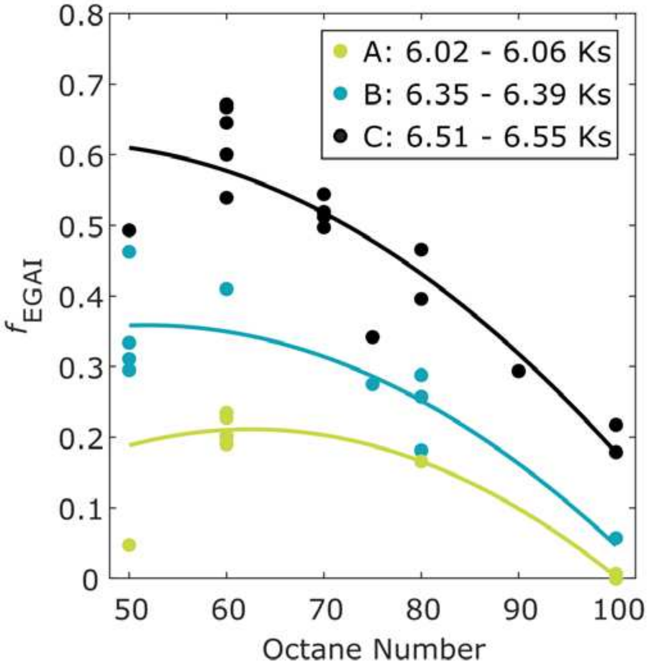

Figure 29. EGAI fraction (f_{EGAI}) measurements plotted against ON of the experiments that meet the TDC condition criteria defined by the A, B, and C shaded regions in Figure 25. Markers represent individual test replicates. Second order polynomials fit to the data using the least squares method.

Stronger trends emerge between f_{EGAI} and octane number once compression inconsistencies are accounted for. The f_{EGAI} metric proved sensitive to both temperature and fuel reactivity. The lower time integrated temperature groups feature EGAI events of lower magnitude, as do the experiments of lower fuel reactivity (i.e. higher ON). Second order polynomials are fit to the data as a loose representation of the trends. In theory, f_{EGAI} is bounded by 0 for the case in which no EGAI occurs and by 1 for the case in which volumetric autoignition consumes the entirety of the reactive mixture prior to the introduction of the spark (i.e. preignition). The trend between f_{EGAI} and ON is expected to be non-linear as it approaches either extreme.

Interestingly, the experimentally determined limit to the f_{EGAI} metric for PRF blends was found to be less than 1.0. Low-temperature volumetric chemistry with these fuels causes two-stage ignition behavior that disrupts the evaluation of the f_{EGAI} measurement. The low temperature combustion events that precede EGAI are responsible for some fraction of the total energy released but, by definition, are not considered part of the primary EGAI event. With that, even experiments in which volumetric combustion occurred prior to the spark (preignition) only reach an apparent f_{EGAI} of 0.70. This limitation is depicted by the leveling off of the f_{EGAI}, ON trends in the PRF 50 region of Figure 29.

Low-temperature chemistry manifests itself in the f_{EGAI} measurements as a local reversal of the inverse trend with octane number and as an overall limitation in f_{EGAI} for fuels that exhibit two-stage ignition characteristics. NTC chemistry may be more active in the PRF 50 region of the f_{EGAI} data in Figure 29, as indicated by the leveling off and possible reversal of the trends in that location. It is theorized that ignition delays for the PRF 50 blends are longer than those of the PRF 60 blends at the compressed temperatures presented. Should that be true, the propagating flame would be allowed to consume more of the reactive mixture prior to EGAI and a lower f_{EGAI} would be the result. However, the number of data points collected for the PRF 50 blends that met these test criteria is insufficient to draw any meaningful conclusions.

Spatial temperature gradients could complicate the NTC phenomenon further, as colder regions of the end-gas (e.g. in the thermal boundary layer or crevice volume) could autoignite before the rest of the chamber. Such an occurrence would still constitute as EGAI and would be detected by the AHRR signature, though it is unclear whether it could be distinguished from standard EGAI in the main chamber (see §6.1). Further still, cases in which the propagating flame enters a region of the end-gas where LTC is active are likely. Section 6.1 presents a simulated PRF

80, 5.88 Ks case in which LTHR is present, but the propagating flame is able to consume the entirety of the mixture prior to EGAI.

5.2 EGAI Sensitivity to Temperature History and Turbulence

To explore the effect of selection criteria stringency, Figure 30 features f_{EGAI} measurements across octane number for three integrated temperature ranges of varying width. The narrowest integrated temperature range identifies experiments that were subjected to compression events with highly similar temperature histories. Experiments meeting the defined criteria exhibit minimal f_{EGAI} variability and a strong correlation with octane number. As the integrated temperature range is widened, the criteria used to identify trials of the same sort becomes less strict and, with that, consistency of the f_{EGAI} measurements begins to diminish. This is especially true of the PRF 90 experiments that meet the criteria of the widest integrated temperature range. The integrated temperatures for these cases are distributed evenly throughout the shaded region, unlike the other fuel blends that are grouped closely together on the TDC conditions plot. The f_{EGAI} range of 0.10 to 0.68 for these PRF 90 experiments depicts the effect of using lenient selection criteria for compression temperature histories in full. Ultimately, a balance must be found between efforts of ensuring that grouped trials have been subjected to similar conditions and of maintaining a sizable enough dataset for interpretation.

Turbulence is the most significant governing factor of premixed flame propagation rate, as it is directly coupled with species diffusion rates and increasing the surface area of the propagating flame via “wrinkling.” Though turbulence is intended to be minimized with the RCM’s creviced pistons, piston offset during a compression event can introduce bulk fluid motion that cascades to small length scale turbulence. The result is a strong correlation between piston offset and SI flame propagation rate that will be covered in §5.3. Perfectly symmetrical compression events (i.e. piston offset is 0 ms) result in near quiescent adiabatic cores that have higher temperatures and lower turbulence levels relative to their asymmetric (i.e. piston offset > 5.0 ms) counterparts. Section 5.3 also covers flame propagation rates, their sensitivities, and their effects on f_{EGAI} and EGAI timing in more depth. What is of concern here is how piston offset selection criteria stringency may affect experiment grouping. This is explored by setting selection criteria bounds for piston offset with a narrow band of temperature history integration values, in Figure 31.

The effect of turbulence on combustion phenomena here is subtle. Absent consideration of NTC behavior, the phasing of the EGAI events over the range of fuel reactivity is expected to correlate with the tested fuel's ON. That is, fuels with lower reactivity (higher PRF number) should feature EGAI events that occur later than those of higher reactivity. Through the introduction of the strict selection criteria for integrated temperature history (6.530-6.550 Ks in Figure 31), the grouped trials are assumed to have been exposed to highly similar temperatures during compression and the effect of turbulence on the autoignition phasing is thus analyzed independently. With 2.50 – 5.00 ms piston offset selection criteria applied in the AHRR data of the left column of Figure 31, the expected phasing of the volumetric heat release events is captured. As that restriction is relaxed, two additional trials meet the selection criteria (one PRF 90 and one PRF 60) and disrupt the expected phasing.

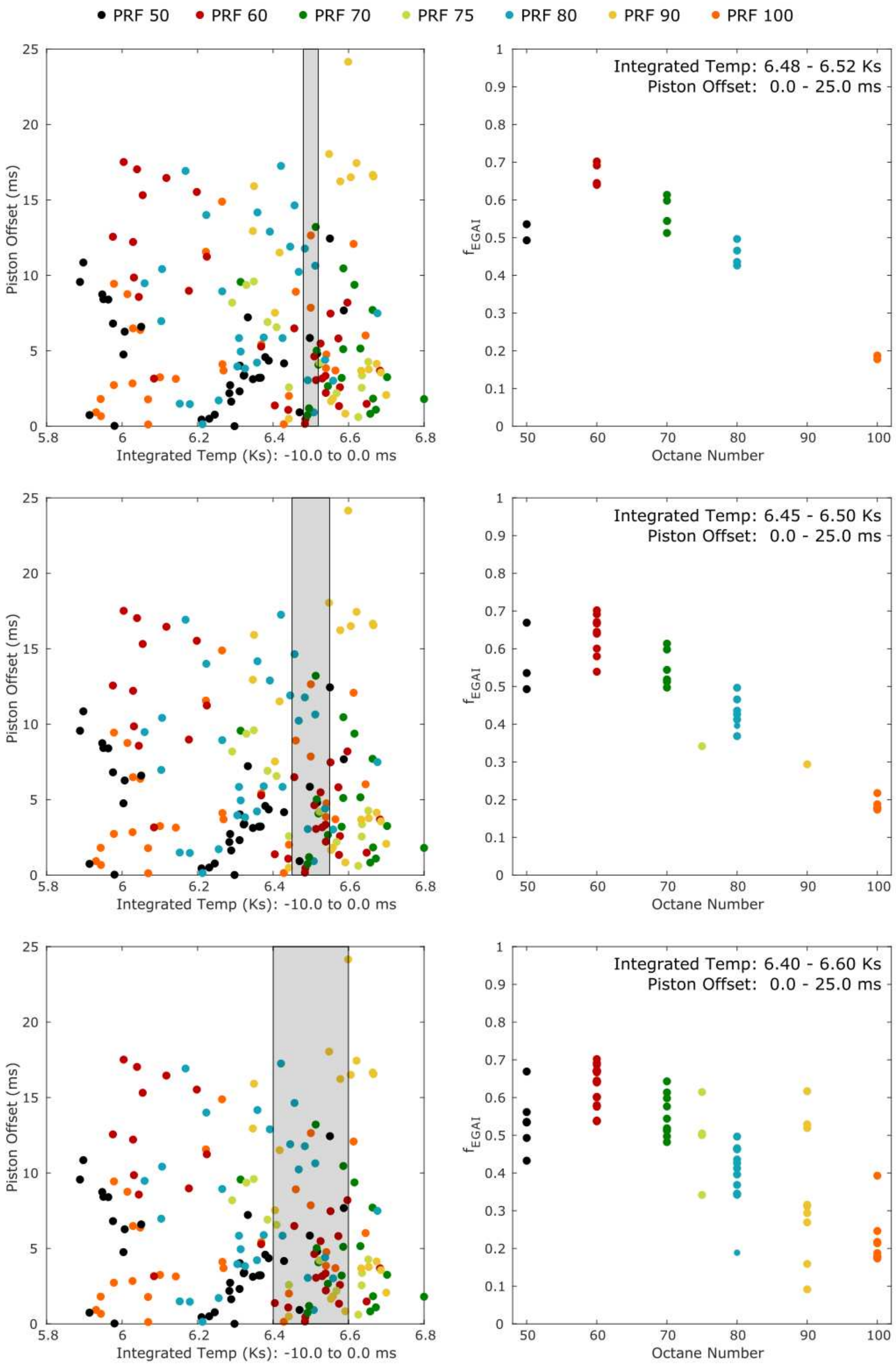
● PRF 50 ● PRF 60 ● PRF 70 ● PRF 75 ● PRF 80 ● PRF 90 ● PRF 100
Piston Offset (ms)
Integrated Temp (Ks): -10.0 to 0.0 ms
5.8 6 6.2 6.4 6.6 6.8
0 5 10 15 20 25
f_EGAI
Octane Number
50 60 70 80 90 100
0 0.1 0.2 0.3 0.4 0.5 0.6 0.7 0.8 0.9 1
Integrated Temp: 6.48 - 6.52 Ks
Piston Offset: 0.0 - 25.0 ms
Integrated Temp: 6.45 - 6.50 Ks
Piston Offset: 0.0 - 25.0 ms
Integrated Temp: 6.40 - 6.60 Ks
Piston Offset: 0.0 - 25.0 ms

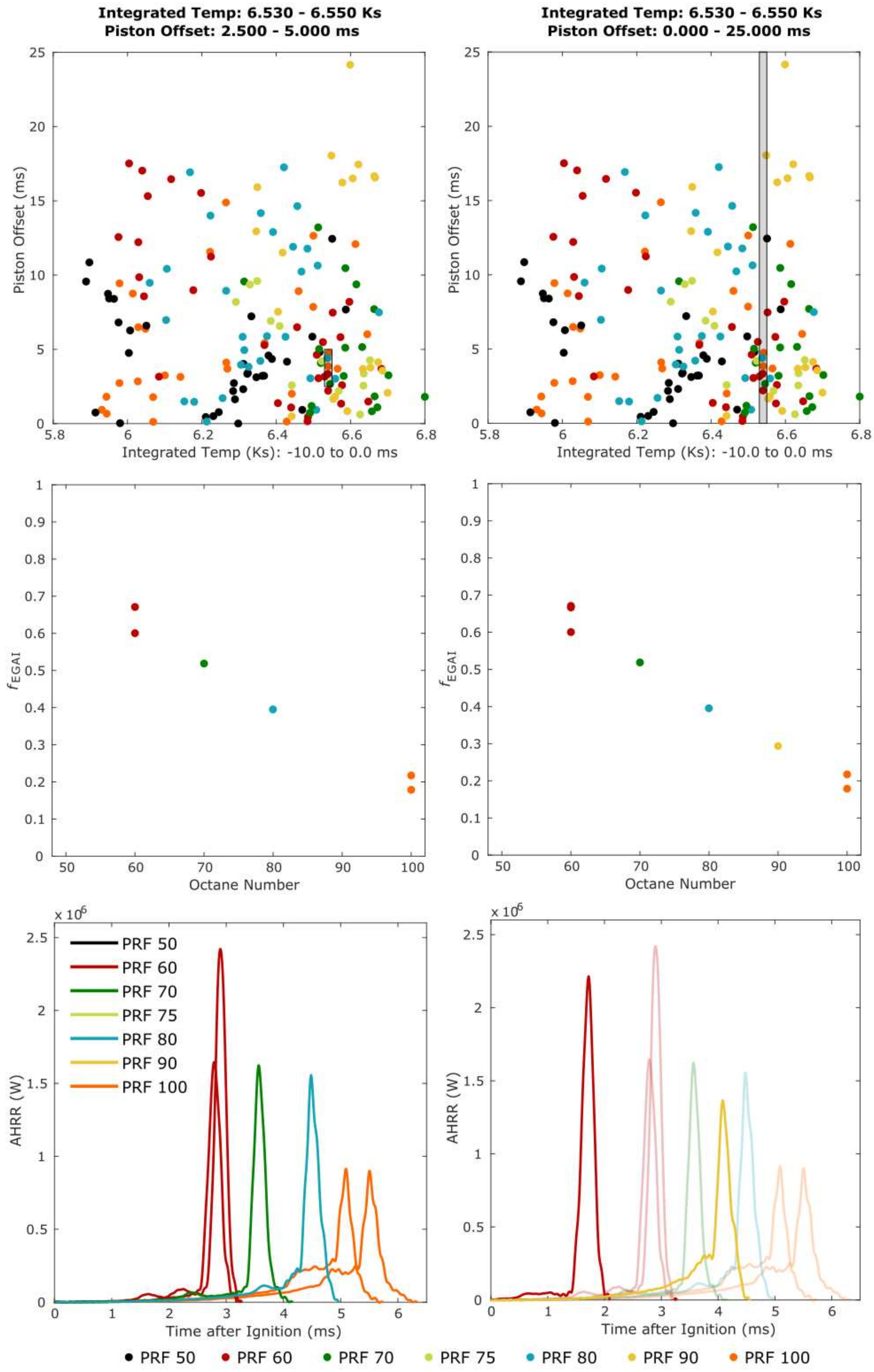
Integrated Temp: 6.530 - 6.550 Ks
Piston Offset: 2.500 - 5.000 ms
Integrated Temp: 6.530 - 6.550 Ks
Piston Offset: 0.000 - 25.000 ms
Piston Offset (ms)
Integrated Temp (Ks): -10.0 to 0.0 ms
0
5
10
15
20
25
5.8
6
6.2
6.4
6.6
6.8
f_{EGAI}
Octane Number
0
0.1
0.2
0.3
0.4
0.5
0.6
0.7
0.8
0.9
1
50
60
70
80
90
100
AHRR (W)
Time after Ignition (ms)
x 10^6
0
0.5
1
1.5
2
2.5
0
1
2
3
4
5
6
PRF 50
PRF 60
PRF 70
PRF 75
PRF 80
PRF 90
PRF 100
● PRF 50
● PRF 60
● PRF 70
● PRF 75
● PRF 80
● PRF 90
● PRF 100

Figure 30. (Page 70) F_{EGAI} measurements plotted against octane number for trials that meet the integrated temperature history requirements listed. The requirements are illustrated by the shaded regions in the corresponding TDC condition plot to the left of each f_{EGAI} plot. Experiments that fall within the shaded region meet the defined selection criteria and are plotted. Piston offset not controlled. Integrated temperature history bounded by the values listed. Markers colored by octane number.

Figure 31. (Page 71) F_{EGAI} measurements and AHRR signatures for trials that meet the listed integrated temperature history and piston offset criteria. Datasets are organized by column. Selection criteria illustrated by the shaded region in the TDC condition plots in the top row. Integrated temperature history criteria are the same for both data sets. Piston offset criteria imposed on the data in the left column of plots. Markers and lines colored by octane number. The colors of the AHRR signatures that are included in both sets are dulled on the bottom-right plot to accentuate differences.

The additional PRF 90 case features a much higher piston offset and a higher turbulence level is inferred for that case. It is thought that the higher turbulence level results in a faster flame propagation rate, which in turn compresses the end-gases at a faster rate and leads to earlier EGAI phasing (the PRF 90 EGAI event comes before that of the featured PRF 80 trial). The additional PRF 60 case, however, features the lowest piston offset of the group, but still exhibits earlier EGAI phasing than its replicate trials. These two observations contradict one another and seem speak more to the stochasticity of combustion phenomena rather than the role of turbulence in EGAI.

What is more, the f_{EGAI} trends with ON are entirely undisturbed by the changing piston offset selection criteria under these conditions. From that, it can be concluded that the magnitude of EGAI phenomena is much more sensitive to temperature than to flame speed. It is likely the case that SI flame propagation rate has a balanced influence on competing phenomena governing EGAI magnitude – the rate at which the reactants are consumed by the SI flame and the timing of EGAI events. This influence is assessed in detail in §5.3.

5.3 Flame Propagation and Sensitivities

This section focuses on the sensitivities of flame propagation rate in the laser-ignited RCM experiments and on the role of propagation rate in EGAI physics. To facilitate comparison, only experiments of the same initial condition are presented (index 1), so as to eliminate the effects of changing inert composition and gas density on diffusivity and propagation rates. Flame propagation rate measurements for index 1 experiments that featured piston offsets of less than 5.00 ms are listed in Table 4 with their corresponding measured pressures and estimated temperatures at the time of ignition.

Table 4. Unburned flame propagation rate measurements listed by their mean and standard deviations for the index 1 experiments (initial conditions: 300 K and 1.000 bar; oxidizer/inert molar composition: 21% O_2 / 79% N_2; stoichiometric). Only the experiments with piston offsets of less than 5.00 ms are included to ensure that the effect of turbulence is minimized. The number of measurements is included to indicate the level of confidence in the data. The "Simulated LFS" column features the predicted laminar flame speeds from the 1-D CHEMKIN simulations with 590 K and 22.5 bar ambient conditions.

PRF	# of Data Points	Temp. (K)	Pressure (bar)	Measured Prop. Rate (cm/s)		Simulated LFS (cm/s)
				Mean	SD	
50	6	571 ± 2	22.0 ± 0.2	63.3	15.0	52.5
60	4	598 ± 5	22.9 ± 0.2	80.3	6.3	51.1
70	1	614	23.8	83.5	-	50.4
75	4	605 ± 4	23.1 ± 0.2	62.5	4.1	50.2
80	3	591 ± 1	22.6 ± 0.0	65.1	10.5	49.7
90	3	612 ± 3	23.2 ± 0.1	63.3	13.9	49.2
100	5	589 ± 3	22.5 ± 0.2	65.1	8.3	48.5

These measurements have been converted from the observed burned propagation rates to the reported unburned propagation rates using Equation 10 from §3.4. Measurements are extrapolated to the zero-stretch condition using Equation 9. The measurements reported are higher than what is found in most of literature [27] for a number of reasons. First, piston offset induces variable levels of turbulence in the flow field thus affecting the mixing rate and effective flame surface area leading to higher propagation rates than what would be observed if the flow field were perfectly quiescent. Second, the temperatures and pressures at which the measurements are taken are considerably higher than what can be created through conventional means (i.e. with a spherical bomb). Initiating a bomb with these temperatures with premixed fuel and air would result in autoignition before any flame speed measurements could be taken. The laser-ignited RCM experiment is unique in that (1) the premixed test gases can be brought to high temperatures and pressures nearly instantaneously, allowing for flame propagation rate measurements to be taken prior to autoignition, and (2) the laser-ignition system does not interfere with the flow field upon initiating the premixed flame (as would an electrode). Thus, the ability to measure propagation rate at such extreme initial conditions is unique to this experimental setup and is of crucial importance to refining the understanding of SI ICE combustion.

Propagation rate was found to be correlated most strongly with piston offset, but also with temperature and pressure at the time of ignition to a lesser degree. Figure 32 presents propagation rate as the dependent variable to temperature, pressure, piston offset, and fuel reactivity. Temperatures at the time of ignition are presented in place of the time integrated temperature values used elsewhere because of the different combustion physics at play. That is, the propagation of a flame is governed by the instantaneous upstream temperatures because of its dependence on molecular diffusion. This is because the diffusion rate of a molecule is determined by its mass and instantaneous energy (temperature), whereas volumetric combustion chemistry is dependent on the time history of the temperature, as it is governed by the production of radical species.

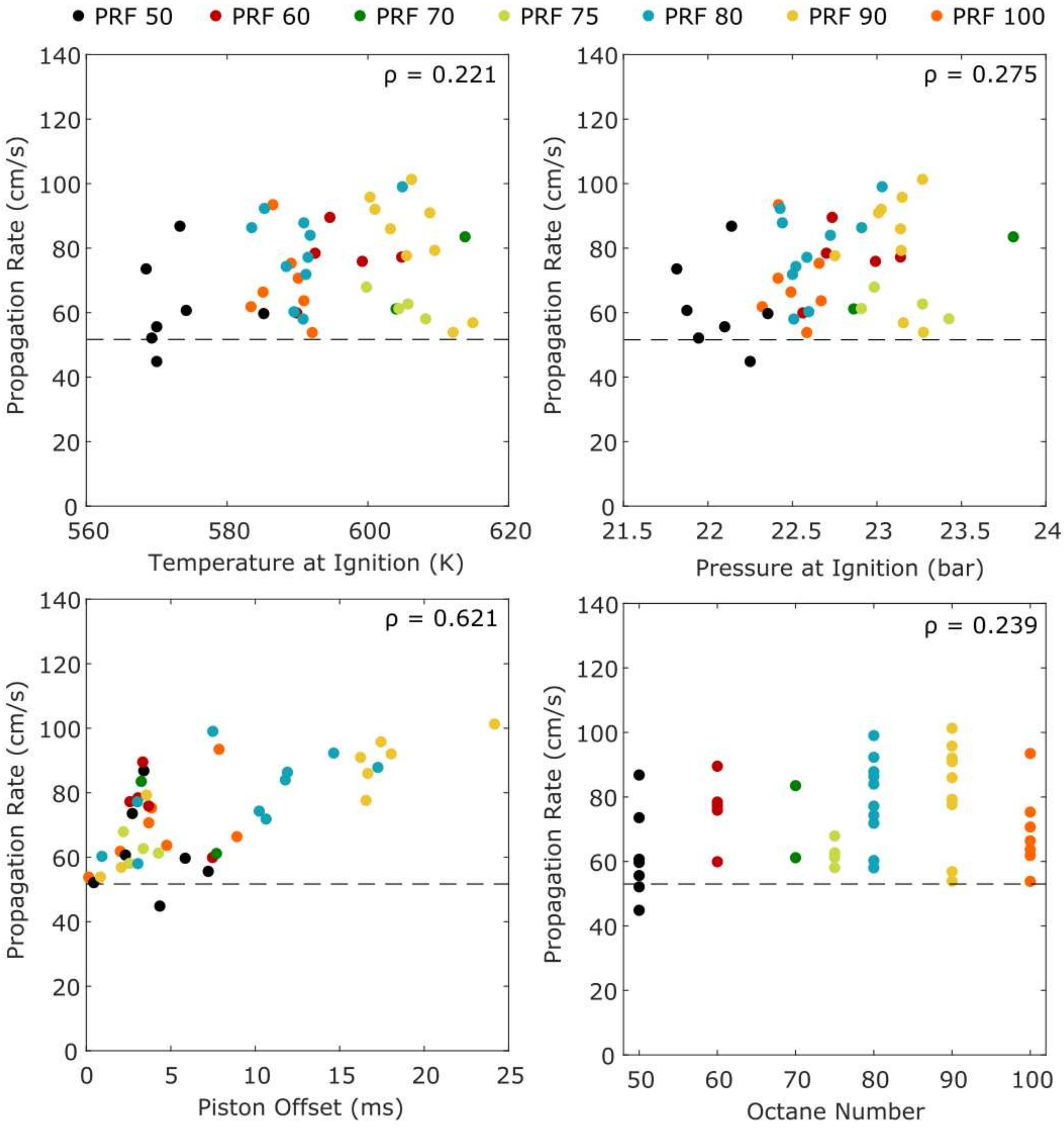

Figure 32. Unburned flame propagation rate presented as the dependent variable to estimated temperature, measured pressure, piston offset, and octane number of the fuel blend. Experiments conducted with the initial conditions listed under index 1. The average laminar flame speed of the simulations presented in Table 4 is represented by the dashed horizontal line in each plot. Spearman correlation coefficients included with each plot to show strength of dependency. Data markers colored by octane number.

Spearman rho correlation coefficients are included to quantify the strength of the dependencies (note that the closer the coefficient is to 1 or -1, the stronger the dependency; the closer it is to 0, the weaker the dependency). Temperature and pressure appear to have minimal effect on propagation rate over the ranges presented. It is expected that larger differences in those independent variables would produce more noticeable trends with propagation rate. Fuel reactivity appears to have no significant influence either – a finding that accords with the rest of literature [27]. In contrast, piston offset, as it indicates the relative level of turbulence in the flow field, has a strong influence over the propagation rate as quantified by the spearman coefficient of 0.679. As has been discussed, piston offset introduces bulk fluid motion during compression which cascades to produce small length scale, high kinetic energy turbulence. Turbulence in turn promotes mixing and increases the surface area of the flame, resulting in a faster propagation rate.

What is of most importance to the premise of the measurement technique is the fact that experiments with piston offsets approaching 0.0 ms feature propagation rates in close agreement with those of the 1-D laminar flame speed simulations. That is, cases with low piston offset offer quiescent flow-fields after compression that are host to near-laminar flames. Figure 32 features the measured propagation rates of the experiments performed under initial condition index 1 plotted against piston offset. The close agreement of the simulated average laminar flame speed (LFS), represented by the dashed horizontal line in Figure 32, and the y-axis intercept of the apparent trend between measured propagation rate and piston offset illustrates the validity of the measurement technique when near-symmetric compression is achieved

It is of interest to assess how strong of an influence SI flame propagation rate has on EGAI. In large, the magnitude of an EGAI event is determined by the outcome of a race between the propagating flame and the volumetric chemistry in the end-gas – the faster the propagation rate or the longer the autoignition delay, the more gas the flame can consume prior to autoignition and the lower the resulting *f*EGAI. The propagation rate and the ignition delay are also likely coupled, due to the compressive action of the flame on the end-gas. The degree to which the speed of the propagating flame determines the timing and magnitude of the EGAI event is captured in Figure 33 for experiments under initial condition index 1.

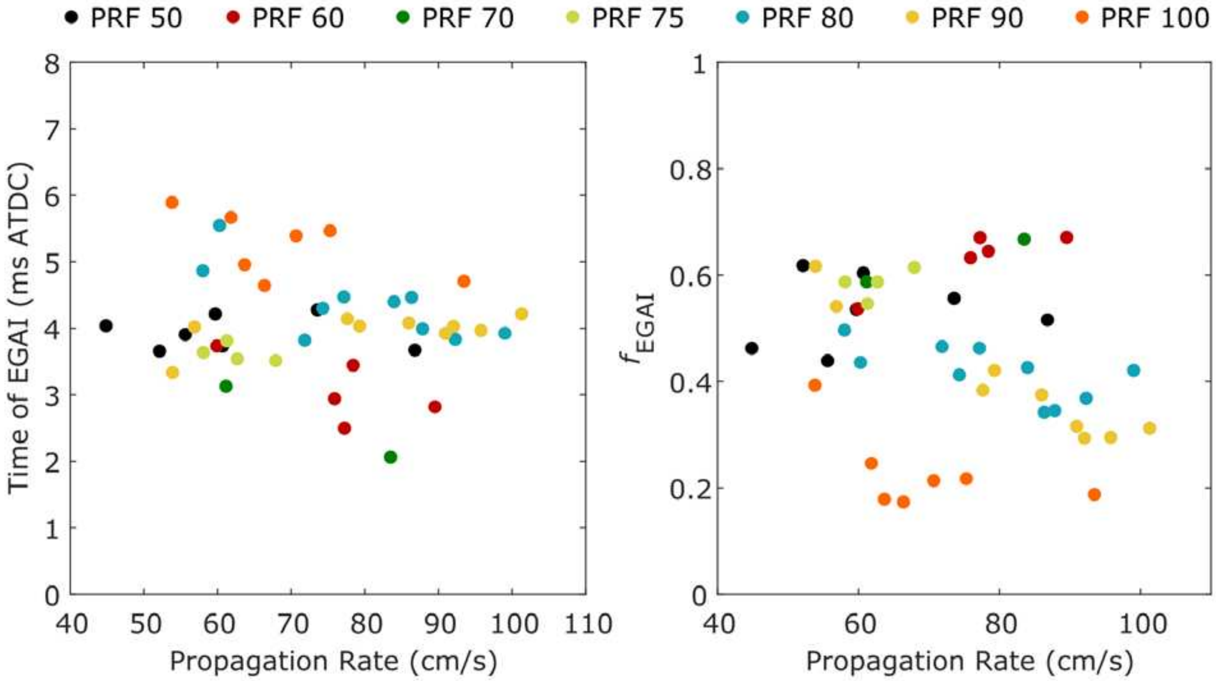

Figure 33. EGAI timing and fraction dependence on flame propagation rate. Spearman coefficients included for each fuel blend in Table 5 to assess dependency separate from fuel reactivity.

Strong inverse correlations between the propagation rate and *f*EGAI exist when fuels are considered independently from the rest of the group. The spearman rho coefficients capturing the strength of those correlations are listed in Table 5 for each fuel tested. The fuels are considered independently to eliminate the effects of changing the fuel reactivity on the magnitude and timing of the EGAI events, which would otherwise mislead interpretation.

Table 5. Spearman coefficients quantifying the strength of the dependencies between f_{EGAI}, time of EGAI, and propagation rate. Each fuel blend is listed separately to eliminate the influence of variation in fuel reactivity on results. The sample size collected is also listed to provide an indication of the strength of confidence in the reported numbers.

PRF	# of Data Points	Time of EGAI ρ	f_{EGAI} ρ
50	7	0.07	0.14
60	5	-0.50	0.90
70	2	-	-
75	4	-0.80	0.40
80	10	-0.55	-0.72
90	9	0.32	-0.92
100	7	-0.57	-0.43

Some fuels exhibit the expected trends between propagation rate and f_{EGAI} (PRF 80, 90, and 100). The faster the flame propagates, the more end-gas it can consume prior to autoignition, the lower the resulting f_{EGAI}. PRF 50, however, seems to depict that no correlation between EGAI timing and propagation rate exists, and other reactivities present the exact opposite trend. The correlations between propagation rate and EGAI timing are equally non-telling. The featured PRF 100 cases depict an inverse relationship – the faster the flame, the sooner EGAI occurs. This dependency can be explained by the faster rates of end-gas compression that are the result of the faster propagation rates, but other fuel reactivities seem to depict that no correlation between EGAI timing and propagation rate exists (PRFs 50, 60, 75, and 90). With that, the size of the dataset seems to be insufficient for meaningful interpretation.

Regardless of the strength of the correlation between propagation rate and EGAI timing, the logic that EGAI severity is governed by competition between propagating flame and end-gas chemistry is supported. Figure 34 depicts the dependency between EGAI timing and f_{EGAI} that is caused by the same physics as the theorized correlation between propagation rate and f_{EGAI}.

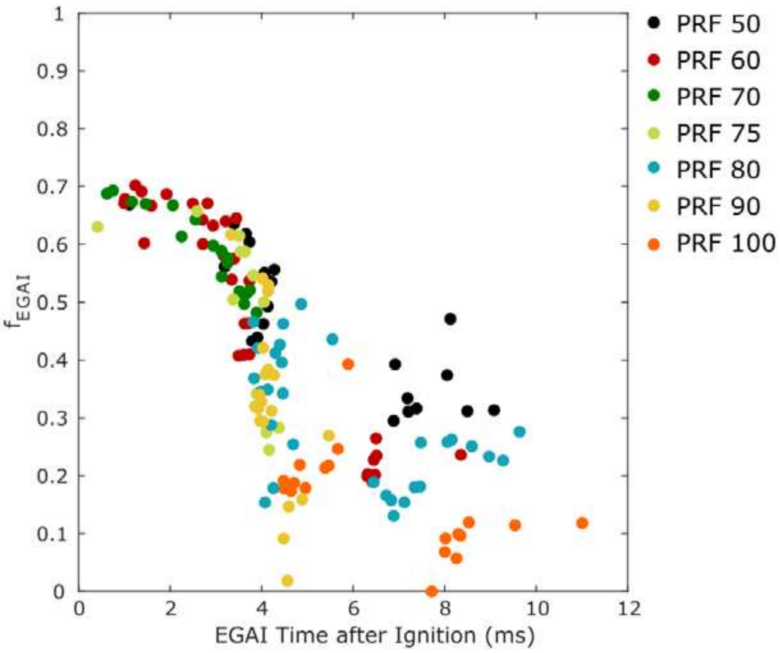

Figure 34. f_{EGAI} plotted against time at which the EGAI events occurred. Only trials in which EGAI was detected are included. Data markers colored by octane number.

The expected inverse trend between the two variables is present. Its non-linearity can be explained by the exponential growth of the flame surface area with time. Reactant consumption rate is governed in part by the flame surface area, and thereby also increases exponentially with time, explaining the steep drop off of f_{EGAI} with time. The disintegration of the trend with increasing EGAI time is likely explained by differences in turbulence level and compression temperature causing differences in flame propagation rate. Nonetheless, the theory that later phasing of the EGAI event allows for more of the reactants to be consumed by the flame holds true.

5.4 Observations of EGAI and Optical Identification of Combustion Mode

Select Schlieren images from a PRF 90, index 4 trial are shown in Figure 35. This trial was selected for the clarity with which the EGAI event was captured. Images are mapped to the corresponding AHRR profile in Figure 36. The first four images depict early-stage flame propagation. Ignition is captured just after the spark is introduced in Image 1 and the flame kernel grows outward in the subsequent images, extending beyond the field of view in Image 4. Note that the field of view was limited by the relative size of the windows to the size of the combustion chamber. By the time the flame reached the field of view boundary, it encompassed a mere 7% of the total chamber volume. Beyond this point, growth of cellular instabilities on the outer surface of the flame provide evidence for continued propagation between 2.0 and 4.5 ms. Then, a low magnitude spike in AHRR is detected and shortly after a secondary, more turbulent flame appears in the field of view on the left-hand side (image 5). This secondary flame may be acting in conjunction with a LTHR event, as the AHRR decreases momentarily before the EGAI peak. Shortly thereafter, in Image 6, a sudden vivid change in the view port suggests autoignition. The cellular instabilities that were used to identify the flame front disappear, replaced by what looks to be a more uniform, homogenous gas that directly corresponds to the primary EGAI peak in the AHRR graph. Images 7 and 8 were taken after peak AHRR.

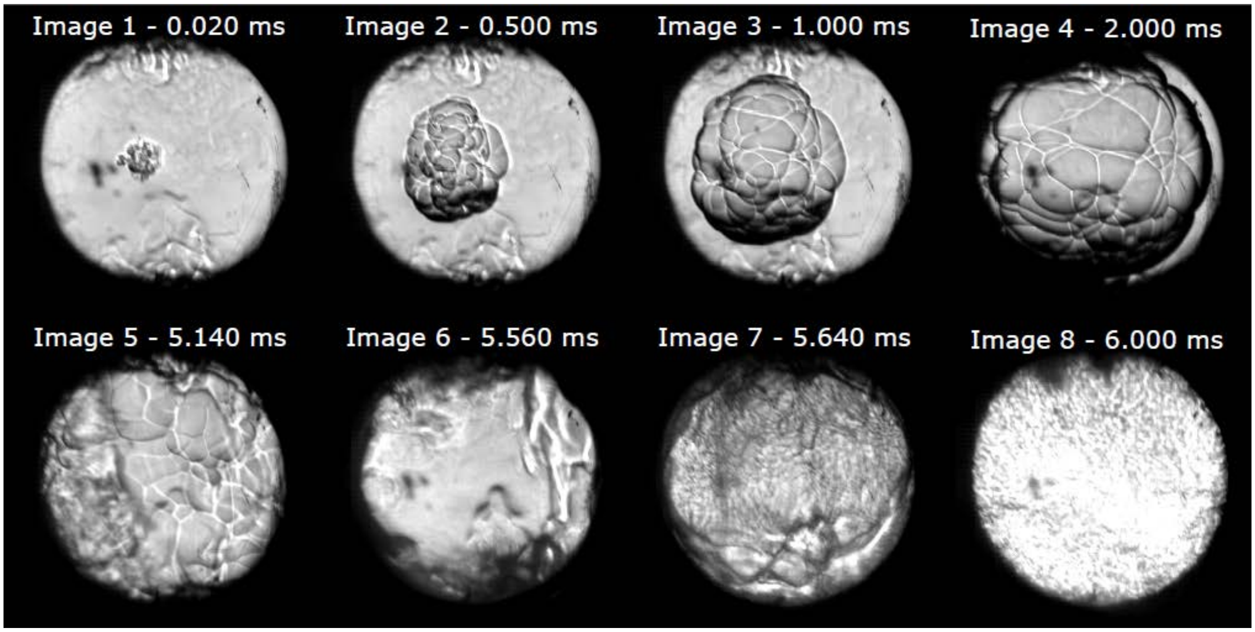

Figure 35. Schlieren images captured at 50,000 frames per second for a PRF 90, index 4 experiment. Image numbers correspond with the labels on the AHRR profile shown in Figure 36. The time listed for each image is relative to the ignition timing.

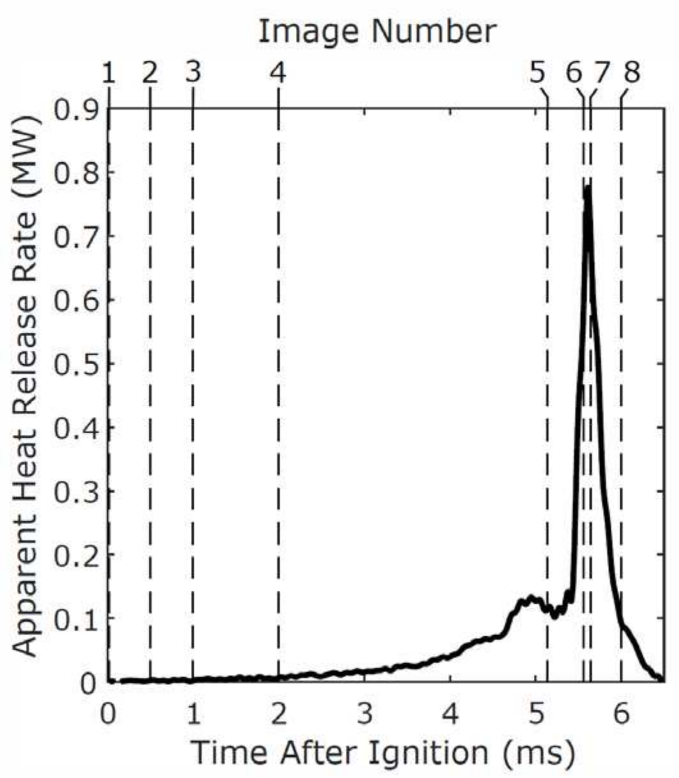

Figure 36. AHRR profile for the PRF 90, index 4 experiment featured in the Schlieren images of Figure 35. Vertical dashed lines indicate the times at which those images were taken.

Low-temperature volumetric heat release (LTHR) was clearly identified through direct optical observation and AHRR peak identification. As the low-temperature reactions are taking place, the diffraction characteristics of the end-gas are affected by the production of combustion radical species. Optically, such events manifest themselves as distortions of the field of view and a sudden darkening or lightening of the image without obstruction of the flame surface. This effect is difficult to present in still image form, and is not distinguishable in the images of Figure 35.

The transition to EGAI has also been observed while the outer perimeter of the propagating flame is still in view. Figure 37 features Schlieren images from a PRF 50 trial with the initial conditions of index 1 in which the transition to volumetric heat release is captured completely. These images are mapped to their corresponding AHRR measurements in Figure 38.

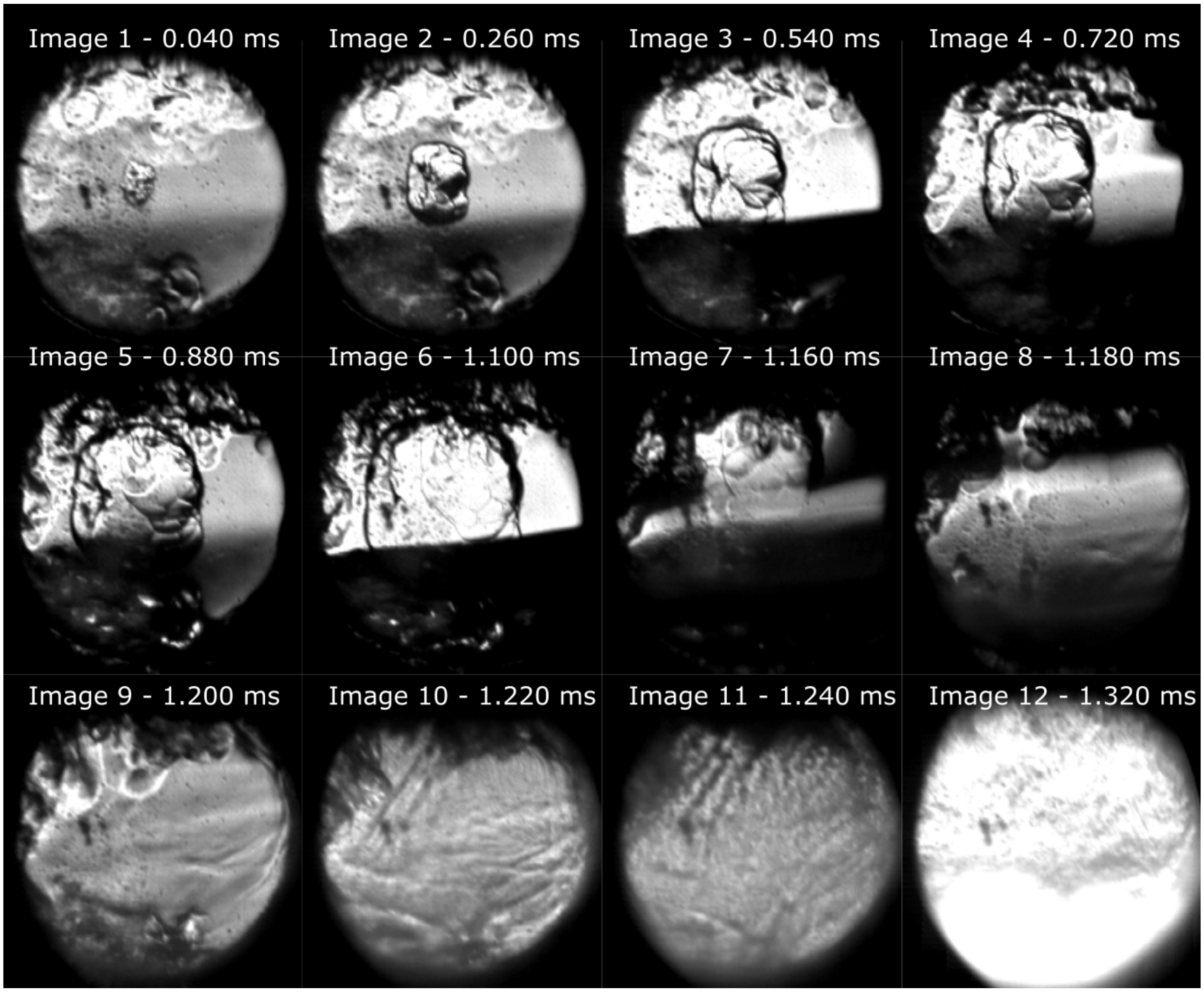

Figure 37. Select Schlieren images from the eighth trial conducted with a PRF 50 fuel blend with the initial conditions listed under index 1 in Table 3. Images are mapped to their corresponding AHRR measurements in Figure 38.

The first two images of the presented sequence depict the propagating flame shortly after ignition. LTC is detected by the AHRR measurements of images 3-5 and manifests as the lightening and darkening of the images in the sequence. This effect is depicted with more clarity than in the previous example. The propagating flame is completely engulfed by high-temperature volumetric combustion in image 7, corresponding with the massive gain in AHRR that indicates EGAI. Only a small portion of the light from the LED is able to penetrate the medium. This is either because the gases at this stage are opaque or the refractive index of the combustion radical species is sufficiently high that the majority of the light becomes blocked by the knife edge. The apparent opaqueness subsides in images 9-11, corresponding with peak AHRR. As AHRR drops to zero after EGAI, the image brightens significantly, suggesting that light is being produced by the combustion event itself rather than by the LED alone. This observation was made across the board for all experiments in which EGAI occurred.

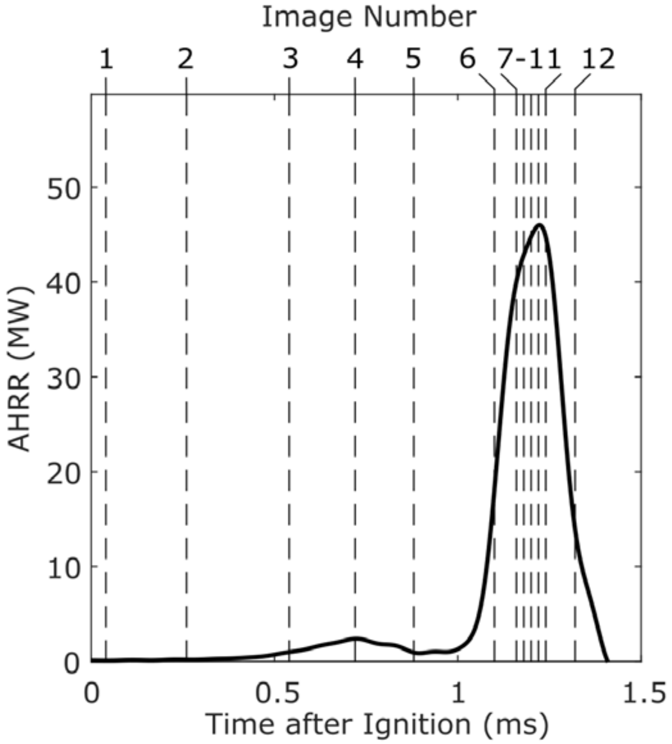

Figure 38. AHRR measurements for the PRF 50 case pictured in Figure 37. The times at which the images were taken are indicated by the dashed vertical lines and image numbers listed.

The bottom halves of images 1-8 in this example are obscured for unknown reasons. The sharp cut off suggests that light is completely blocked by the knife edge, which, as described in §2.3, is a critical component of the Schlieren technique. Interestingly, the bottom half of the images before spark ignition and after EGAI are not obscured. This may imply that volumetric combustion chemistry is already occurring in images 1-8, leading to the production of species that diffract the light to a high enough degree that it ends up being completely blocked by knife edge – a hypothesis that is corroborated by the fact that the bottom half of the image fades to black just before the spark is introduced. The other experiments performed in the same time frame did not have obscured images such as these.

Though cases in which the propagating flame is still in view when autoignition occurs are exciting, it is argued that they do not reveal much about the interaction between the propagating flame and the end-gas chemistry as they may imply to. If a perfectly spherical flame is assumed, the relative volume of the flame to the total chamber is only 7% by the time the flame reaches the field of view limitation. As such, volumetric combustion events are likely not triggered by the compressive action of the propagating flames. These experiments may resemble spark-assisted HCCI operation or they may simply be classified as preignition with a well-timed spark. The latter, in this case, is likely more accurate, as LTC appears to be active prior to the spark. Preignition occurred in many other experiments (mostly PRF 60 under index 1), but the resulting volumetric combustion would usually consume the entirety of the mixture prior to the introduction of the spark. Regardless of the scientific value of this particular case, capturing the full transition from propagating flame to EGAI is exciting and worth presenting.

5.5 RCM Combustion Abnormalities

The ability to identify combustion phenomena by their AHRR signatures is highly dependent on the repeatability, detectability, and uniqueness of those signatures. Two possible modes of combustion have been identified through experimental observations and simulation efforts that may impede that ability. The first is a mysterious jet of gas that consistently appears in experiments of relatively low propensity for autoignition. The jet disrupts the flow field on the right hand side of the images (the top of the chamber) and frequently produces what looks to be a secondary turbulent flame front on the left hand side (the bottom of the chamber). The second combustion abnormality is the potential for ignition of the gases in the crevice volumes. Because of the narrow channels that connect these crevice regions to the main chamber and their lower relative temperature, it is thought that if crevice volume combustion is occurring, EGAI events do not consume those crevice volume gases directly, but source them with high-temperatures jets that produce a second-stage of combustion. This “jet-ignition” phenomenon has been well documented [28]. Both of these abnormalities compromise the ability to properly identify combustion phenomena because of the similarity of their AHRR signatures with the other combustion modes that are of interest (e.g. EGAI, LTHR). These combustion abnormalities are discussed in detail in this section, inclusive of the determination of whether or not they actually exist, how significant the challenges they pose, and the ways by which their presence could be mitigated or at least accounted for.

Figure 39 presents a sequence of images for a PRF 90, index 3 experiment in which the gas jet disturbance is clearly captured. Note that this is the same experiment that is presented in Figure 35. The jet disturbance and the secondary turbulent flame front that subsides are highlighted by blue and orange coloring to assist identification. These combustion phenomena are easily identifiable in video format but are more difficult to distinguish in still image format. The first image shows the propagating flame shortly after ignition, while the second skips ahead to a time when the flame perimeter is well outside the field of view. The cellular texture of the flame surface can still be identified and the flame’s unimpeded motion is evidenced by the continuing growth of those cells (i.e. the flame has not yet reached the chamber wall). In image 3, the gas jet appears on the right hand side of the image, directed into the center of the chamber in the subsequent two images. Note that the images are oriented such that the pistons are just out of view to the top and bottom, and the gas jet is coming from the top of the chamber shooting downward. Shortly thereafter, in image 7, a secondary, seemingly turbulent flame front appears and propagates from the bottom of the chamber upward. The transition to EGAI obscures the view of both flame fronts in images 12-16.

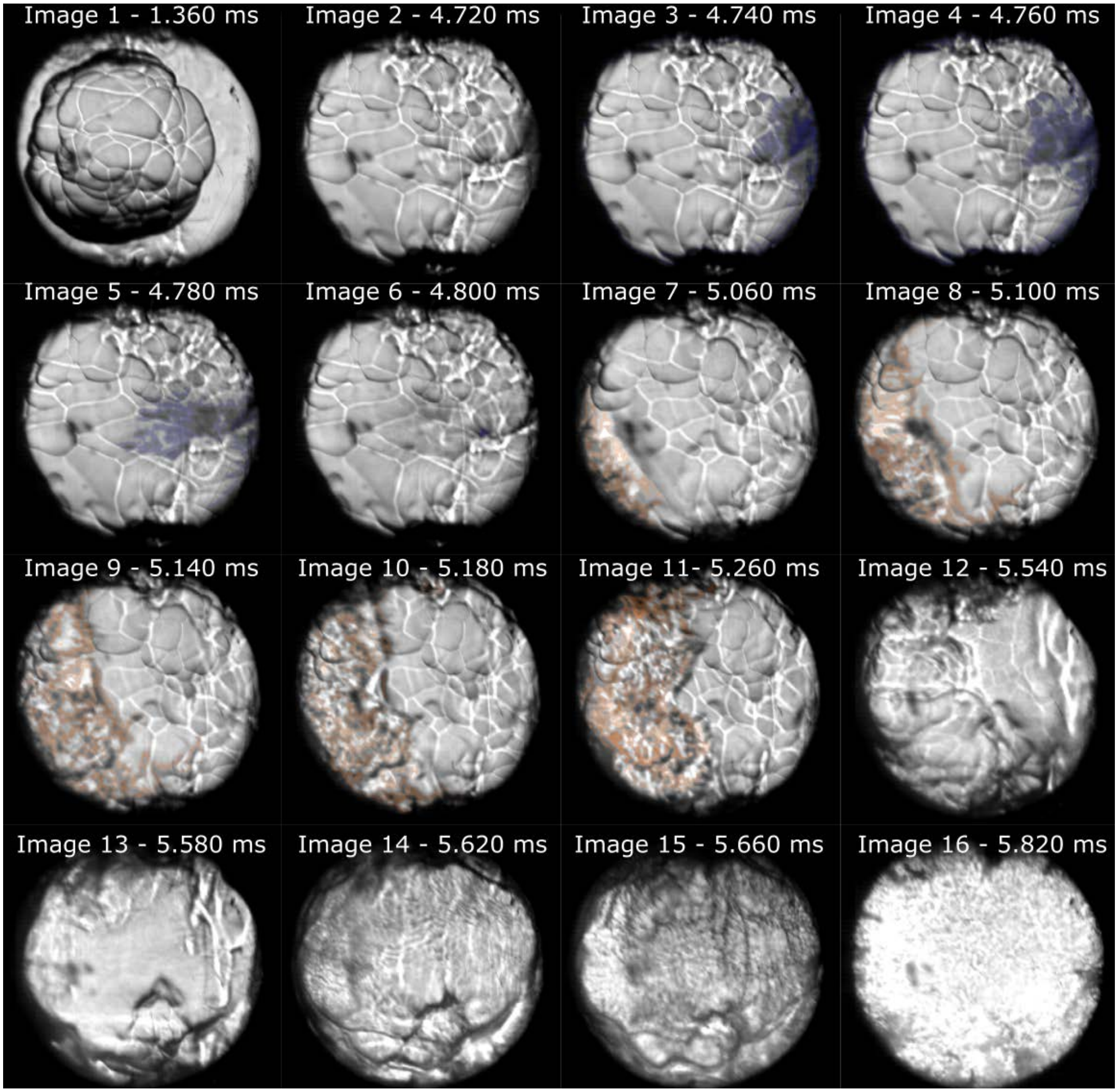

Figure 39. Schlieren images of a PRF 90 trial with initial conditions listed under index 3. The gas jet disturbance is seen on the right hand side of images 3-5, and is lightly colored blue to aid identification. The secondary turbulent flame front is depicted in images 8-11 and is colored orange. Images are mapped to their corresponding AHRR measurements in Figure 40.

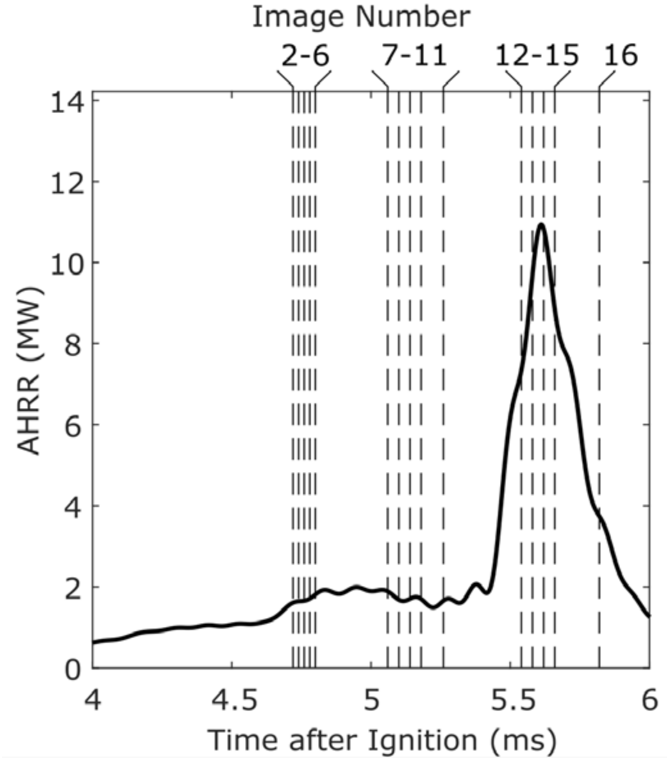

Figure 40. AHRR measurements corresponding with images presented in Figure 39.

The gas jet abnormality is observed in nearly all of the low EGAI propensity experiments. The jet always comes from the right hand side and is visually similar to the roll up vortices that are observed during compression. That similarity suggests that the jet is non-reactive. The secondary turbulent flame appears in about half of the experiments in which the gas jet disturbance is observed. If present, it is always initiated just outside the field of view to the left of the image. This behavior is considered abnormal as it is a deviation from the designed experiment. The most simplified, controlled combustion event is the one in which the symmetry condition is preserved. The introduction of a gas jet disturbance and unintended secondary flame front affects the interaction between the main propagating flame and the volumetric combustion events, which is undesirable for a controlled study.

More critically, these abnormalities manifest as similar AHRR signatures to volumetric LTC events, interfering with the proper identification of the main combustion modes. Figure 40 presents the AHRR profile for the presented images. The times at which the images were taken are denoted by the dashed vertical lines and listed image numbers. Images 2-6, in which the gas-jet is clearly captured, correspond with a local bump on the AHRR plot. That bump is associated with LTHR in other experiments, but no optical evidence of LTHR in this trial exists (i.e. there is no image distortion or lightening/darkening effect). The subsequent images in which the secondary turbulent flame is captured (images 7-11) are time mapped with AHRR measurements that momentarily decrease prior to EGAI.

Though the images may suggest the opposite, it is likely that the momentary low-magnitude increase in AHRR is caused by the secondary flame front, rather than the gas jet. The turbulent flame is initiated off-screen, meaning that it is already releasing energy and raising chamber pressure before it is optically identified. The reason for why AHRR decreases after the local peak is unknown – AHRR should continue to rise up until the point of EGAI unless the flame is impeded. An alternative, perhaps more likely, explanation of the local AHRR bump is that the gas jet reflects off the chamber's pressure transducer (which it is oriented towards), thus causing a momentary increase in the rate of pressure rise.

The fact that these abnormalities are repeatable implies that they are caused by some element of the RCM combustion chamber, rather than by random spatial gradients. Given the consistency of the gas jet origin and its proximity to the top of the chamber, it is likely that it is somehow the result of the dead volume within the chamber's fill valve. Illustrated in Figure 41, tested gases are introduced to the RCM chamber via a ball valve on the top side. The valve handle turns a hollow cylinder that is ported to either connect or close off the gas manifold to the chamber volume according to its position. The flaw with this design is that the valve contains approximately 1.5 cm^3 of dead volume that is continuous with the main chamber even when the valve is in the closed position, creating a condition of axial asymmetry for the combustion chamber. This dead volume in the fill valve is depicted in Figure 41 by the dash outlined box.

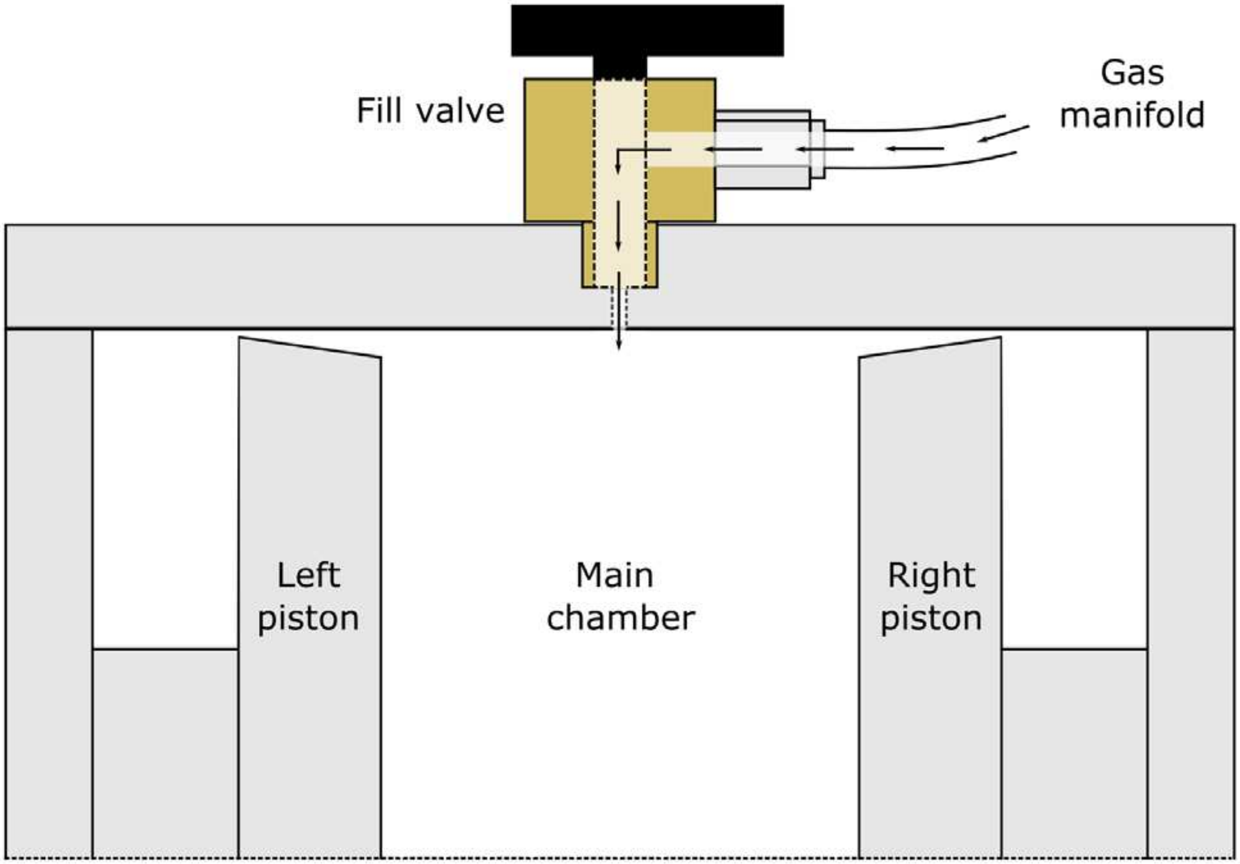

Figure 41. Cross-section illustration of the RCM combustion chamber to show the dead volume within the fill port valve. The dash outline on the fill port gives an indication for the size of the volume that is still connected to the main combustion chamber when the valve is closed. Not drawn to scale.

The mechanics by which this dead volume could produce a gas jet prior to EGAI events are unclear. The gas jet always appears while the flame is still propagating, meaning that the end-gases are being compressed and the pressure differential between the fill valve and the main chamber should be such that gases are flowing into that dead volume rather than out of it. Local autoignition in the fill port would reverse the pressure differential, causing such a jet. However, the gases within the fill valve are thought to be at a lower temperature than the rest of the end-gases due to the increased surface area to volume ratio in that region (i.e. there is more heat transfer). NTC behavior could explain the autoignition of the fill port dead volume before the rest of the chamber, though the consistency by which and the thermodynamic condition range over which the gas jet is observed suggests that this is unlikely. Further, should autoignition be occurring in the cooler regions before the rest of the chamber, the gases within the crevice volumes would also likely autoignite before the main chamber, given that they are also subject to higher heat transfer rates. The crevice volumes contain much more unburned gas than does the fill port valve. The resulting autoignition event within the crevice volume is suspected to cause a much higher magnitude spike in AHRR than what is detected at the time corresponding to the initiation of the gas jet. Further still, if the jet were caused by autoignition within the fill valve, the temperatures of the gases within the jet would be extremely high. If this were the case, the jet would immediately initiate secondary flame fronts in the end gas directly adjacent to the valve, which has never been observed.

Adding to the abnormality, the secondary turbulent flame front, if present, always appears after the gas jet and from the opposite side of the chamber. The consistency of the relative timing and spatial positioning between the two events implies causation, though the mechanics by which the gas jet could trigger the secondary flame front are unclear also. The reason why the jet would ignite a flame at the bottom of the chamber rather than at the top of the chamber near its origin is elusive. Fundamentally, the cause of the gas jet is unknown, as is that of the secondary flame front, and the association of the two events is merely speculative.

Means to mitigate this abnormality have been sought out. A stem gasket fill valve was implemented to eliminate the valve's dead volume, but leakage and gasket failure were significant problems and that valve type was abandoned. A spacer plug was fit to the interior of the ball valve to reduce the dead volume size. The plug seemed to reduce the size of the jet, though it did not eliminate it entirely and the compression ratio was changed from 11.6:1 to 11.8:1. All that said, though the gas jet and secondary turbulent flame disrupt symmetry, they are not thought to invalidate the experiment. Confidence in the identification of LTHR events is compromised, but the overall quantification of the magnitude of the EGAI events (f_{EGAI}) are unaffected.

The possibility of crevice volume combustion is not as benign. Crevice volume combustion is characterized by the initiation of propagating flames in the regions behind the front face of the pistons. Volumetric autoignition could also occur in the crevice volume, before, after, or simultaneously with the autoignition of the main chamber. This is a problem because, if it is occurring in the experiments, crevice volume combustion results in AHRR signatures that are indistinguishable from those of EGAI events. Thus, a propagating flame entering the crevice volume would be identified as EGAI, and the f_{EGAI} metric would misrepresent the amount of energy released by volumetric combustion events in the main chamber.

To fully assess the possibility of crevice volume combustion and its implications on the interpretation of the collected data, the several modes by which it can substantiate must first be addressed. CFD simulations have aided in the identification of four primary combustion mode progressions in the laser-ignited RCM experiments: (1) the spark-ignited flame propagates completely to the wall, no autoignition occurs, and the flame quenches at the channel connecting the main chamber to the crevice volume; (2) the flame propagates completely to the wall with no autoignition but is not quenched and continues through the channel to consume the crevice volume; (3) LTHR and/or EGAI occurs in the main chamber before the flame reaches the wall, quenching occurs at the crevice volume channel, and no combustion in the crevice volume ensues; (4) LTHR and/or EGAI occurs in the main chamber, combustion is extinguished at the channel, but then reinitiated in the crevice volumes by the high temperature product gases of the autoignition event.

These progressions are illustrated graphically in Figure 42, along with the AHRR signatures that would result.

The AHRR signatures are illustrations informed by behavior observed in either the simulations or the experiments. They do not represent real measurements, and should not suggest that these types of combustion are anything more than theoretical. Instead, they are only used to help qualitatively identify characteristic AHRR behavior of specific combustion behavior. Combustion mode (1), in which there is no EGAI or crevice volume combustion, features a steady ramp up in AHRR with no inflection point. This behavior has been observed experimentally, meaning that there are indeed experiments in the data set in which the crevice volumes do not ignite. Combustion mode (2), in which no EGAI occurs but a propagating flame enters the crevice volume, features a strong AHRR inflection point leading to an obvious peak. By the time the propagating flame enters the channel, the unburned end-gases in the crevice volume can make up as much as 50% of the total trapped mass (see Figure 54 of §6.2). As those more dense gases begin to burn, the rate at which energy is being released increases substantially leading to the observed AHRR peak. Combustion mode (3), in which EGAI occurs but the crevice volumes do not ignite, features a similar AHRR signature to that of combustion mode (2). Here, the primary AHRR peak is due to the rapid heat release from the volumetric combustion event in the end-gas. Combustion mode (4), in which both EGAI and crevice volume combustion occur, features sequential AHRR peaks for both events.

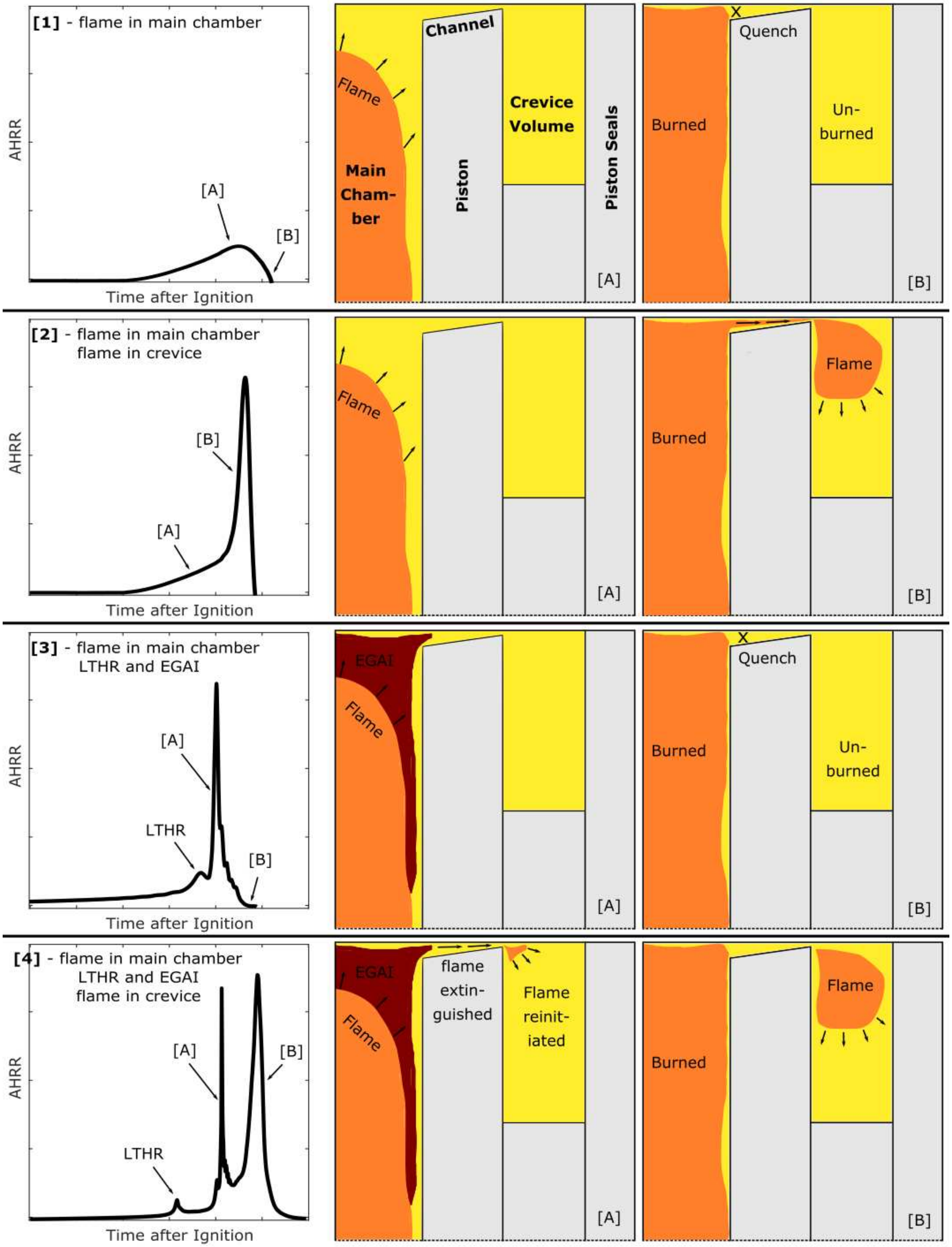
[1] - flame in main chamber
AHRR
Time after Ignition
[A]
[B]
Channel
Flame
Main Chamber
Piston
Crevice Volume
Piston Seals
[A]
Burned
Quench
X
Un-burned
[B]
[2] - flame in main chamber
flame in crevice
AHRR
Time after Ignition
[A]
[B]
Flame
[A]
Burned
Flame
[B]
[3] - flame in main chamber
LTHR and EGAI
AHRR
Time after Ignition
[A]
LTHR
[B]
EGAI
Flame
[A]
Burned
X
Quench
Un-burned
[B]
[4] - flame in main chamber
LTHR and EGAI
flame in crevice
AHRR
Time after Ignition
[A]
[B]
LTHR
EGAI
Flame
flame extin-guished
Flame reinit-iated
[A]
Burned
Flame
[B]

Figure 42. (Page 93) Illustrations of SI combustion progression modes of interest in the RCM shown with their would-be characteristic AHRR signatures. Modes are delimited by row and feature two illustrations each – [A] and [B]. The characteristic AHRR peaks associated with the illustrated combustion modes are indicated on the AHRR profiles in the left column.

Other options exist, but are of less interest: (5) crevice volumes could autoignite simultaneously with the rest of the chamber, but it would be a non-issue as crevice volume autoignition would then be correctly identified as EGAI and counted towards f_{EGAI}; (6) a second flame-to-EGAI progression could occur in the crevice volume (i.e. a premixed flame begins to propagate in the crevice volume compressing the crevice volume end-gas and potentially leading to a second autoignition); (7) preignition results in volumetric combustion of the entire chamber prior to the spark. The latter was observed frequently, but flagged as unsuccessful laser-ignited experiments.

The challenge that arises if crevice volume combustion is occurring is that reliably distinguishing between the AHRR signatures of combustion modes (2) and (3) is not possible. Given that EGAI does not occur in combustion mode (2) but it does in mode (3), the inability to distinguish them by their AHRR signatures is a fundamental flaw to the experiment. Further, if progression mode (4) is occurring, the AHRR signature is not able to be sufficiently resolved for identification amongst the heavy pressure oscillations that result from EGAI. In essence, the entire structure of identifying combustion phenomena by AHRR signature hangs on whether crevice volume combustion is occurring. There is no way of observing the crevice volumes optically with the current combustion chamber, so the question of crevice volume combustion must be addressed through larger trends in the AHRR datasets and qualitative comparison with simulation results. This section covers the former, while the latter is described in §6.1 and §6.2.

Assessment of the trends in relative combustion efficiency for the entire data set seem to suggest that no crevice combustion is occurring. The true combustion efficiency cannot be evaluated through integration of the AHRR curve. The AHRR is subject to heat transfer, and as such, longer combustion durations will result in lower integrated AHRR values. This means that even if combustion efficiency is 100% in all cases, there will still be a trend between the integrated AHRR and the combustion duration. Further, data filtering affects the magnitude of the derived AHRR and comprises the accuracy of the integrated AHRR as an indicator of the amount of energy released during combustion. Nevertheless, integrated AHRR is still a valuable metric as indication of the apparent combustion efficiency relative to other cases. Apparent combustion efficiency serves as a comparison between an experiment's integrated AHRR and its estimated charge energy that is found with the known chamber volume, initial pressure, stoichiometry, and approximate heating value of the fuel. Apparent combustion efficiency is plotted against f_{EGAI} for the all experiments in Figure 43 alongside a representation of the expected trends for a dataset in which the onset of crevice volume combustion is captured.

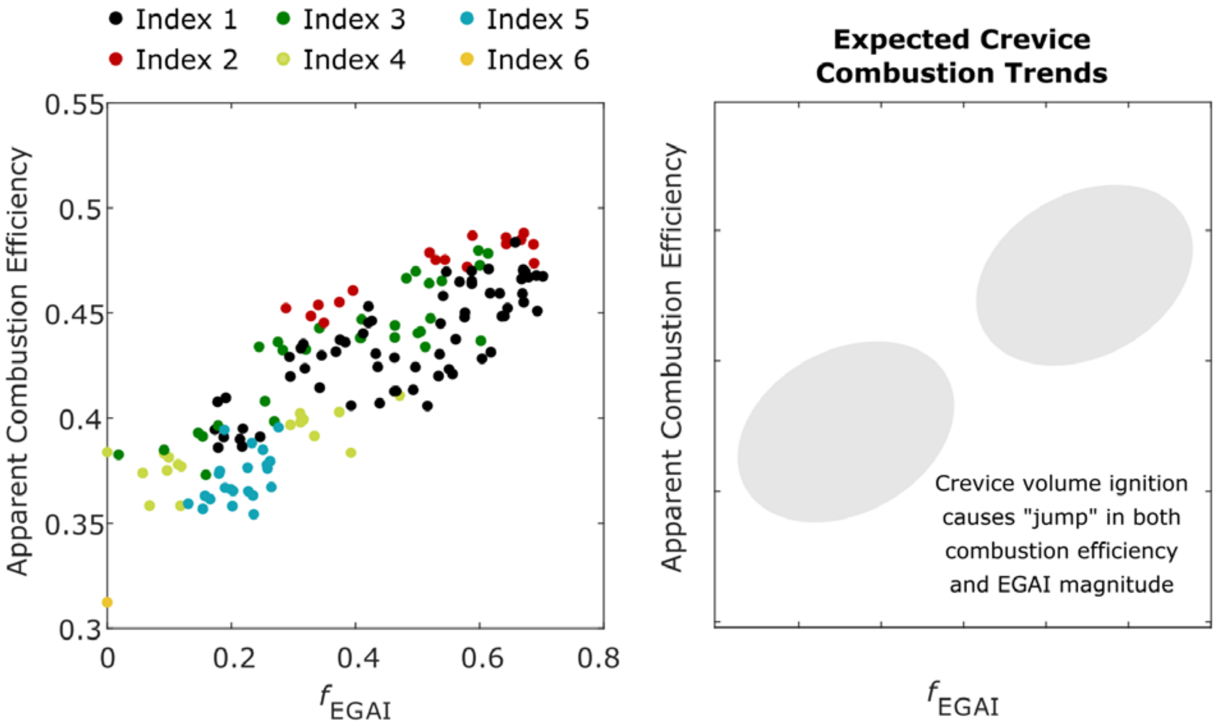

Figure 43. Apparent combustion efficiency plotted against EGAI magnitude. The measured data from the experiments is presented in the left plot and colored by initial condition index of Table 3.

The plot on the right is an illustration of the theorized trends that would result if the onset of crevice volume combustion were captured in the data set.

A strong trend between integrated AHRR and f_{EGAI} exists. This trend is expected as cases with higher f_{EGAI} tend to have shorter combustion durations so heat transfer has less of an effect. The trend could also be explained by increasing combustion efficiency with more aggressive EGAI events. Two trials in this dataset were evaluated with f_{EGAI} of 0. With the method of qualitatively identifying characteristic AHRR signatures, this means that the AHRR profile featured no inflection point or primary peak (see combustion mode (1) in Figure 42). Based on the prediction of how crevice volume combustion manifests on the AHRR plot (see combustion mode (2) in Figure 42), it can be concluded that there is no crevice volume combustion in these two particular experiments.

With the $f_{EGAI} = 0$ cases as the starting point, the trend of the larger data set can be interpreted. In all other cases, an AHRR peak similar to that of combustion mode (2) or (3) was detected, causing the f_{EGAI} measurements to be evaluated as non-zero. Schlieren videos confirm the presence of EGAI in most of these cases. The detected AHRR peak may also be caused by combustion behavior analogous to mode (4), but the necessary filtering of the pressure curve may not be able to resolve the two AHRR peaks. A clear indication of combustion in the crevice volumes would be a discontinuous increase in relative combustion efficiency (i.e. integrated AHRR). That is, combustion efficiency would be substantially higher for the cases in which the crevice volumes ignited compared to those in which they did not. Should the additional heat release from combustion in the crevice volumes be identified as EGAI, then a discontinuous increase in f_{EGAI} would also result. If crevice volume combustion is a binary matter (i.e. it either happens or it does not), then having experiments in which crevice volume combustion occurred and did not occur in the same data set would be indicated by two distinct groupings in Figure 43. That is, the sharp increase in both f_{EGAI} and integrated AHRR would clearly distinguish between cases in which crevice volume combustion occurred and those in which it did not. An illustration of this proposed behavior is also given in Figure 43 to better describe the theoretical trend. The grouping of the data into a single cluster suggests that the crevice volumes do not ignite.

It is possible that crevice volume combustion is not a binary matter, however. There could exist a condition in which ignition in the crevice volume would not result in a sharp increase in combustion efficiency, and there would instead be a gradual transition from no crevice volume combustion to complete crevice volume combustion. If this is indeed what is happening in the experiments, the lack of two distinct groups in Figure 43 would be inconsequential. For further assessment, an experiment's integrated AHRR is plotted against its maximum detected AHRR for all experiments with initial conditions of index 1 in Figure 44.

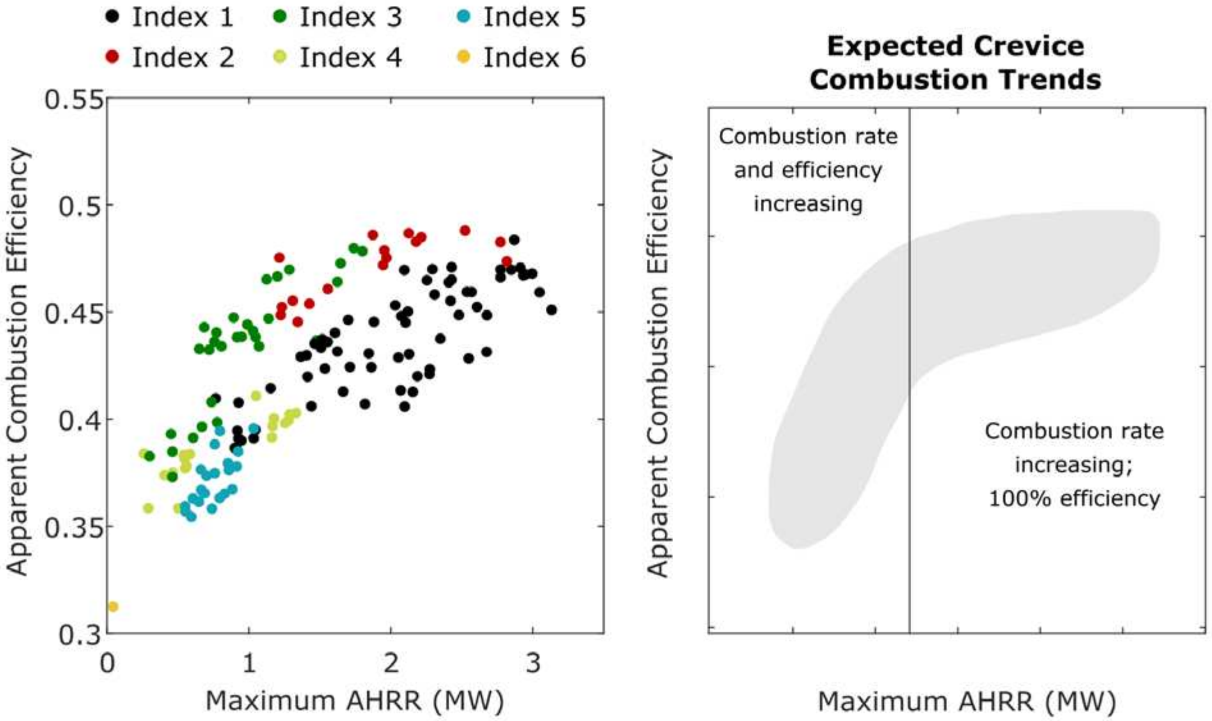

Figure 44. Maximum AHRR and apparent combustion efficiency trends in the full data set. Plot on the left features real data colored by the initial condition index, as coded in Table 3. Plot on the right is an illustration of the data trend expected if the onset of crevice volume combustion is

captured within the data. Apparent combustion efficiency derived from the integrated AHRR and the estimated charge energy for each experiment.

Maximum AHRR is affected by heat transfer, just as integrated AHRR, but to a lesser degree. Maximum AHRR is thought to be a stronger function of the amount of unburned gas that is involved in the combustion responsible for the primary AHRR peak (whether it be caused by EGAI, crevice volume combustion, or both). Should the transition to complete crevice volume combustion be gradual, then, starting with the case in which the crevice volumes are known to not ignite ($f_{EGAI} = 0$), the integrated AHRR and maximum AHRR will increase as a function of combustion efficiency (i.e. increasing levels of crevice volume combustion) and of decreasing combustion duration to some degree. Eventually, though, 100% combustion efficiency will be achieved (or some constant value of combustion efficiency). Beyond that point, the integrated AHRR and maximum AHRR will no longer be a function of combustion efficiency, as it has reached its maximum value, and will only be a function of combustion duration. Integrated AHRR is a stronger function of combustion duration than is maximum AHRR, so a change in the slope of the trend between integrated AHRR and maximum AHRR will result. Figure 44 includes an illustration of this theorized behavior. Given that there is no slope change in the trend between integrated and maximum AHRR, it is thought that combustion in the crevice volumes is not occurring in this dataset.

The question of crevice volume combustion remains open, despite the presented trends in the data that suggest it is not occurring. Substantial simulation evidence exists for the opposite conclusion, as will be discussed in §6.2. In all, the potential for crevice volume combustion to be misidentified as EGAI is not thought to invalidate the experiment. There is no question that EGAI has been directly observed, quantified, and correlated with thermodynamic and fuel reactivity conditions in this study. Instead, the potential for crevice volume combustion speaks to flaws in this particular combustion chamber design for the application of laser-ignited RCM experiments. Alternative chamber designs will be discussed in §6.3.

CHAPTER 6 – COMPUTATIONAL RESULTS

Three-dimensional computational fluid dynamic (CFD) models were constructed for the laser-ignited RCM experiments. Symmetric compression models, as described in §4.1, compose the majority of the simulations for PRF blends. Asymmetric compression models were employed on occasion to maximize experimental/computational agreement in cases with natural gas as a fuel. Both serve to inform experimental observations, strengthen understanding of EGAI physics, and better assess combustion abnormalities. “None of the models are correct, but some of them are useful.” – Greg Hampson, Ph.D.

6.1 Symmetric Compression Models for PRF Blends

Symmetric compression models were employed as a means of further investigating the effects of changing fuel reactivity and thermodynamic condition on EGAI propensity in the laser-ignited RCM experiments. The final model is the result of six complete redesigns along with countless iterative modifications to the domain and to the model execution strategies. Presented here are the final six simulations that were performed using this model. Two temperature conditions after TDC were explored. The first with an integrated temperature value of 5.88 Ks and the second with 6.42 Ks. Given the symmetrical compression condition imposed by limitations of the model, both feature piston offsets of 0 ms. All of the simulations were performed with the fuel and oxidizer blends in stoichiometric proportion, with initial conditions corresponding to those of experimental initial condition index 1. The 5.88 Ks models were initiated at a starting temperature of 300 K, while the 6.42 Ks models with 328 K. Three fuel reactivities were tested under each temperature condition - PRF 50, 80, and 100. Doing so resulted in the full range of heavy, medium, and light EGAI. In a similar manner to the experimental approach, fuel reactivity and thermodynamic condition are investigated independently. In accordance with experimental findings, a forced quench condition is applied at the channel inlets to the crevice volumes such that combustion does not occur outside of the main chamber (the potential for crevice volume combustion will be assessed in §6.2). The AHRR profiles of the PRF 50, 80, and 100 cases modeled under the 5.88 Ks and 6.42 Ks test conditions are shown in Figure 45.

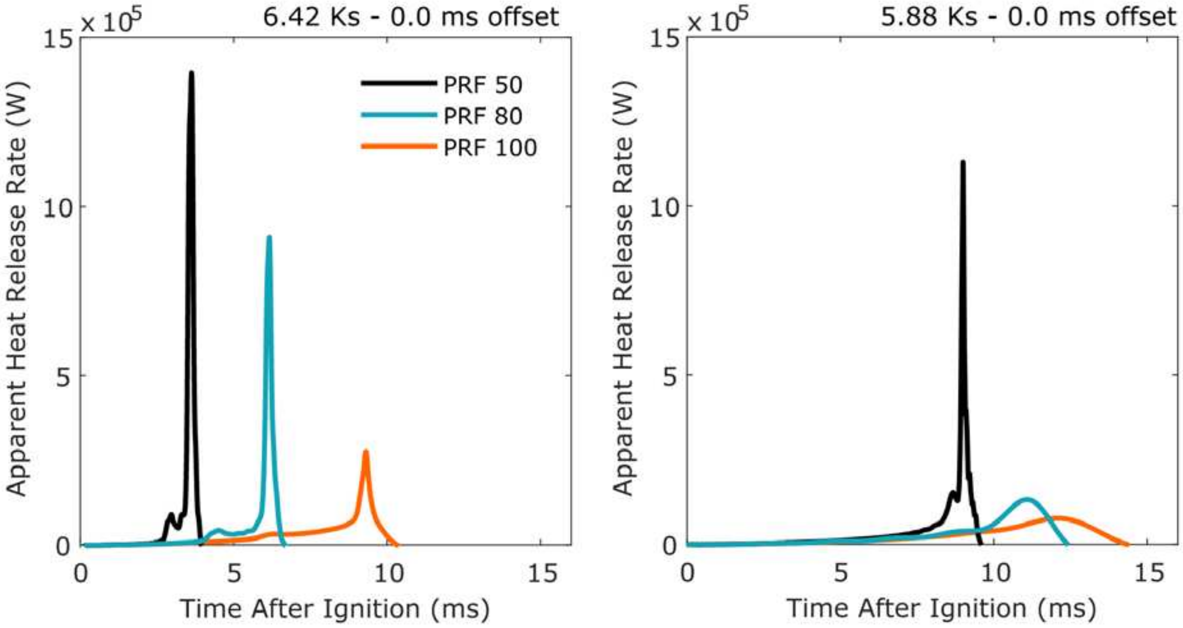

Figure 45. Simulated AHRR signatures for PRF 50, 80, and 100 under the 5.88 Ks and 6.42 Ks temperature history conditions.

Just as with the experiments, the magnitude of the maximum AHRR varied monotonically with fuel blend reactivity and integrated temperature. For both temperature conditions, the lower reactivity (PRF100) blends produce a longer combustion duration with lower rate of increase in AHRR compared to the more reactive blends (PRF50 and PRF 80). The AHRR signatures for the simulations of the 6.42 Ks test condition exhibit dramatic changes in slope, which occur after some period of moderate, longer duration AHRR rates – a clear indication of the propagating flame to

EGAI transition. This also occurs in the PRF 50 simulation of the 5.88 Ks condition, but is absent in the models of the PRF 80 and 100 blends.

Also interesting is the tighter relative grouping of the AHRR signatures under the 5.88 Ks test condition. This speaks to the decreased role EGAI has in the combustion progression at these lower temperatures and to propagation rate's lack of sensitivity to octane number. Here, the PRF 80 and 100 cases feature nearly identical AHRR signatures in the first 10 ms after ignition, but PRF 80 deviates from PRF 100 with a faster rate of combustion towards the end of the HR that is suggestive of a volumetric combustion event. Indeed, spatial maps of volumetric HRR reveal that, at the time of its deviation from the PRF 100 AHRR signature, the PRF 80 case features a flame propagating into a region in which LTHR active, as shown in Figure 46. Unlike the PRF 50 case of the same temperature condition, however, the flame of the PRF 80 case is able to consume the entirety of the end-gas prior to EGAI. Nevertheless, LTHR results in a measureable increase in AHRR that mimics the signature that would be produced by the conventional propagating flame to EGAI transition, as shown by the mapped AHRR profile of Figure 47, corresponding to the simulation images of Figure 46.

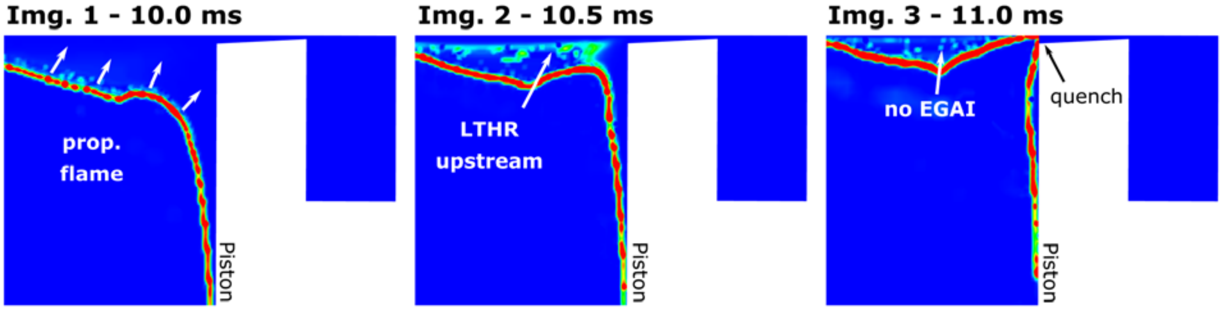

Figure 46. Volumetric HRR maps of the corner end-gases for the PRF 80, 5.88 Ks simulation. Upstream LTHR events lead to a momentary increase in measured AHRR, but the propagating flame consumes the entirety of the mixture prior to EGAI.

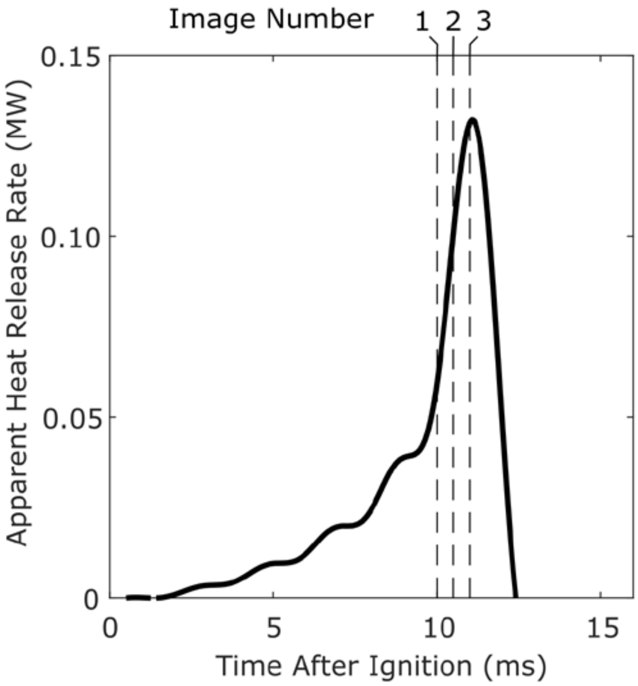

Figure 47. AHRR measurements for the PRF 80, 5.88 Ks simulation. The times at which the images of Figure 46 are taken are indicated by the dashed vertical lines.

Plotted with a lower y-axis bound, the AHRR profile of this case denotes volumetric combustion behavior, despite its absence – another potential challenge to the identification of EGAI through the AHRR signatures alone. Experimental detection of an AHRR inflection point and subsequent peak, like what is shown here for the PRF 80 simulation, would indicate EGAI and a f_{EGAI} would be derived from the peak. To maintain consistency between the experimental and computational methods, the simulated PRF 80 peak is also counted toward f_{EGAI} despite knowledge that the peak is caused by low-temperature events rather than by EGAI.

The modeled f_{EGAI} for the PRF 50, 80, and 100 cases are plotted for both temperature conditions in Figure 48. Similar trends between ON and f_{EGAI} exist in the simulations as do in the experiments. Second order polynomials seem to adequately characterize the non-linearities in the data. The same leveling-off of the f_{EGAI} measurements to a value less than 1 is present for the higher reactivities blends.

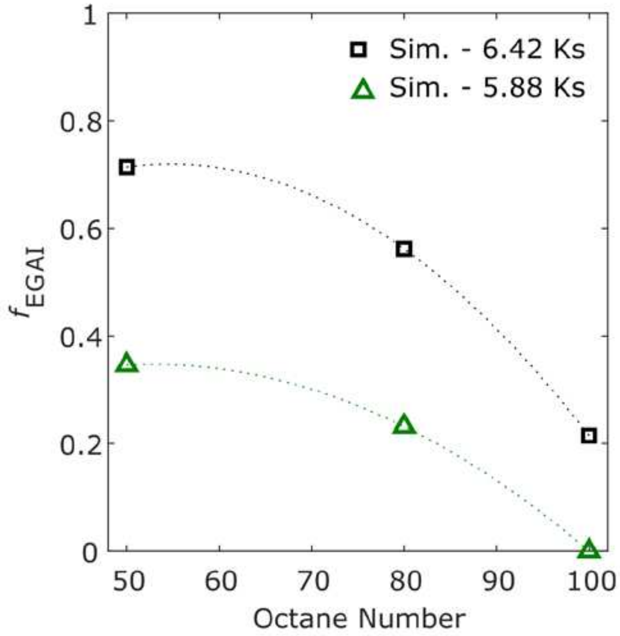

Figure 48. *F*EGAI measurements of the final six computations for the two compression temperature conditions.

To assess the validity of the model and perform a more thorough analysis of the physics behind EGAI, a representative experimental AHRR profile for the PRF50, index 4 test condition is selected for comparison purposes. It is presented along with its corresponding simulation (the PRF 50, 5.88 Ks condition) in Figure 49. The time integrated temperature values for the experiment and simulation are 6.28 and 5.88 respectively. The symmetrical compression model forces a piston offset of 0 ms in contrast to the measured piston offset of 2.189 ms in the experiment. The simulation features a forced quench condition at the crevice volume in in accordance with experimental findings.

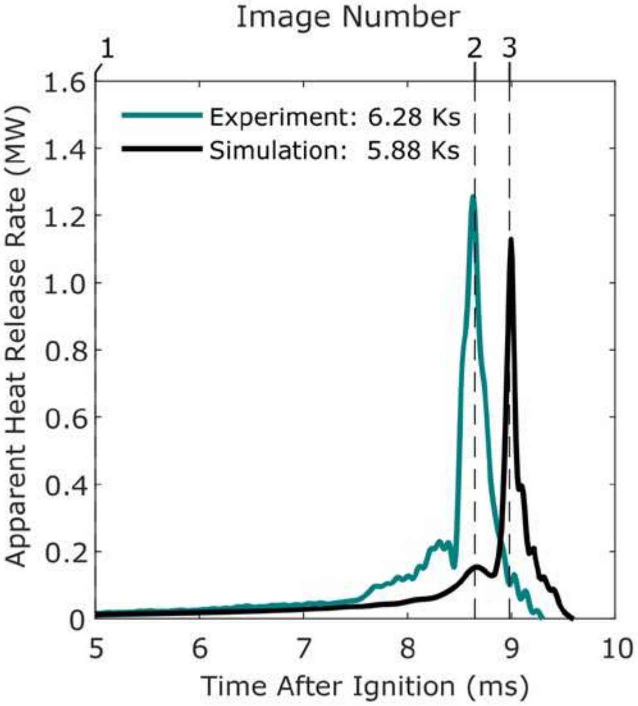

Figure 49. AHRR profiles for the experimental and simulated PRF 50, index 4 test condition. The times at which the simulation images of Figure 50 are taken are indicated by the dashed vertical lines.

Despite the simulation's cooler temperatures and lower relative turbulence level, excellent qualitative agreement between the AHRR signatures is achieved. Flame speed of the simulation was 41.9 cm/s compared to the experiment's 42.5 cm/s. The simulated and experimental f_{EGAI} measurements were 0.346 and 0.312 respectively. What is claimed here is not that the model perfectly matches the thermodynamic or fluid dynamic conditions that are present in the experiment. In fact, this is not true, given the differences in integrated temperature and piston offset between the two. The model is not predictive. Instead, what is claimed here, is that the qualitative similarity of the AHRR signatures suggests analogous combustion physics at play. With that, the combustion phenomena of the simulation can be interpreted to inform the experimental results.

The simulated volumetric heat release rate for this simulation is imaged in the central plane of the combustion chamber in Figure 50 for the three denoted times in Figure 49. These times were selected for their concurrence with the characteristic AHRR behavior used to identify propagating flames, LTHR, and EGAI events without visual data (i.e. based on the AHRR signature alone). The field of view in these frames reveals the piston cross-sectional profiles along with the crevice volumes situated on the backside of each piston face. Image 1, captured 5.00 ms after ignition, depicts a near spherical flame front that is propagating away from the central ignition site. As the flame approaches the chamber wall several milliseconds later, it triggers a short volumetric low temperature heat release in the corner end-gas that gives way to a near stagnant cool flame, revealed by the light green HRR region in Image 2. Shortly thereafter, volumetric EGAI ensues (Image 3), but leaves the propagating flame travelling parallel to the piston face undisturbed. The forced quench condition is pictured clearly in this image by the sharp cutoff of HRR at the entrance of the crevice channel.

Figure 50 also presents the combustion radical species and temperature profiles over distance for the three images. These measurements are taken along the dotted line that extends from the center of the chamber to the wall, angled such that the LTHR and EGAI events are well captured. For the three plots, the bounds of the y-axes are the same for comparison purposes, but the bounds of the x-axes change to provide sufficient resolution across the area of interest for interpretation. The extent of the x-axis for each plot is represented on the corresponding image by the bounded solid line overlay. That is, the left-most point on the x-axis is spatially indicated in the image by the bracket that is perpendicular to the measurement line and closest to center. The axis then extends in space away from center, following the solid line until reaching the second bracket, representing the right most point on the x-axis of the plot.

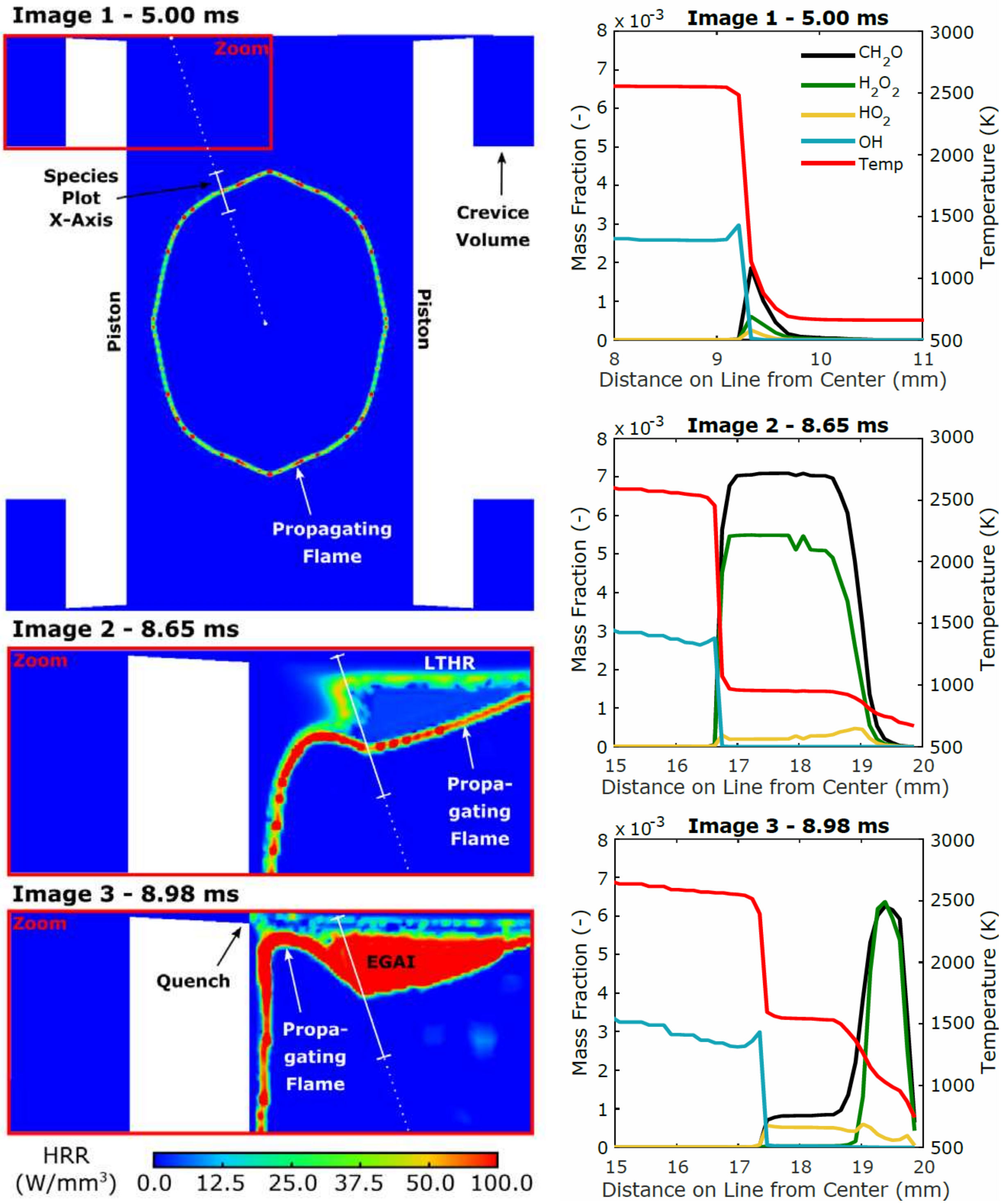

Figure 50. (Left) Central plane view of the RCM combustion chamber with pistons in the TDC position. Images colored by volumetric heat release rate to visualize combustion events. Piston cross-sections profiled in white. Images 2 and 3 feature zoomed view as indicated in Image 1. (Right) The species and temperature measurements corresponding with images 1, 2, and 3. Species and temperature measurements taken across the black dotted lines are presented in the images on

the left. The x-axes bounds of the corresponding species plots are represented by the bracketed solid line overlays in each image.

Species and temperature profiles are consistent with expectations for a thermal diffusive preheat zone in Image 1. As the flame approaches the wall and low-temperature chemistry becomes active, substantial amounts of formaldehyde (CH_2O) and hydrogen peroxide (H_2O_2) are produced, along with a modest rise in temperature (Image 2 – 8.65 ms). Both the flame surface and thermal boundary layer can be identified in the Image 2 plot by the steep drop off of radical species on either side of the end-gas volume. The volumetric formaldehyde production is indicative of low-temperature n-alkane chemistry. Hydrogen peroxide production is indicative of high-pressure hydrogen chemistry and leads to the chain branching thermal decomposition reaction $HOOH+M \rightarrow OH+OH+M$ [16]. These autoignition precursor species are more stable at medium temperatures than the reactants that formed them, and as such, temporarily slow the volumetric reactions to produce a two-stage ignition effect. Indeed, shortly thereafter, the low-temperature heat release rapidly transitions into a strong volumetric heat release that constitutes EGAI (Image 3 – 8.98 ms). During the transition to EGAI, the hydrogen peroxide mass fraction increases further and then dramatically decreases due to the thermal decomposition reaction. In this case, EGAI does not immediately break through the thermal boundary layer and the higher concentrations of formaldehyde and hydrogen peroxide remain a short while longer.

As a review of the validity of the forced quench condition imposed at the crevice volume channel inlet in the simulation, Figure 51 presents a comparison of the modeled AHRRs when the quench condition is applied and when it is not for the PRF 50, 5.88 Ks case. The two simulations are perfectly identical, save crevice combustion.

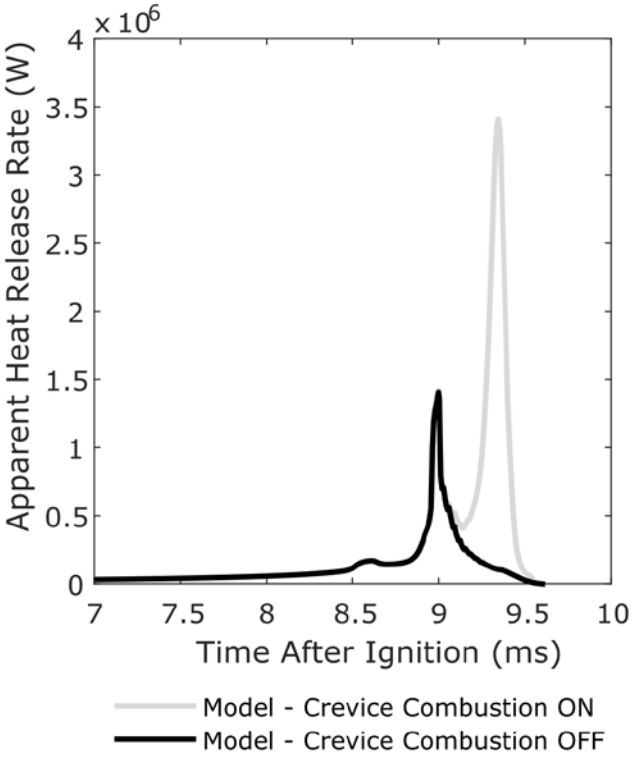

Figure 51. Comparison of the AHRR signatures of two identical simulations save crevice combustion. PRF 50, 5.88 Ks, 0.0 ms offset. In the "Crevice Combustion OFF" model, a propagating flame triggers a LTHR event followed by EGAI in the main chamber, and a forced quench condition prevents the ignition of the gases in the crevice volumes. The "Crevice Combustion ON" model does not impose the forced quench condition, resulting in a more substantial peak in AHRR that corresponds with a propagating flame consuming the compressed gases of the crevice volumes. This latter behavior has not been observed experimentally.

The case in which crevice volume combustion was allowed features a dual-peak AHRR indicator as predicted by combustion progression mode (4) of Figure 42 in §5.5. Volumetric EGAI first occurs in the main chamber, subsequently igniting the crevice volumes via a high-temperature jet. These events manifest as two separate AHRR peaks – a behavior that has never been detected experimentally. When the forced quench condition is applied, the second, higher-magnitude AHRR peak is eliminated and much better qualitative agreement with the experiment is achieved (see Figure 49). The qualitative similarity is in-itself evidence against crevice volume combustion.

However, the results of the asymmetric model for NG fuels, covered in §6.2, undermine any claims that can be made off of this comparison alone.

6.2 Asymmetric Compression Models for NG Fuels

Asymmetric compression models were used when the agreement between the model and experiment was of critical importance. To maximize agreement, individual experimental trials were selected and their compression events were meticulously modeled to best replicate TDC conditions after compression. The computational time and modeling effort expended building an asymmetric compression model are far greater than a symmetric model. For this reason, the asymmetric modeling strategy was only employed when the level of accuracy required made it absolutely necessary.

One of these cases that is of particular interest was for an auxiliary project funded by the DOE in which laser-ignited RCM experiments were used to validate the performance of an in-house reduced chemical kinetic mechanism for natural gas (NG) fuels. The mechanism proved adequate in 0D CHEMKIN simulations in which the initial conditions and pressure-time history estimated the thermodynamic conditions of the end-gas. A representative NG experiment, directly analogous to those performed with PRF blends, was selected for modeling. The mixture composition, initial conditions, and compression characteristics of the experiment are listed in Table 6 below.

The motion profiles of the two pistons were meticulously modeled using the LVDT measurements from the experiment and the third-order polynomial time-correction methods described in §4.3. This method allowed for the piston offset of the real compression event to be modeled, thereby more accurately capturing the temperature, pressure, and flow field conditions of the combustion chamber during and after compression. The resulting pressure-time history of the compression event in the simulation matched well with that which was measured for the selected trial, as shown in Figure 52.

Table 6. Gaseous composition and initial conditions of the representative NG experiment selected for modeling.

Fuel Blend Composition (mass %)	CH_4	69.3	Equivalence Ratio	(-)	1.00
	C_2H_6	23.8	Initial Temp.	(K)	308
	C_3H_8	6.9	Initial Pressure	(bar)	1.000
Inert/Oxidizer Composition (mass %)	O_2	18.7	TDC Temperature	(K)	795
	N_2	15.4			
	Ar	65.9			

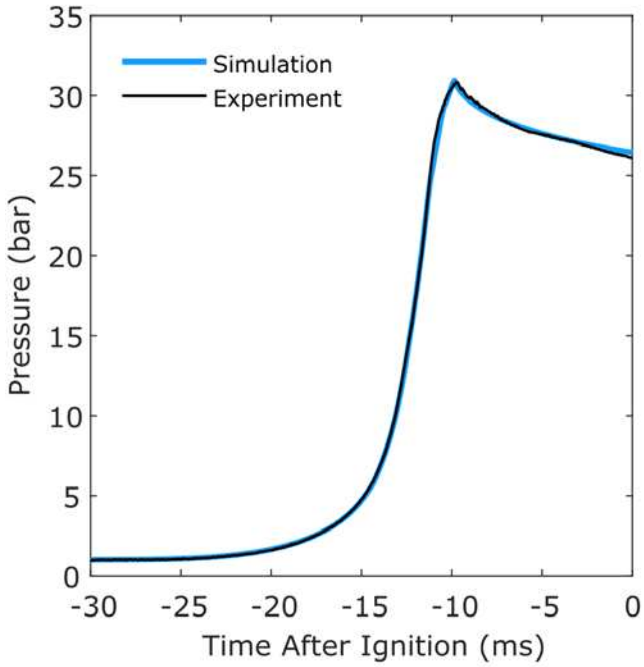

Figure 52. Simulated and experimental pressure traces for the wet gas, no EGR NG laser-ignited RCM representative experiment. Asymmetric compression modeling strategies used, resulting in excellent accuracy in the temperature and flow field conditions at TDC.

Quantitatively confirming the similarity of the compression events, the integrated temperatures of the simulation and of the experiment were 7.271 Ks and 7.274 Ks respectively. It is suspected that the flow field was modeled to a similar degree of accuracy, though no quantitative metric can be claimed. In large part due to the accuracy with which the compression event was modeled, the combustion progression and resulting AHRR measurement of the simulation was highly similar to that of the experiment, as shown in Figure 53. The predicted and observed burned flame propagation rates (not corrected for flame stretch) were 1024 cm/s and 1036 cm/s respectively. The rise in pressure due to combustion also exhibits fair agreement with the experiment, though peak pressure is not captured quite as well.

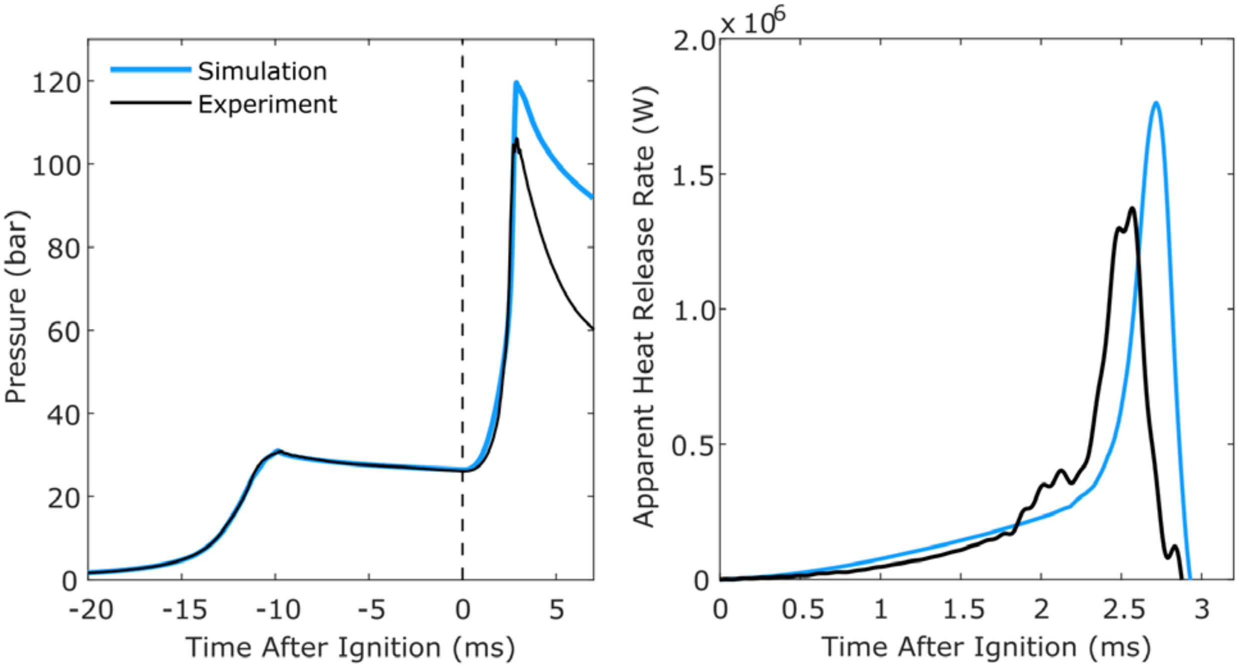

Figure 53. Pressure and AHRR profiles for laser-ignited NG experiment of the test conditions listed in Table 6. Both experimental and simulated data shown.

With that agreement comes the introduction of the most challenging problem this research has faced – the fact that despite the usual AHRR indicators, this trial features no EGAI. Instead, the AHRR inflection point and subsequent peak is caused by the propagating flame entering the crevice volume.

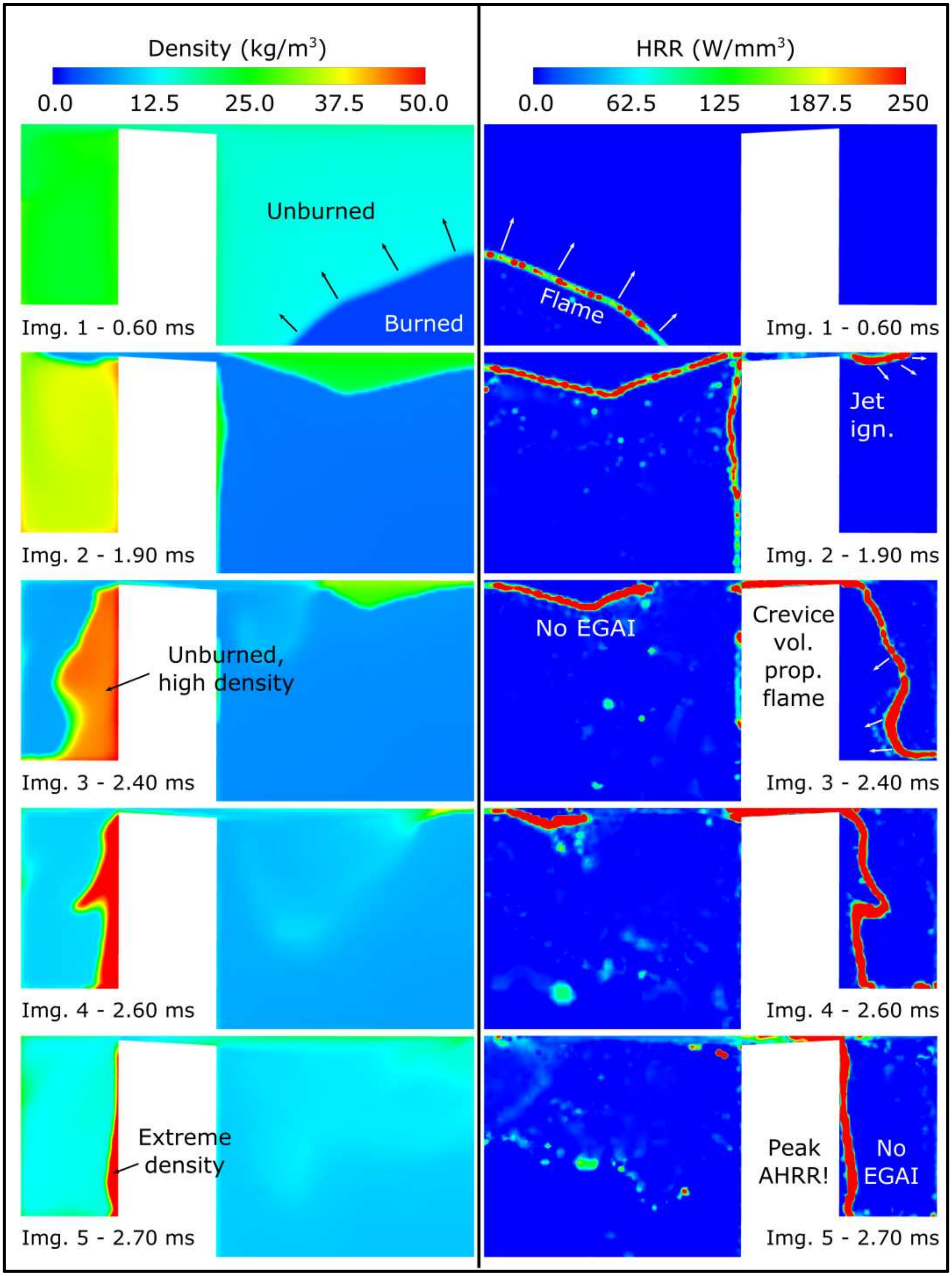
Density (kg/m³)
0.0
12.5
25.0
37.5
50.0
HRR (W/mm³)
0.0
62.5
125
187.5
250
Unburned
Burned
Flame
Img. 1 - 0.60 ms
Img. 1 - 0.60 ms
Jet
ign.
Img. 2 - 1.90 ms
Img. 2 - 1.90 ms
Unburned,
high density
No EGAI
Crevice
vol.
prop.
flame
Img. 3 - 2.40 ms
Img. 3 - 2.40 ms
Img. 4 - 2.60 ms
Img. 4 - 2.60 ms
Extreme
density
Peak
AHRR!
No
EGAI
Img. 5 - 2.70 ms
Img. 5 - 2.70 ms

Figure 54. (Page 113) Images of the laser-ignited NG simulation colored by density in the left column and by volumetric heat release rate in the right. The image corresponding AHRR measurements are presented in Figure 55.

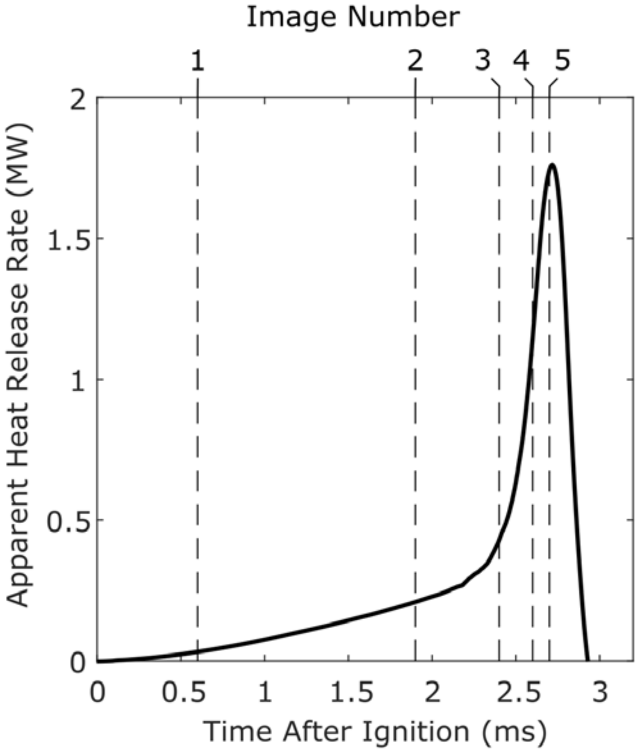

Figure 55. Simulated AHRR profile for the laser-ignited NG case. The times at which the images of Figure 54 were taken are represented by the dashed vertical lines.

This combustion progression mode was discussed at length in §5.5, but this simulation is what gives it validity. Figure 54 shows a sequence of density and HRR maps from the simulation that show the flame propagating through the crevice volume unobstructed. The observed increase in heat release rate at the time of image 3 is the result of the unburned gas density in the crevice volume region being much higher than that of the main chamber. Upstream unburned gases are compressed by the approaching flame, and by the time the propagating flame enters the channel, over half of the chamber's trapped mass can be contained within the crevice volume, as illustrated for this case by the simulation images of Figure 54 colored by density.

This observation may not be unique. The same effect could be present in a typical SI engine combustion chamber since it is the result of the compressive action of the propagating flame [30]. Still, the similarity of the AHRR signature of this case to one with moderate EGAI is troublesome. The Schlieren images recorded for the representative experiment upon which this simulation was built are included in Figure 56 for further review.

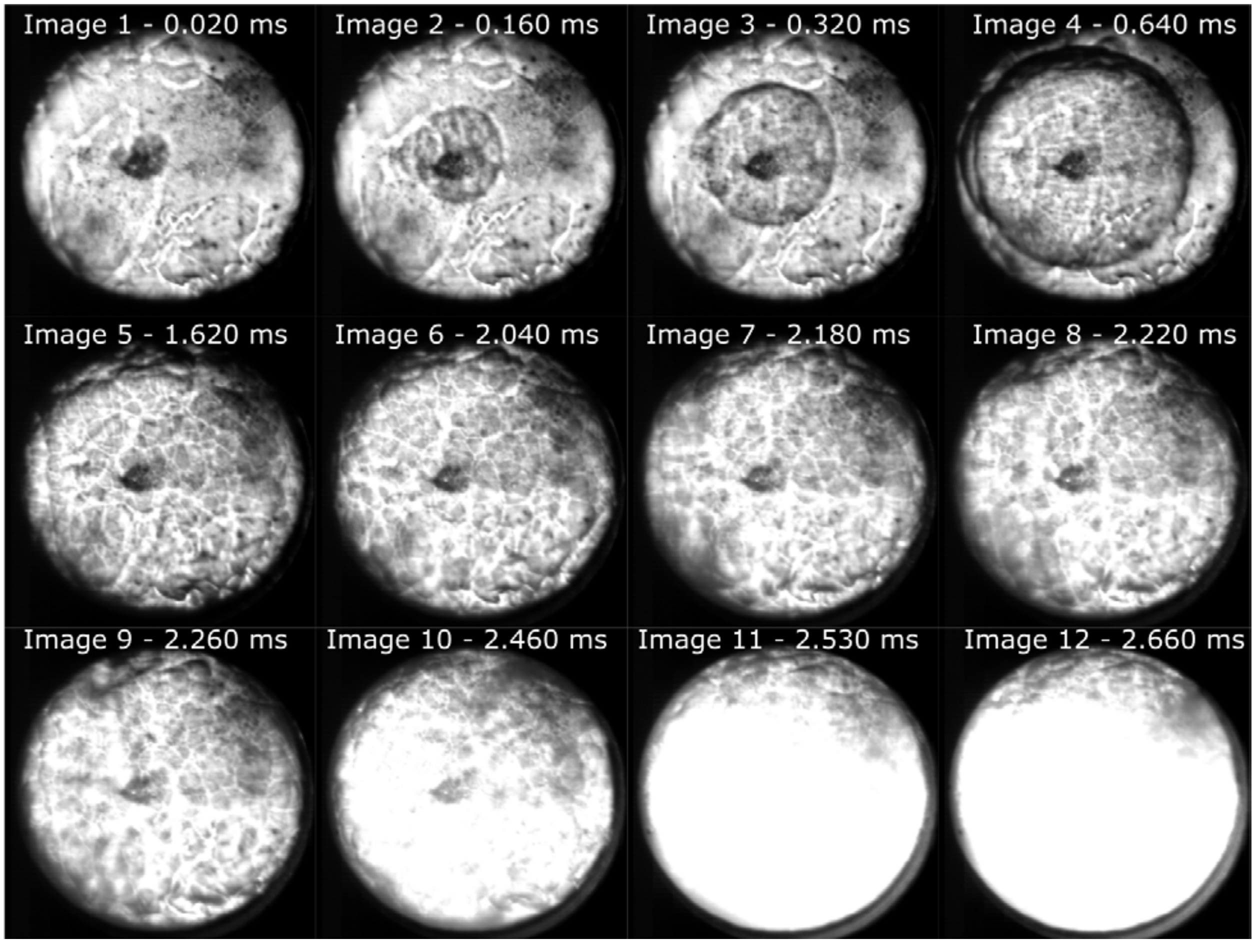

Figure 56. Schlieren images from the wet blend NG experiment selected for modeling.

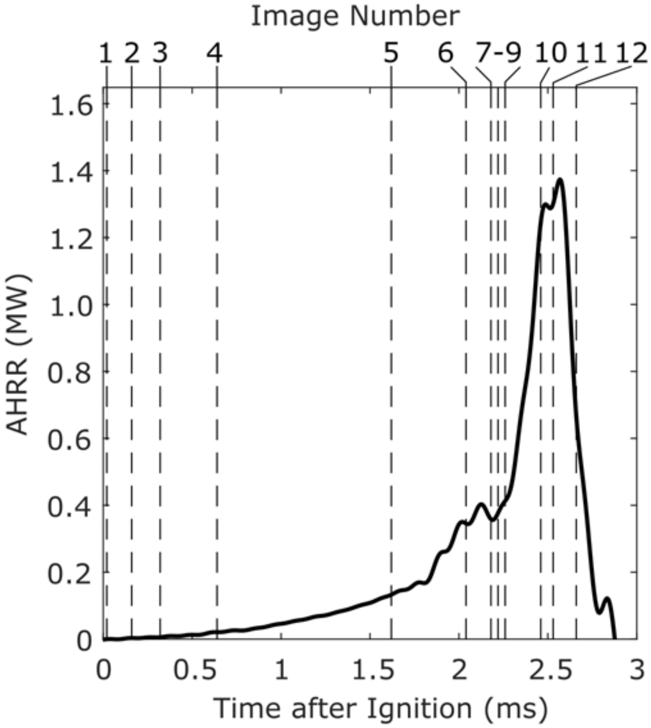

Figure 57. Experimentally measured AHRR profile corresponding to the images of Figure 56.

Here, in still motion form, the typical progression of the propagating flame triggering EGAI may be suggested, but in fact there is very little optical evidence of any volumetric heat release. The transition to the bright white frame of images 10 and 11 does not appear to be the result of a distinct change in the end-gas, as it is in the previously presented image sequences of §5.4 for PRF blends (note, again, such a difference is difficult to present in still image form). Instead, the flow field becomes highly turbulent and what appear to be multiple other flame fronts enter the field of view. The frames then become over exposed with light. This type of transition is distinctly different from the volumetric EGAI events observed previously. In fact, there is no definitive evidence of EGAI in the images or in the AHRR signature.

This experiment and its corresponding simulation were performed well after the others involving PRF blends. Recall that there is substantial experimental evidence suggesting that no crevice volume combustion is occurring in the PRF blend cases, as discussed in §5.5, but the dataset for the NG fuels is not yet large enough to perform a similar analysis. What is learned from this particular experiment/simulation is that uncertainties surrounding the combustion behavior in the laser-ignited RCM experiments still exist.

Without the luxury of being able to see a spatial map of the volumetric heat release, the AHRR peak of these profiles would be, and still are, identified as EGAI. This is obviously problematic as crevice volume combustion cannot be distinguished from EGAI and therefore could be mistakenly identified as EGAI in the experiments. Should that be the case however, the consequences are not dire for the concept of the experiment, just for the application of creviced pistons in the experiments. Discussion on possible improvements to the combustion chamber design are included in 6.3.

6.3 Using CFD to Explore Alternative Combustion Chamber Designs

With a more complete understanding of the complications introduced by crevice volume combustion, alternative combustion chamber designs that are better suited for the objectives of laser-ignited RCM studies were explored. Two options were proposed. One option would be to eliminate the crevices completely. Doing so would compromise the adiabatic core assumption, as much higher levels of turbulence would be introduced to the flow field by compression, but would eliminate the possibility of crevice volume combustion. Alternatively, a crevice containment strategy could be implemented. Here, the crevice volumes would be connected to the main chamber while the pistons are in motion, but would be closed off as the pistons reach their TDC positions. The flow-field benefits of creviced piston design would thus be maintained, but the possible effect on combustion progression would be eliminated. This section briefly reviews the proposition to eliminate the crevice volumes using CFD models. Crevice containment strategies are also introduced. Neither section is meant to serve as a complete design review.

A symmetric compression model was constructed for the crevice volume elimination proposition. Compression ratio was maintained at 11.6:1 and the characteristics of the compression event were kept largely the same. A thermal hotspot was initiated in the center of the chamber 10 ms after the pistons reached TDC. Six fuel reactivities were tested, ranging from PRF 50 to PRF 100, under stoichiometric conditions with an inert/oxidizing blend of 79% N_2 / 21% O_2. Initial pressures and temperatures were maintained at 1.000 bar and 300 K respectively. The resulting AHRR profiles are presented in Figure 58, colored by ON.

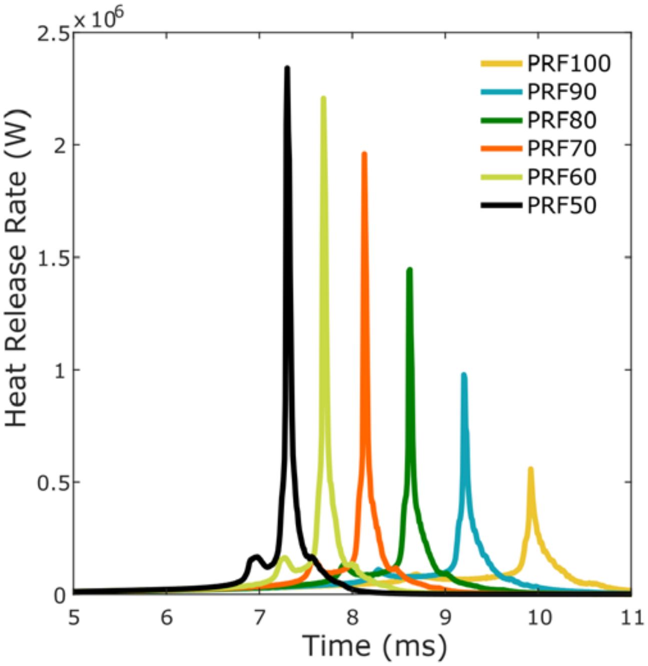

Figure 58. AHRR profiles for a range of fuel blends in laser-ignited RCM simulations with crevice-less pistons.

Despite the loss of the quiescent, adiabatic core, the expected trends with ON are maintained. With increasing fuel reactivity, the magnitude of the EGAI events rises and their timing advances. Further, the AHRR signatures are just as discernable as they are with the current combustion chamber. Unique AHRR peaks can be identified and used to denote specific combustion behavior (e.g. propagating flame, LTHR, EGAI) without the complication of potentially misidentifying crevice volume combustion as EGAI.

What is lost by eliminating the crevice volumes is the ability to make the assumption that the compressed gases form a largely homogenous core. The roll-up vortices on the front faces of the pistons would compromise the quiescence of the gas. Flame propagation rate measurements, being highly sensitive to turbulence, would be less telling and EGAI events would be subject to random spatial gradients and inhomogeneities. The ability to create a high-temperature high-pressure reactive gas mixture with minimal fluid dynamic disturbances is central to the objectives of this research and to other applications of the RCM. Disruption of the flow field undermines the quality of the experiment as it applies to fundamental combustion studies, and as such, elimination of the crevice volumes is not recommended.

The alternative approach of implementing a crevice containment strategy is more appealing, as it is thought to avoid disturbance of the flow field. Figure 59 includes a graphical illustration of how this might be achieved. The current combustion chamber could be modified to house an insert that extrudes from the chamber wall at a position that coincides with the TDC positioning of the crevice volume channel. During compression, the creviced piston behaves as it otherwise would, redirecting the roll-up vortex and minimizing fluid dynamic disturbances. Upon reaching TDC, the outer edge of the piston face slightly interferes with the insert, closing off the crevice volumes from the main chamber. The insert could be composed of something as simple as a rubber o-ring, but it could also be machined from a soft metal if melting of o-rings becomes an issue. Other research groups have proposed similar designs [31].

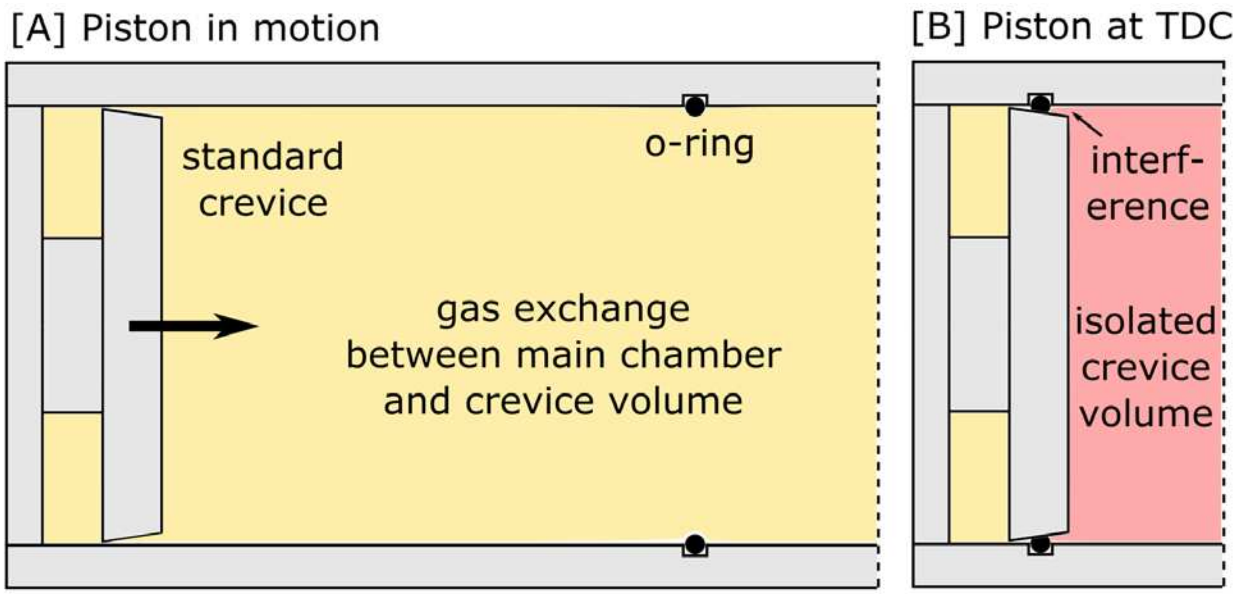

Figure 59. Illustration of a possible crevice containment modification featuring an o-ring positioned to interfere with the piston's crevice channel at the TDC position.

Construction of CFD models for crevice containment strategies has begun, but more work needs to be done before they are fully operational, let alone capable of informing design decisions. Much attention was paid to accurately modeling o-ring interfering surfaces (the outer edge of the piston and the o-ring) in the prototype computational domains, ultimately to the detriment of the model. Future researchers should avoid wasting time modeling such systems with excessive detail. Here, a model that simply constrains the flow entering the crevice volumes after TDC would suffice.

The symmetric domain from §6.1 serves this purpose. The flow-through boundaries imposed at the channel inlet were previously used to force a quench condition while still allowing gas exchange between the main chamber and the crevice volumes. To simulate crevice containment, these flow-through boundaries are switched to the wall type after the pistons reach TDC. The simulation is stopped at the time of ignition (as is already done to initialize the thermal hotspot ignition site) and the domain is modified to remove the crevice volumes. The new domain is then mapped by the output variables recorded just before the simulation was stopped. Thus, the actual domain shape changes at the time of ignition, as depicted by Figure 60. Though this is obviously not a perfect representation of the real-world crevice containment designs, it does allow for the effect of crevice containment on the combustion physics to be explored.

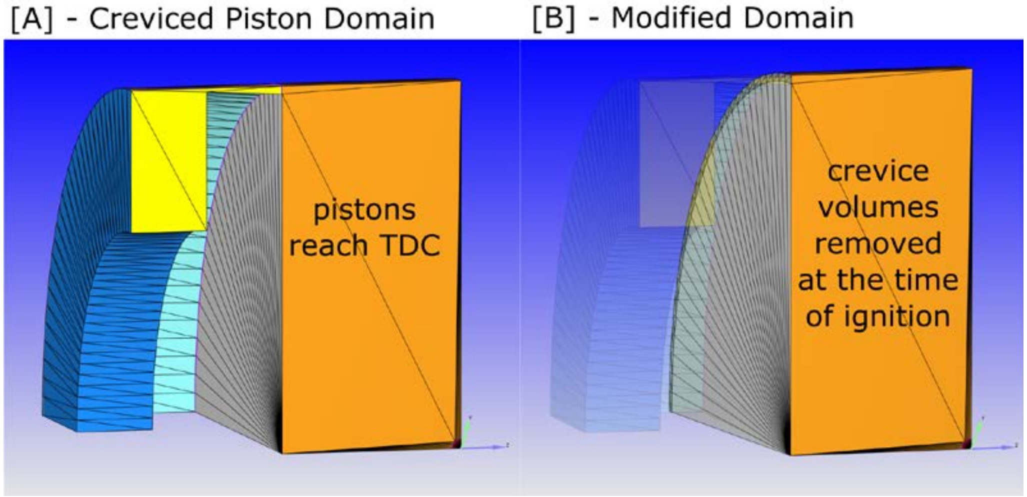

Figure 60. Screenshots of the computational domains for the crevice containment simulation. During compression, the crevices are continuous with the main chamber, as shown in [A]. At the time of ignition, the crevice volumes are removed as shown in [B].

The PRF 50 simulation with the 6.42 Ks compression from §6.1 was repurposed to explore this crevice containment strategy. A comparison between the pressure and AHRR profiles of the quenched condition and of the crevice containment condition are shown in Figure 61. What distinguishes these two cases is the size of the volume into which the unburned end-gases are compressed. The gases ahead of the flame front in the standard domain can flow into the crevice volumes, but those in the crevice containment domain have nowhere to go. This is an important distinction as it determines how quickly temperatures rise in the end-gas due to the compressive action of the approaching flame. EGAI occurs later in the standard case for this very reason. EGAI magnitude is likewise affected, but twofold. First, the standard case's later phasing of the EGAI event allows time for more of the reactive mixture to be consumed by the propagating flame – a lower f_{EGAI} results. Second, because of the quench condition in the standard case, unburned gases are leaving the reactive region that is the main chamber when they enter the crevice volume. As will be discussed in §6.4, the effect of this is that less of the reactants are consumed by either combustion event – lower peak pressure and f_{EGAI} result.

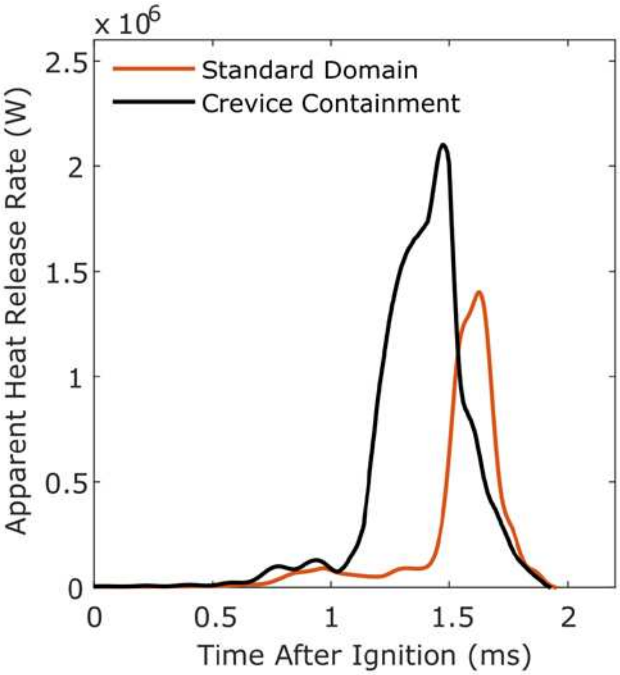

Figure 61. Comparison of the AHRR profiles of a PRF 50, 6.42 Ks simulation. The red line represents the standard case in which the crevice volume remains continuous with the main chamber throughout. The black line represents the crevice containment model in which the crevice volume is deleted from the domain at the time of ignition.

There has been nothing yet to suggest adverse effects to the experiments should crevice containment strategies be implemented. Practical containment designs will form the foundation for the ideal RCM combustion chamber. That said, not much effort has been expended in designing such a system and several hindrances to the process are immediately apparent: (1) risk of crashing the pistons into the inserts, which may be installed improperly or may have dislodged during testing; (2) the pistons getting stuck in their TDC positions because of interference with the inserts;

(3) damage to the insert's sealing surface due to extreme temperatures. There are likely others, but none so far have seemed insurmountable. Going forward, it is recommended that crevice containment strategies are explored more thoroughly.

6.4 Model Value, Limitations, and Uncertainties

Modeling efforts began with the intention of studying the physics of EGAI, but ended up being most valuable as a means of developing a better understanding of the experiment. Simulations proved valuable in characterizing AHRR signatures and the types of combustion behavior associated with them and probing for weak points in the experimental concepts.

With regard to the question of crevice volume combustion, the only certain conclusion that can be drawn is one of uncertainty. The likely reality is that crevice volume combustion is conditional. Preliminary results for the NG experiments suggest that crevice volume combustion serves as the primary heat release event while trends in the larger dataset of the PRF blend experiments give evidence that the crevices do not burn at all. Though an unsatisfying conclusion, the reality is that the degree to which the experiments are affected by crevice volume combustion is unknown. The computational models were useful simply in drawing attention to the problem and to its possible consequences with regard to the premise of the experiment.

The consequences of crevice volume combustion to the experimental concepts have already been discussed at length. What has not yet been discussed are the limitations imposed on the model if crevice volume combustion is *not* occurring. In essence, the quench condition at the crevice volume channel established "non-reactive" secondary volumes separate from the main "reactive" chamber. The consequence is that unburned reactants are redirected into the crevice volumes as the flame propagates, leaving the part of the chamber within which they can be consumed, and end up not burning at all. This means that, if in fact combustion events are quenched at the crevice inlet in the laser-ignited RCM experiments, the amount of fuel/oxidizer mass that participates in the reactions will be subject to the timing of the EGAI events, and the peak pressure and AHRR of the model will likewise be affected. The further the propagating flame is allowed to travel, the more reactive mixture is directed into the crevice volumes and the lower the resulting combustion efficiency due to the quench condition not allowing the mass in the crevice volumes to burn. The resulting trends between EGAI time and apparent combustion efficiency have indeed been observed for the PRF blends experimentally (see §5.1).

The consequence of the quench condition to the model is that matching peak pressure and AHRR to what is observed experimentally becomes extremely difficult as it is highly sensitive to EGAI timing and flame propagation rate. Should flame speed be under-predicted, the flame front will consume less of the mixture prior to EGAI, effectively resulting in more reactive mass participating in combustion and higher peak pressures and AHRRs. Should EGAI occur earlier in the simulation than in does the experiment, more trapped mass will participate in the reactions of the simulation and the peak AHRR and pressure will be over-predicted.

Agreement between the models and the experiments is also sensitive to the proper representation of the volume, as it determines the trapped mass, and the compression ratio of the combustion chamber. Both are subject to change with configuration of the RCM and the combustion chamber from day to day. Installation of the piston faces onto the plunger assemblies is less than consistent due to the current seal layout. The pistons do not “bottom out” onto the plunger shaft, but rather compress a Teflon seal until they can no longer be threaded. This leads to the pistons being installed at slightly different depths every time they are serviced, resulting in a change in trapped mass and compression ratio. The combustion chamber windows and auxiliary instrumentation are installed in a similar way and can result in the same.

The variation in chamber volume and compression ratio is less of a modeling limitation than it is a frustrating complication in consistency of the experiments. Compression ratio was estimated via a combination of direct measurement techniques and correlations with isentropic/polytropic compression relations. Except for the case in which major modifications were made to the fill port valve, the compression ratio was assumed constant at 11.6:1. As such, variation in the chamber volume and compression ratio in the experiments is likely contributing to the observed differences in peak pressure and AHRR between the simulations and experiments.

The heat transfer correlations, as they apply to the low-turbulence RCM simulations, also lead to uncertainties in the simulations. This also surely contributes to the observed differences, but is less of a fundamental limitation to the model. Heat transfer coefficients could be tuned to better match experimental rates and the simulations could be calibrated to account for differences.

The development of a predictive model was never the goal. Despite clear differences in the results of the experiments and of the simulations, the qualitative agreement of the observed trends speaks to the model value. Simulations served as a means to better understand the experiment and its sensitivities, ultimately giving insight into the combustion physics underlying EGAI.

CHAPTER 7 – CONCLUSIONS AND FUTURE WORK

Modern engines operating beyond the conditions commensurate with the RON/MON metrics require the development of new methods to characterize fuel reactivity and knock propensity. So too, does the development of future fuels with reactivity behavior that deviates from that of alkanes. Specifically, fuel reactivity measurement methods must enable a wide variation in end-gas conditions (pressure, temperature, and speciation), incorporate advanced diagnostics to elucidate the onset of EGAI, require small quantities of fuel, and be amenable to comparisons against computational modeling.

The results of this study demonstrate the ability to evaluate knock propensity of SI fuels through observation of EGAI in the unburned gases upstream of laser-ignited, premixed flames at engine-relevant pressures and temperatures in an RCM. To demonstrate this principle, stoichiometric PRF blends of varying reactivity ($50 \leq ON \leq 100$) were ignited over a range of temperatures and pressures, all in excess of 545 K and 16.1 bar, producing outwardly propagating, laminar premixed flames. High-speed pressure measurements, paired with Schlieren imaging, clearly indicated the presence of EGAI. The magnitude of the EGAI event, as quantified by the fraction of the total heat release contributed by EGAI, was subject to fuel reactivity, temperature history, turbulence, and time.

Experiments were accompanied by three-dimensional computational models with detailed chemical kinetics performed using CONVERGE^{TM} CFD software. Excellent quantitative agreement with the experiments was achieved. Models were employed to investigate the combustion physics behind EGAI, inform experimental findings, and explore alternative combustion chamber designs.

This final chapter serves as an evaluation of the degree to which the objectives defined in §1.4 were met. Informed by the experimental and computational findings, the potential for the RCM to be used as a knock propensity measurement instrument is first assessed. To improve its ability to serve those ends, design modification recommendations for the experimental platform are next given. Last, future work is discussed, inclusive of how the developed methods could be applied to test real fuels and of the challenges that still impede the development of a comprehensive knock propensity metric.

7.1 RCM as a Potential Knock Propensity Measurement Instrument

Towards the standardization of a knock propensity measurement method involving spark-ignited RCM experiments, results were promising, but more work needs to be done. The RCM certainly proved itself a worthy platform for conducting fundamental SI combustion studies. Single-point ignition was reliably achieved in high-temperature, high-pressure conditions with minimal flow disturbances. Associated instrumentation allowed for the clear identification and quantification of EGAI events. These findings show promise for the developed methods and serve as a general proof of concept for using an RCM to measure knock propensity.

What is lacking in this particular experimental platform is consistency. Variability in compression speed and symmetry was found to have significant influence over TDC thermodynamic and fluid dynamic conditions. For a given set of initial conditions, temperatures after compression were observed to vary by as much as 80 °C. Volumetric combustion events are of course extremely sensitive to temperature, and such variability is unacceptable in an instrument purposed to measure a test fuel’s propensity to autoignite under specific, repeatable conditions.

To account for compression variability in this study, selection criteria for the TDC conditions were imposed. Analysis of the full dataset revealed EGAI phenomena to be most sensitive to the temperature history before spark-ignition (indicated by the time-integrated temperature over the 10 ms prior to the spark) and to the relative turbulence levels of the flow field (indicated by the piston offset). EGAI was found to be much less sensitive to chamber pressure. Grouping experiments by their TDC conditions rather than by their initial conditions vastly improved the consistency of the observed combustion phenomena (e.g. EGAI magnitude, flame speed) amongst trials being identified as of the same sort.

Still, even with relatively strict TDC condition criteria, the resolution by which f_{EGAI} can indicate a fuel's knock propensity through the traditional metrics (i.e. RON, MON, octane index) is currently lacking. That is, there exists potential to correlate a fuel's f_{EGAI} with what would be its ON as measured by a CFR engine, but the derived ON appears to be too sensitive to variability in the f_{EGAI} measurements for this to be possible. A likely solution to this lack of resolution is repetition. Standardized cetane number measurement instruments like the ignition quality tester (IQT) perform over 25 cycles to return a single measurement and a similar approach could be taken with an RCM. Large numbers of replicate cycles that meet target TDC condition criteria could increase confidence in the f_{EGAI} measurements and the resolution by which ON could be derived.

The claim, then, is not that the laser-ignited RCM experiments are currently a viable alternative to ON measurement using a CFR engine. The claim is that there is potential for them to be. Laser-ignited RCM experiments are a controllable analog to premixed SI engine operation. They could be tuned in a way so as to promote the observation of EGAI over a range of thermodynamic conditions relevant to modern engine operation. If consistency of the compression events could be improved, f_{EGAI} could very well give a better indication of a fuel's propensity to knock under such conditions. Further still, f_{EGAI} offers a quantification of the magnitude of EGAI events, where ON merely indicates their onset. The ability to quantify EGAI magnitude with precision lends itself to applications in which low levels of EGAI could be controlled and tolerated rather than simply avoided.

7.2 Design Considerations for the Experimental Platform

There are a number of limitations that may impede the RCM's application as a dedicated knock propensity measurement instrument in its current configuration. Identified by the combined experimental and computational efforts of this study, those limitations are: (1) the consistency of the speed and symmetry of the compression events, (2) the time it takes to perform a complete cycle (currently ~15 minutes), and (3) the potential for ignition of the crevice volumes paired with the inability to distinguish that behavior from other volumetric combustion events using the AHRR signatures alone. These do not seem to be insurmountable challenges.

Compression consistency issues are unique to dual-piston machines. The time it takes for an individual piston to complete its stroke is relatively constant. The inconsistencies in speed and symmetry arise with piston offset, in which one piston is released considerably before the other. Bulk fluid motion is introduced, cascading to smaller length-scale turbulence, and the effective time of the compression event is extended by the piston offset.

Improving the compression consistency of the machine is conceptually quite simple. The dual piston layout could be converted to a single piston platform by removing one of the drive cylinder assemblies and capping the end of the combustion chamber. This would eliminate the problem of piston offset to the detriment of either the machine's high-compression ratio or high-volume, low-aspect ratio chamber at TDC. Still, a capped combustion chamber would allow for the installment of a larger viewport and the added ability to observe combustion phenomena in the extremities of the chamber. Note that the global time at which the piston's drive assembly begins to move would still be variable – i.e. the time at which the piston begins to move relative to when the RCM trigger is pressed would still be variable. This is not an issue, should the auxiliary systems remain triggered by the chamber pressure rise rather than from the electrical signal of the RCM trigger. Alternative designs could also be proposed, including the installment of a mechanical linkage between the two drive assemblies. This would be a challenging design project, but if successful, would make the compromise between compression ratio, chamber aspect ratio, and consistency unnecessary.

It is suspected that even when subjected to perfectly consistent compression events, inherent randomness in the SI combustion events will require that many replicate trials be performed to return a measurement with high confidence. To improve the platform's aptitude as a knock propensity measurement instrument, cycle times must be improved. Currently, the most time-expensive portion of the testing procedure is the gas exchange process, followed closely by the charging of the pneumatic bellows for firing. The advantage of the current layout is simplicity and ease of use. An RCM purpose built as a knock propensity measurement instrument could employ valve designs that are far superior to the current ball-valve fill port and the gas-exchange process could be automated quite easily. Currently, exhaust gases are vacuumed out of the chamber when the pistons are at their BDC positions. Opening the fill valve and vacuuming at TDC would cut operation time by an order of magnitude. The RCM manifold could also be fit with a regulator capable of achieving precise fill pressures in short periods of time. The implementation of these modifications, along with automated valves and faster drive mechanisms, would reduce cycle times significantly.

Last is the problem of crevice volume combustion, with perhaps the simplest of solutions. As section §6.3 discusses at length, the crevice volumes could be removed completely with minimal effect on the EGAI physics. Further, crevice containment strategies could be employed such that quiescent chamber conditions could be maintained, but the possibility of crevice combustion would be eliminated. These solutions would be simple to implement and low cost. Other considerations include the enlargement of the viewports to see the full extent of the combustion chamber or the improvement of pressure filtering techniques to gain the ability to distinguish between crevice volume combustion and EGAI with accuracy. Considerable effort has been expended towards the latter with no improvement.

The current CSU RCM platform is tailored to host a wide variety of experiments, but could be modified to improve compression consistency and cycle repetition rate to serve as a dedicated knock propensity measurement instrument. Crevice containment or elimination strategies should be explored first, as the gained confidence in the measured AHRRs from their implementation will far outweigh the design and manufacturing effort expended.

7.3 Future Work

In summary, this study has revealed promise for an RCM to serve as a knock propensity measurement instrument. The experimental and computational results presented herein provide the foundation upon which future SI combustion studies can be conducted. This foundation itself was built on the collective efforts of Ciprian Dumitrache and Andrew Boissiere, whom developed the first laser-ignition and Schlieren imaging systems for the RCM [19]. With the groundwork in place, the real fundamental SI combustion research can begin. Beyond modifications to the experimental apparatus, opportunity exists to begin testing real fuels with sensitivities, refining

f_{EGAI} measurement techniques such that ON can be derived, developing new knock propensity standards that are not anchored to the CFR engine platform, and using EGAI magnitude as a control parameter to boost combustion efficiency in engines in which low levels of EGAI can be tolerated.

The major barrier that remains in the way of the development of a comprehensive knock propensity metric is the challenge of summarizing a fuel's combustion tendencies across a wide range of operating conditions with a single number, comprehensible to the lay-user. The RON and MON metrics were purposed to span the NTC region of a tested fuel and thus provide an overview of how the fuel may behave in the common engine. However, MON has been proven to be antiquated and has little relevance to modern engine operation. The natural gas industry is struggling with same problem of methane number (MN) standardization, with little agreement on how best to summarize gaseous fuel knock propensity over a wide range of fuel compositions and engine operating conditions [8,32]. This in mind, an experimental platform that allows for the precise control of SI combustion phenomena lends itself to experiments from which new knock propensity measurement standards could be developed. An RCM with SI capability can be used to investigate the complexities of SI combustion physics and may help overcome these challenges.

BIBLIOGRAPHY

[1] J.B. Heywood, Internal combustion engine fundamentals, McGraw-Hill, New York, 1988.

[2] S.R. Turns, An introduction to combustion: concepts and applications, 3rd ed, McGraw-Hill, New York, 2012.

[3] J. Livengood, P. Wu, Correlation of autoignition phenomena in internal combustion engines and rapid compression machines, Symp. (Int.) Combust. (1955) 347–356.

[4] A. Vressner, A. Lundin, M. Christensen, P. Tunestal, B. Johansson, Pressure Oscillations During Rapid HCCI Combustion, SAE Technical Paper Series. (n.d.).

[5] D. Montgomery, MECH 580B1-001: Industrial Gas and Dual Fuel Engines - IC Engine Abnormal Combustion Lecture, (2018).

[6] ASTM D2700-12: Standard Test Method for Motor Octane Number of Spark-Ignition Engine Fuel, (2018).

[7] ASTM D2699-12: Standard Test Method for Research Octane Number of Spark-Ignition Engine Fuel, (2018).

[8] A.A. Attar, G.A. Karim, Knock Rating of Gaseous Fuels, Journal of Engineering for Gas Turbines and Power. 125 (2003) 500. doi:10.1115/1.1560707.

[9] G.T. Kalghatgi, Fuel Anti-Knock Quality- Part II. Vehicle Studies - How Relevant is Motor Octane Number (MON) in Modern Engines?, SAE International. (2001).

[10] C.K. Law, Combustion physics, Cambridge University Press, Cambridge ; New York, 2006.

[11] G.T. Kalghatgi, Developments in internal combustion engines and implications for combustion science and future transport fuels, Proceedings of the Combustion Institute. 35 (2015) 101–115. doi:10.1016/j.proci.2014.10.002.

[12] G.T. Kalghatgi, Fuel Anti-Knock Quality - Part I. Engine Studies, SAE International. (2001).

[13] Z. Wang, H. Liu, R.D. Reitz, Knocking combustion in spark-ignition engines, Progress in Energy and Combustion Science. 61 (2017) 78–112. doi:10.1016/j.pecs.2017.03.004.

[14] S. Bhoite, A Computational Study of Autoignition, Spark Ignition and Dual Fuel Droplet Ignition in a Rapid Compression Machine, Colorado State University, 2017.

[15] Y. Qi, Z. Wang, J. Wang, X. He, Effects of thermodynamic conditions on the end gas combustion mode associated with engine knock, Combustion and Flame. 162 (2015) 4119–4128. doi:10.1016/j.combustflame.2015.08.016.

[16] C. Dumitrache, M. Baumgardner, A. Boissiere, A. Maria, J. Roucis, A.J. Marchese, A. Yalin, A study of laser induced ignition of methane–air mixtures inside a Rapid Compression Machine, Proceedings of the Combustion Institute. 36 (2017) 3431–3439. doi:10.1016/j.proci.2016.05.033.

[17] C.-J. Sung, H.J. Curran, Using rapid compression machines for chemical kinetics studies, Progress in Energy and Combustion Science. 44 (2014) 1–18. doi:10.1016/j.pecs.2014.04.001.

[18] M. Baumgardner, Characterizing Fuel Reactivity in Advanced Internal Combustion Engines, Dissertation, Colorado State University, 2014.

[19] C. Dumitrache, M. Baumgardner, A. Boissiere, A. Maria, J. Roucis, A.J. Marchese, A. Yalin, A study of laser induced ignition of methane–air mixtures inside a Rapid Compression Machine, Proceedings of the Combustion Institute. 36 (2017) 3431–3439. doi:10.1016/j.proci.2016.05.033.

[20] G.A. Karim, Combustion in Gas Fueled Compression: Ignition Engines of the Dual Fuel Type, Journal of Engineering for Gas Turbines and Power. 125 (2003) 827. doi:10.1115/1.1581894.

[21] A.P. Kelley, C.K. Law, Nonlinear effects in the extraction of laminar flame speeds from expanding spherical flames, Combustion and Flame. 156 (2009) 1844–1851. doi:10.1016/j.combustflame.2009.04.004.

[22] CONVERGE Manual, (n.d.).

[23] S. Kenjereš, K. Hanjalić, Tackling complex turbulent flows with transient RANS, Fluid Dynamics Research. 41 (2009) 012201. doi:10.1088/0169-5983/41/1/012201.

[24] H. Wang, M. Yao, R.D. Reitz, Development of a Reduced Primary Reference Fuel Mechanism for Internal Combustion Engine Combustion Simulations, Energy & Fuels. 27 (2013) 7843–7853. doi:10.1021/ef401992e.

[25] M.B. Luong, Z. Luo, T. Lu, S.H. Chung, C.S. Yoo, Direct numerical simulations of the ignition of lean primary reference fuel/air mixtures with temperature inhomogeneities, Combustion and Flame. 160 (2013) 2038–2047. doi:10.1016/j.combustflame.2013.04.012.

[26] Y.A. Çengel, M.A. Boles, Thermodynamics: an engineering approach, Eighth edition, McGraw-Hill Education, New York, 2015.

[27] X. Hui, C.-J. Sung, Laminar flame speeds of transportation-relevant hydrocarbons and jet fuels at elevated temperatures and pressures, Fuel. 109 (2013) 191–200. doi:10.1016/j.fuel.2012.12.084.

[28] E. Toulson, H.J. Schock, W.P. Attard, A Review of Pre-Chamber Initiated Jet Ignition Combustion Systems, in: 2010. doi:10.4271/2010-01-2263.

[29] I. Glassman, R.A. Yetter, N. Glumac, Combustion, Fifth edition, Academic Press, Waltham, MA, 2015.

[30] J. Hiltner, MECH 580B1 - 001: Industrial Gas and Dual Fuel Engines Lecture, (2018).

[31] G. Mittal, A. Bhari, A rapid compression machine with crevice containment, Combustion and Flame. 160 (2013) 2975–2981. doi:10.1016/j.combustflame.2013.06.027.

[32] V.N. Korolev, A.V. Marugin, Determination of the octane number of a fuel by the IR spectroscopy method, Journal of Applied Spectroscopy. 67 (2000) 336–342. doi:10.1007/BF02681855.

[33] A. Boissiere, Effect of Additives on Laser Ignition and Compression Ignition of Methane and Hydrocarbons in a Rapid Compression Machine, Master of Science, Colorado State University, 2016.

APPENDIX A – LASER MAINTAINENCE AND OPERATION

Warning: *Do not attempt to use the laser until having received proper instruction regarding laser safety and this particular unit's functionality.*

The Quantel Q-Smart 100 features a liquid-cooled laser head. Though maintenance procedures for this system once installed should be minimal, ensuring that the cooling system has the appropriate amount of coolant and is well bled is absolutely essential to proper, reliable operation. The coolant tank is housed as part of the main control and power supply unit, pictured in Figure 62 (a) and (b), featuring a liquid level indicator window on the back labeled "B2" in the figure. Coolant supply and return lines (B5) are color coded blue and red respectively, and care should be taken to avoid pumping the coolant in the wrong direction (i.e. hooking the blue supply line up to the red return outlet on the laser head). The coolant pump can be manually operated using the green button (B1) on the back side of the control unit. Air bubbles can be removed from the coolant lines by situating the control unit housing above the laser head, such that the coolant tank is the highest point in the system, and then running the pump for several seconds or until no bubbles are seen passing through the lines. Distilled water was the coolant of choice upon installation of the system. Occasional checks to make sure that the water is free of contaminants are recommended.

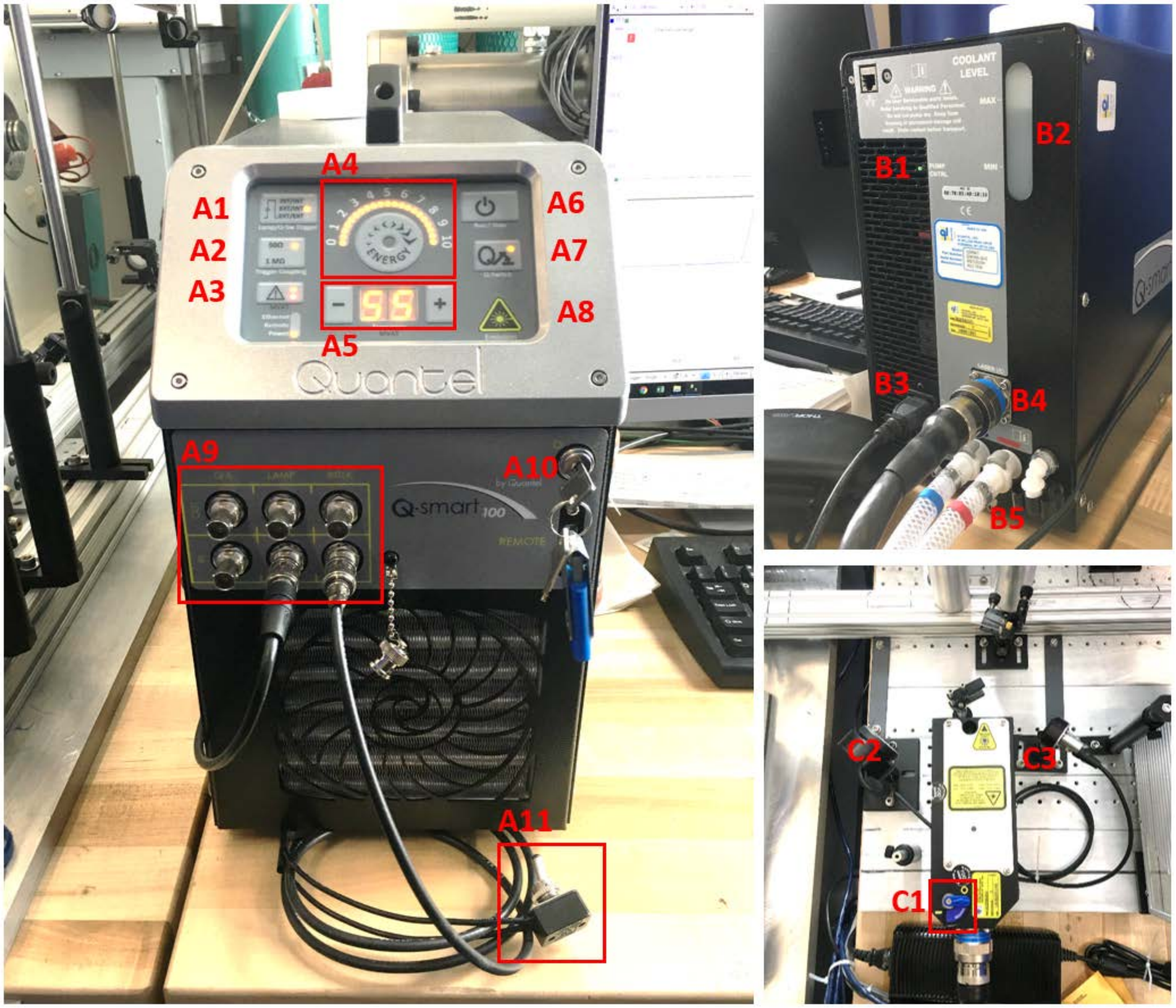

Figure 62. (a) Quantel Q-smart 100 laser control unit, power supply, and cooling tower. (b) Rear view of control unit. (c) Nd.YAG 1064 nm liquid-cooled laser head. Energy meter, photodiode, and beam splitters also shown.

The laser system can be configured to serve in a variety of applications. As a dedicated ignition source for the RCM, the laser is setup to run in single-shot mode, but running in continuous mode will be required for laser alignment. To configure the laser, first ensure that the mil-spec data transfer cable (B4) is properly connected to both the control tower and laser head. Turn the system on using the key on the front of the control unit (A10).

Single-shot mode requires a trigger input voltage pulse via the LAMP-IN port of the BNC cluster (A9). The voltage pulse is provided by a pulse-delay generator that is itself triggered off the pressure rise outputted from the charge amplifier for the in-cylinder piezoelectric pressure transducer. These systems are described in detail later in this section. Select "EXT/INT" mode with the "Lamp/Q-Sw Trigger" button (A1) on the control panel. This specifies that the flash lamp pump will be triggered via external means and the Q-switch will be triggered according to optimum timing specifications by the control unit itself.

The external trigger source should be used with the 50 Ω "Trigger Coupling" mode (A2). Configure the pulse-delay generator to be gated off of the output pressure reading voltage from the Kistler charge amplifier. All experiments in this thesis were conducted with a 0.40 V gate with the charge amplifier set to 25.00 bar/V. That is, a pressure reading at or above 10 bar would set off the pulse-generator that will subsequently trigger the laser after a prescribed delay period. The voltage pulse sent to the LAMP/IN port is a 5 V square wave with a width of 0.005 s at a delay of 0.014 s. This delay period with the 0.40 V gate was found to result in an average ignition timing of 0.010 s after the pistons reach TDC, but there is significant variability in that ignition timing due to variation in compression speed.

It is highly recommended to setup the photodiode (C3) and energy meter (C2) optical paths at this point, as they will affect the alignment of the main pathway. Never subject either instrument to the full power of laser and become familiar with the damage threshold limits prior to use. In its current configuration, two microscope slides are used to successively split the main beam, each redirecting approximately 5% of the incoming beam to their respective instruments. The photodiode is kept off, but still produces a voltage reading when subjected to the incoming beam. The Picoscope DAQ unit collects the voltage reading from the photodiode and records the relative timing of the laser pulse and compression event. The energy meter communicates with the Ophir software package which displays pulse-by-pulse energy measurements. These measurements are taken from the redirected path such that the actual amount of energy reaching the chamber is a function of the measured and energy and the emissivity of the optical components in the beam path - the two microscope slides, lenses, mirrors, and window. Though this emissivity does vary, for simplicity, it has been assumed that it does not change and that the amount of energy that reaches the chamber is a constant 14.602 times what is experimentally measured, based on the initial findings recorded when all optical components were clean. To configure the laser for alignment procedures, switch over to continuous mode (INT/INT trigger) on the control panel, and select the lowest energy level with the scroll wheel (A4) with a shot frequency of 1-2 Hz, adjusted with + and – buttons (A5). Refer to the instructions provided by Thorlabs to perform the beam alignment.

Once the trigger system has been configured and the beam properly aligned, switch back over to “EXT/INT” trigger mode and select the appropriate beam energy and frequency levels. Single shot mode is displayed as “SS” (do not mistake for “55 Hz”!) and is one setting lower than “01” Hz continuous mode. It is recommended that the operator start at the lowest energy setting, gradually increasing the level until a spark is formed. This can be easily accomplished by filling the combustion chamber with 1.000 bar of nitrogen and running the laser continuously (“INT/INT” mode) at a frequency of 1-2 Hz, increasing the energy until sparks are formed.

Finally, to arm the laser and prepare for firing, toggle the interlock switch (A11) such that the red interlock light (A3) goes out. Notice that the yellow interlock light (A3) remains lit, as there are system trouble codes that need to be cleared before the system can enter run mode. In order to clear these codes, press the interlock button (A3) several times to scroll through the warning code list. Upon reaching the end of the list, the yellow light extinguish and the system will be ready to arm. Of course, it is good practice to know what the warning codes mean. Ordinarily, they are only indicating that the interlock was activated and is now turned off, but the possibility exists for more serious problems (e.g. overheating laser head) to be called out here. Next, ensure that the Q-Switch indicator light (A7) is illuminated , open the shutter (C1) on the laser head, and press the “Run/Stop” button (A6) on the control unit to arm the laser. At this point, in single shot mode, the system is waiting for the signal from the external trigger to fire. A yellow warning light blinks from the emission port of the laser head periodically to indicate that the system is armed and that extreme caution should be implemented. Confirm that the pulse-delay generator is in run mode and fire the RCM. Evidence of the laser being fired is provided by a spike on the photodiode readout and a beam energy measurement recorded on the Ophir user interface.

It is important to consider that the cleanliness of the inside surface of the laser optical port on the combustion chamber will affect the amount of energy required to produce a spark. So too will the mixture composition and thermodynamic conditions. Excessively high spark energies have the potential to “boost” the ignited flame, leading to faster flame propagation rates in the vicinity of the spark. In most cases, this boosting effect should be avoided as variation in the spark energy level could skew propagation rate comparisons.

APPENDIX B – CONCEPTUAL DESCRIPTION OF IMAGE PROCESSING SOFTWARE

This section describes the functionality of and methods behind the in-house image processing software package purposed for flame propagation rate measurement in the laser-ignited RCM experiments. The software was developed in MATLAB and is based largely on measuring differences between sequential images. It is able to properly identify the captured flame surface over a wide range of conditions – window cleanliness, turbulence levels, framerate, position, focal depth, etc. The software is far from robust, however, and often needs to be tuned to achieve sufficient accuracy. Future users will benefit from an understanding of the concepts upon which the code was constructed, as they will likely have to troubleshoot the software on a semi-frequent basis. As such, it is of interest to present the broader theory behind the software and how it works rather than give a detailed account of all the variables and functions at play – a tedious and far from cogent undertaking.

Premixed flame propagation rate is governed by the speed at which combustion radical species can diffuse into the unburned gases ahead of the flame front. As such, it is highly sensitive to temperature and turbulence levels, which can vary both spatially and temporally in the RCM experiments. It follows that the local propagation rate and direction are often not representative of the other portions of the flame in the domain. It is of interest, then, to capture the average propagation rate over the entire flame surface, rather than simply track the propagation distance with time in one direction. This is achieved in the image processor by measuring the projected flame area onto a given image and equating it to a circle of the same geometric area. That equivalent circle is then used to find the average propagation distance of the flame at the time at which the image was taken. This process is illustrated in Figure 64. In sequence, a propagation distance time history is constructed and a propagation rate can be approximated.

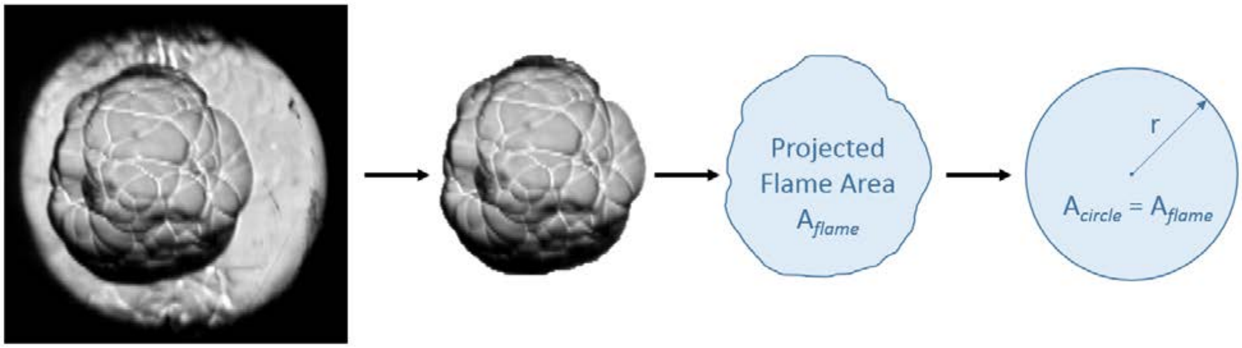

Figure 63. Illustration of the projected flame area method for approximating flame propagation distance, r, with time.

Exactly how the image processor makes these measurements is to be described. The software's executable can be found along with its sub functions in the main "Experiment Processing Package" software folder under "LFS Measurement." The most up-to-date version is LFS3.m. A rudimentary user interface will guide the data input process in MATLAB's command window upon running the script. However, the user must first configure the proper working directories and image locations in the script editor. "LFSdir" is the directory of the folder containing the saved propagation rate measurements that have already been processed. This folder will need to be created in the location of the user's choosing. "Picturedir" gives the address of the folder containing the saved .png images for the experimental trial that the user wishes to process. Both directories are specified in the "INPUTS" section at the very top of the LFS3.m script. Once configured, the software is ready to run.

Upon running the script, the interface prompts the user to enter several describing parameters for the trial under consideration so that it can be paired with the other data previously recorded. Those test descriptions are the experiment index, octane number, and trial number. The experiment index number is a catalogued description that allows the user to easily group trials of a similar sort (e.g. initial pressure/temperature, inert composition). After the user has provided the experiment descriptions, the software will open the first image in the specified directory and request that the frame rate listed on that image be recorded in the command window. The framerate will later be used to calculate the distance the flame has traveled over regular time intervals.

The image processor is concerned only with the images in the folder that have been taken after spark-ignition. Its first order of business, therefore, is to find the image in which the spark has been captured. It does so by taking the sum of the light level (0-255) of all pixels in the image and comparing that sum to that of the previous image. If the difference exceeds the specified threshold, the processor *guesses* that the current image is that in which the spark is captured. It then opens that image for the user to view and requests confirmation that this is indeed the case. If it is not, the user must find the image manually and enter the image number into the command window. The location of the spark in the image is also recorded to serve as an anchor point for the propagating flame for reasons that will be described later in this section.

Next, a pixel to area conversion factor must be determined. This is not a consistent parameter as the size of the projected image can change depending on the alignment of the optics and the adjusted focal length of the camera lens. Physically, however, the size of the chamber's viewport does not change and thereby provides a convenient calibration tool. The processor finds the perimeter of the window and creates a binary image in which every pixel inside of the window projection is given a value of 1. A summation of the binary pixel values (0-1) in this image gives the projected area of the window in number of pixels. This is then used in combination with the known viewport area ($r = 16.12$ mm) to calculate the pixel to area conversion factor which becomes a central parameter to estimating the propagation distance with time.

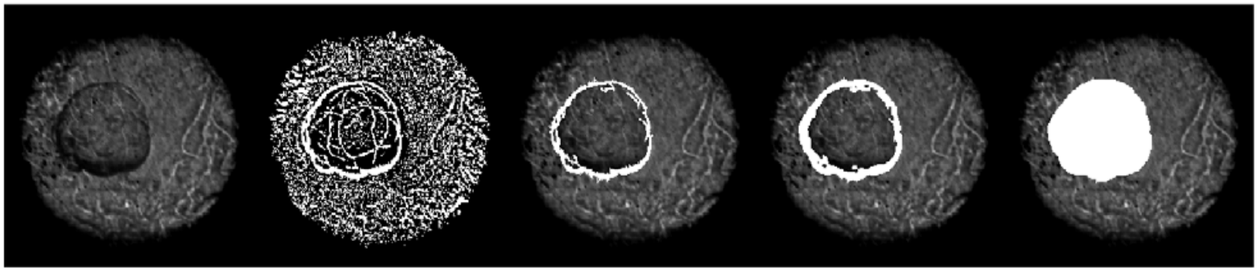

Figure 64. Sequence of Schlieren images depicting the process of identifying the flame surface and determining the total projected flame area onto the image.

The projected flame area in each image in the sequence must now be found through a multi-step procedure. The processor keeps the user informed by opening an intermediate product image after each operation, as depicted in Figure 65. Identifying the flame surface weighs largely on matrix manipulation, as the images are stored in MATLAB as spatial matrices of the pixel light level. The processor begins by comparing the current image to the previous one – literally subtracting one matrix of pixels from the other and then amplifying their differences. Doing so captures the differences brought on by the propagation of the flame, but also by turbulence in the surrounding medium as shown in the second image of Figure 65.

To differentiate the flame surface from the surrounding turbulence, the software first searches for the portion of the difference image that is most dense (i.e. has the highest concentration of “on” pixels). It then searches for continuity between the location of the densest region and the surrounding pixels to eliminate any illuminated pixels that are discontinuous from the flame surface. The result is the collection of illuminated pixels that the software believes to be the projected flame perimeter, as shown in image 3 of Figure 65. This operation is the most prone to error and can result in the complete misidentification of the flame surface if the densest region of the difference image is *not* in fact part of the flame. Misidentification occurs somewhat frequently, but is easily corrected for in post processing so long as the flame is properly identified in the first 5 images and in approximately 50% of the entire set.

It is often the case that the isolated projected flame perimeter does not form a closed loop with itself – that is, it was discontinuous in the previous operation. This loop must be closed prior to performing the final flame area filling procedure. To do so, the software measures the average distance of the pixels forming the flame perimeter to the previously recorded laser spark center anchor point. It then begins to search for pixels that are within that distance from the center that may have been eliminated in the previous operation on the grounds that they were not continuous with the densest region. After bringing those pixels back into the difference matrix, it ensures continuity with the rest of the flame with a local filling procedure and forms a closed loop. Note that this step is performed regardless of whether a closed loop was originally formed or not.

The primary flame area filling procedure can now be performed. Any “off” pixel that is bound on both sides in the x or y directions by “on” pixels is considered a part of the projected flame area, as represented in the last image of Figure 66. This flame area is converted to a circle of equivalent area, the radius of that circle is recorded as the average propagation distance, and the processor moves on to the next image in the sequence.

Upon completion, the resulting propagation distance time history can be quite noisy. It is the job of the post processor to eliminate measurements that appear to be non-physical or indicative of a misidentified flame surface (i.e. they exhibit significant difference from the previous measurement). This is accomplished through comparison of the current measurement with a predicted value for that measurement. The prediction is based on the value and slope of the previous two measurements that have come within a threshold value of their own predictions. If a measurement is substantially different from the predicted value, it is eliminated from the data set, as depicted in Figure 66.

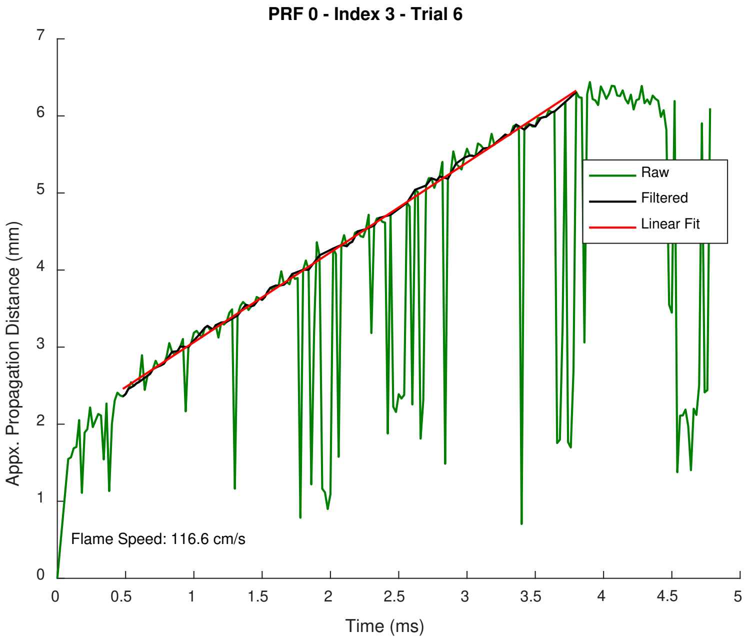

Figure 65. An example of the post-processor's filtering scheme for a case in which the image processor misidentified the flame surface frequently. The raw measurements are presented in green. The measurements that are determined to be accurate by the post-processor are shown in black. A linear regression approximates a constant propagation rate in red.

This procedure weighs heavily on the initial measurements that are taken just after ignition, as those initialize the slope that the post-processor uses to assess the quality of the measurements that follow. For this reason, it is of crucial importance that image processor properly identify the flame surface in at least three sequential images at the beginning of the test. The post-processor will prompt the user (whom is assumed to be smarter than it) to ensure that this is the case. If it is not, the user is given the power to select a different start time for which they deem to have more accurate measurements. Similarly, measurements can be trimmed from the end of the test or the trial can be marked as unsuccessful altogether. These measurement trimming functions are also depicted in Figure 66, with portions of the raw data clipped on both sides. With all non-physical measurements eliminated, the propagation distance time history is fitted with a second order polynomial to eliminate noise. Flame stretch and burned density corrections are then applied, as described in §3.4.

APPENDIX C – BEST PRACTICES FOR REACTIVE MIXTURE FORMATION

The consistency and quality of collected RCM data weigh most heavily on the degree of accuracy to which the test gas mixtures can be formed. Confidence in experimental results is pillared by confidence in the composition of the tested gases, and though precise mixture formation may seem lowly compared to the bigger picture research objectives, ensuring that care is taken during this process will spare the future researcher the headache, confusion, and frustration of interpreting non-physical results for months on end until he or she finally decides that it would be easier to just rerun the entire data set. If there could only be one takeaway from the graduate research experience, it would be the ability to identify bad data on the grounds of careless experimental methods. This section hosts a brief discussion on how best to form gas mixtures using the RCM mixing tanks and manifold apparatus, inclusive of potential mistakes that could compromise the quality of a data set and safety concerns specific to working with highly reactive gases.

Prior to the summer of 2018, components of a test gas mixture were filled directly into the RCM combustion chamber with their proportions controlled through the monitoring of their partial pressures. Though intuitive and convenient, this method is highly subject to error and should not be employed for future experiments. The reason is threefold. First, temperature plays an equally large role in the measured partial pressure of the constituent gas. The temperature of the RCM combustion chamber is monitored only by a thermocouple mounted on the exterior of the chamber. Given the thickness of the chamber walls, the internal temperature transients brought about by the gas filling procedure go undetected on the external surface and therefore are entirely neglected. This means that the amount of the constituent gas added to the chamber by partial pressure will be determined in part by the amount of time that the gas is allowed to sit before the user deems that the system has reached thermal equilibrium. Second, this method makes it easy to ignore the compounding error of sequential filling and consistency between trials becomes difficult to confirm – especially when one experimental trial behaves radically different from another. Third, and of most significant influence, is the mounting location of the dual-capacitance monometer and the fact that it would be exceedingly difficult to mount it directly to the RCM combustion chamber. The monometer is separated from the combustion chamber by nearly a half meter of tubing, and the effective volume within which the mixture is being formed includes that "dead" volume. When constituent gases are filled sequentially, the gas that is intended to go into the chamber must first push the leftover gas of the previous constituent out of the line and into the chamber. This has disastrous consequences on proportion control.

Consider the hypothetical example of a methane/air mixture filled to 1000 mbar. Should the test require a methane partial pressure of 80 mbar and methane is to be filled as the final constituent in the sequence, it is possible that the 80 mbar of methane is only just enough to displace the leftover oxidizer in the line. Here the global proportion of the filled mixture is as intended, but the mixing restriction that the dead tubing volume imposes results in nearly none of the methane actually reaching the chamber. Gases can be evacuated upstream of the transducer, but if they are vacuumed out of the tubing that runs to the chamber, the partial pressures of the previous constituents will be affected to a similar degree. Further, one could propose mounting the monometer directly to the chamber, which would be valid solution should that transducer somehow be closed off during the execution of the experiment to protect it from extreme pressures and temperatures.

In summary, the direct partial pressure fill method should be avoided unless absolutely necessary. Only if the RCM chamber is modified to allow for internal gas temperature and local pressure monitoring could this method be considered legitimate. To maximize composition accuracy and consistency, test gas mixtures are now formed in bulk with both fuel and oxidizer present in the RCM mixing tanks.

Prior to the identification of flaws in the direct fill method, these tanks were only used to create gaseous blends of fuels that are liquid under atmospheric conditions. However, their internal thermocouples and directly mounted pressure transducers make them the ideal alternative to the direct fill method. Further, the large tank volumes can supply approximately 20 RCM experimental trials, eliminating the possibility of inconsistency in mixture composition among replicate trials for a given experiment. A prevalent disadvantage of the mixing tanks compared to the direct fill method is the inability to make quick modifications to the mixture composition. The tank filling procedure takes about an hour and gases must be allowed to sit at high temperature to ensure an adequate level of homogeneity has been achieved prior to use. These are described in more detail in [18,33]. Here, brief instructions on how to use the tanks with both liquid and gaseous fuels will be presented.

The mixing tanks must be completely evacuated prior to filling. Tank heaters should be set to the temperature at which the user intends to fill, which must be above the condensation point for the fuel at the final tank pressure. Ensure that the liquid fill port gasket is in good condition and begin to vacuum out the unwanted gases. Once sufficient vacuum is achieved, gases are filled sequentially – starting with the fuel and ending with the oxidizer.

The crux of the mixing procedure is accounting for temperature transients during filling. Future researchers are encouraged to use tools similar to the tank fill assist functions built into the

“PRFBlendCalculator_ASTM_O2inTank.m” executable in the “Experiment Processing Package” main folder. Simply waiting for the internal tank temperature to return to what it was before the last constituent was filled is an absolute waste of time. Just think about the thermodynamics a little bit and save yourself much frustration. The tank fill assist function employed in this study allows the user to repeatedly input new tank temperatures and accounts for the partial pressure changes that result. It also aims to reduce compounding error by treating each constituent independently during the temperature correction procedure. As an example, a 21% oxygen and 79% nitrogen blend is to be mixed with target tank pressure of 1000 mbar. Nitrogen is filled first, slightly overshooting the target of 790 mbar for a pressure of 796 mbar. The tank temperature after filling is 30 °C. The target pressure for oxygen was originally 1000 mbar, to result in a partial pressure of 210 mbar. However, the 6 mbar overshoot of the nitrogen must be accounted for. Users might be tempted to simply add 6 mbar to the final target pressure – 1006 mbar. This is wrong. In order to achieve the 21%/79% balance, the final target pressure for the oxygen must be 1007.5 mbar (796 mbar nitrogen is 79.1% of 1006, but 79.0% of 1007.5). This distinction may seem like splitting hairs, but once temperature transients are considered, these differences add up. The tank fill assist easily handles these tedious calculations that would otherwise have to be done on the fly.

You, the future researcher, will surely find yourself in the situation where you are filling a mixture constituent, knowing the target fill pressure for the current tank temperature, but just before completion, the tank temperature jumps a degree. What do you do? Quickly punch out the calculations on your phone? Sure. Do that. After you have done that fifteen times, fudged a few calculations, and had to vacuum back the tank in frustration, give the tank fill assist code a try. It is real simple thermodynamics and I’m sure you can build your own, if you cannot get the current one to work for your application.

As an added bonus, the tank fill assist records the fill pressures and temperatures of each mixture constituent during the filling procedure. This allows for precise calculation of the stoichiometry and better estimation of the ratio of specific heats of the mixture as a function of temperature. The tank fill assist outputs temperature and pressure matrices with this data that can be imported directly into the main executable of the “Experiment Processing Package” folder.

APPENDIX D – DATA PROCESSING SOFTWARE PACKAGE

Surely of interest to future researchers will be the experimental data processing software package that was built on the MATLAB platform. The software was purposed to streamline data processing procedures and minimize the effort required to analyze trends in the greater dataset. Prior to its construction, output data from the DAQ was recorded in CSV files and paired with handwritten notes about the initial conditions and manually measured test parameters (e.g. piston offset, peak pressure). Performing a sensitivity analysis on trends in the data was cumbersome to the point that it was often avoided. With this newly developed MATLAB package, test parameters are measured and recorded along with output data from the DAQ automatically and saved in a file format that is standardized such that the entire dataset can be analyzed with ease. Future researchers are encouraged to use the software as it has proved to be invaluable to boosting productivity, reducing frustration (though at times sourcing frustration), and developing a more sophisticated understanding of the results. In fact, the TDC condition grouping method, discussed in §3.1, would not have been possible if not for the MATLAB data processing package. That said, should researchers choose to use the software in future studies, they will likely need to modify the functions to fit their applications. This section provides an account of the processing package's main executable, the functions that compose it, and the strategies imposed to computationally manage large datasets.

The main executable is titled "ExpDataProcessing_EXE.m" and can be found in a folder titled "Experiment Processing Package" on the shared hard drive of the RCM computer. If for some reason that folder is missing or corrupted, contact the author for access. That executable is partitioned into a number of different sections within the script which will soon be reviewed. It functions on a simple infrastructure of two folders named “csv” and “mat” that the user must initialize in their directory of choice. When running experiments, output data from the Picoscope interface should be saved in the “csv” folder in the CSV format. After the user provides the required details about the experiment, the primary MATLAB executable will search for the specified CSV file in that folder and open it for processing. Once complete, data is saved in MAT format in the “mat” folder located in the same directory.

The first section of the executable script is the only one that requires user input. Figure D1 features a snapshot of the portion of the script in which this is done. Here, “workingdir” is the directory in which the “mat” and “csv” folders are located (user’s choice). “in-filename” is the name of the CSV file that corresponds with the data to be processed. “ExperimentName” is less crucial to processing, but should be specified as it can be useful later for automatic legend entry functionality. The “OctaneNumber,” “PFill,” and “TFill” entries can be copied from the tank fill assistant in the “PRFBlendCalculator_ASTM_O2inTank.m” program, which is discussed briefly in Appendix C. These entries are used to determine the composition of the test gas and stoichiometry by using the measured pressures and temperatures of the tank after filling individual constituents. Note that they will only change if the mixture in the tank changes. “ExperimentIndex” and “TrialNumber” are used to denote specific test conditions and individual replicate trials for that set of conditions. In this study experiment indices refer to specific initial conditions inclusive of starting temperature, pressure, and inert composition. “VacuumPressure,” “FillPressure,” “InitialTemperature,” and “ DrivePressure” refer to the pressure that the combustion chamber was vacuumed down to prior to filling of the new charge, the initial pressure to which the chamber was filled, the external chamber temperature at the time of the test, and the pressure to which the RCM bellows were charged to respectively. “PulseEnergy” is the energy output measurement from the

Ophir Starlab DAQ. As of now, it is not possible to interface Starlab with MATLAB, and the measurement must be inputted manually. “SpecialConditions” and “Preignition” flags can be used to mark experiments in which abnormal combustion behavior was observed (e.g. preignition or a double-spark).

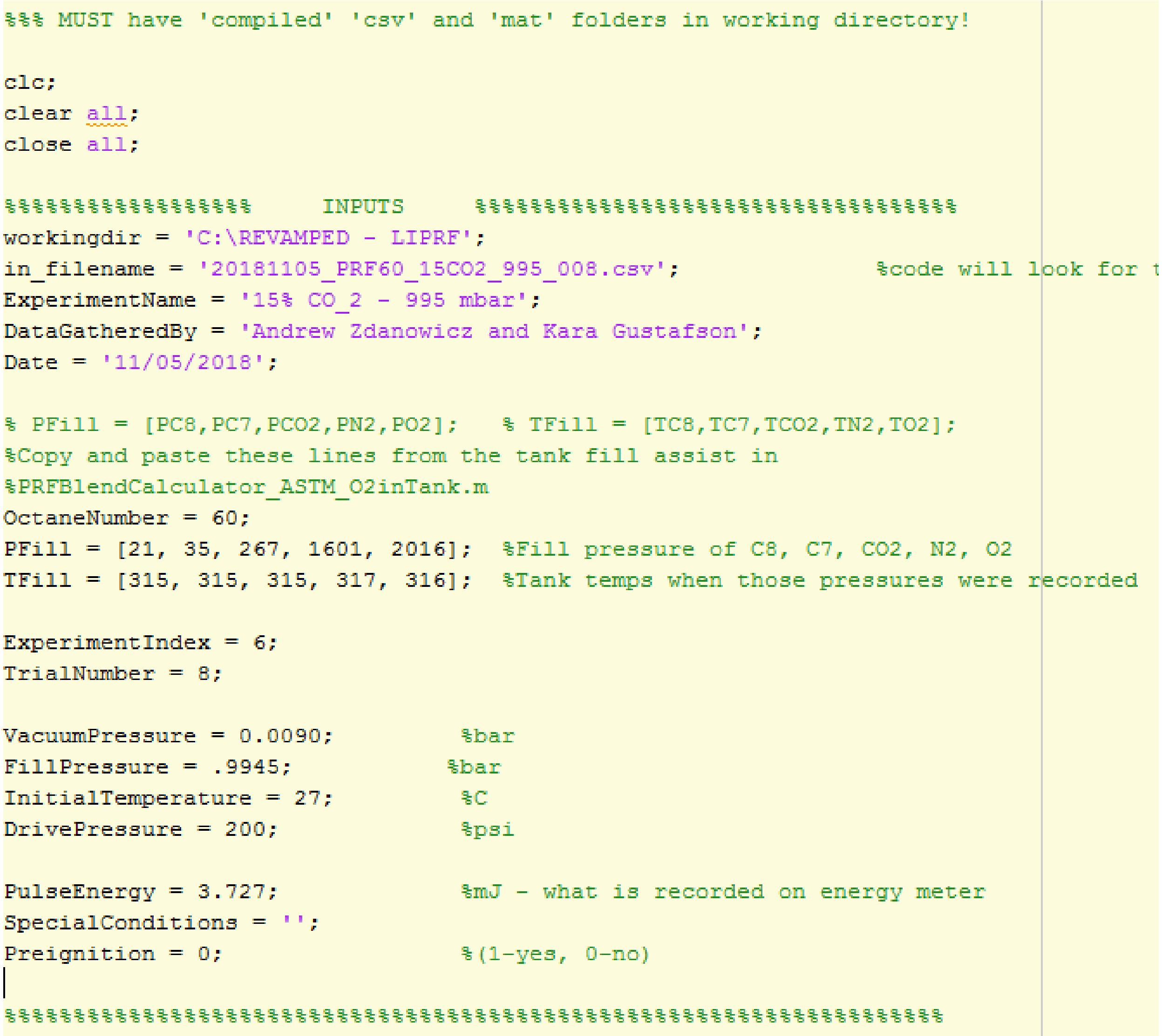

```
%%% MUST have 'compiled' 'csv' and 'mat' folders in working directory!

clc;
clear all;
close all;

%%%%%%%%%%%%%%%%%%     INPUTS     %%%%%%%%%%%%%%%%%%%%%%%%%%%%%%%%%%%
workingdir = 'C:\REVAMPED - LIPRF';
in_filename = '20181105_PRF60_15CO2_995_008.csv';             %code will look for t
ExperimentName = '15% CO_2 - 995 mbar';
DataGatheredBy = 'Andrew Zdanowicz and Kara Gustafson';
Date = '11/05/2018';

% PFill = [PC8,PC7,PCO2,PN2,PO2];   % TFill = [TC8,TC7,TCO2,TN2,TO2];
%Copy and paste these lines from the tank fill assist in
%PRFBlendCalculator_ASTM_O2inTank.m
OctaneNumber = 60;
PFill = [21, 35, 267, 1601, 2016];  %Fill pressure of C8, C7, CO2, N2, O2
TFill = [315, 315, 315, 317, 316];  %Tank temps when those pressures were recorded

ExperimentIndex = 6;
TrialNumber = 8;

VacuumPressure = 0.0090;          %bar
FillPressure = .9945;            %bar
InitialTemperature = 27;          %C
DrivePressure = 200;              %psi

PulseEnergy = 3.727;              %mJ - what is recorded on energy meter
SpecialConditions = '';
Preignition = 0;                  %(1-yes, 0-no)

%%%%%%%%%%%%%%%%%%%%%%%%%%%%%%%%%%%%%%%%%%%%%%%%%%%%%%%%%%%%%%%%%%%%
```

Figure 66. Screenshot of the user input section of the MATLAB data processing executable script.

Once these inputs are filled, the script can be run. The processing functions from this point on are performed automatically and are more or less self-explanatory. Nevertheless, a quick description of what the code is doing will surely assist potential trouble shooting efforts.

The code first determines an appropriate name for the file to be saved based on the octane number and experiment index specified. It then uses a function named “findphi.m” with the “PFill,” “TFill,” “OctaneNumber” inputs to determine the equivalence ratio of the test. This functionality was included after the realization that φ can vary as much as 10% if the temperatures of the mixing tank are not carefully monitored during the mixing procedure (see Appendix C). The function is specific to PRF blends and will have to be modified if other fuels are to be used.

Next, the code finds the specified CSV file in which the experimental data was saved. It sorts the recorded time, piston position, pressure, and photodiode data into the appropriate arrays. Measurements are calibrated using the specified initial pressure and temperature along with several calibration constants that should remain unchanged.

Piston offset is the first experimental parameter to be measured. The function “FindOffset.m” compares the times at which each respective piston reaches a specified fraction of its stroke. This operation is done over a multitude of points when the pistons are roughly halfway to TDC and the resulting data is averaged to give an output piston offset measurement. This function is robust, but may fail if the format of the output CSV files from the DAQ is modified.

Ignition timing is next found using the “FindLaser.m” function. The function looks for a voltage spike in the photodiode channel denoting the firing of the laser and identifies that as the time of ignition. The time of ignition is then compared to the timing of the pistons reaching TDC, given by the local pressure maximum. Several output variables are the result: “LasTimeATDC” as indicating the relative timing of TDC and ignition, “Pcomp” as the peak compression pressure, “PLas” as the measured pressure at the time of ignition.

Raw pressure measurements from the charge amplifier are then filtered by the “filterme.m” function. Future users are encouraged to experiment with the filter constants contained within this function. The current settings were determined to best capture the behavior of interest while removing the oscillations that impeded derivation of AHRRs.

AHRR data is then calculated using the "ahrrcalc_corrected.m" function. This function uses the determined mixture composition and measured pressure-time data to estimate the ratio of specific heats and calculate an AHRR. It is also highly specific to the PRF blend experiments, and is only capable of calculating the specific heat ratios of mixtures containing isooctane, n-heptane, carbon dioxide, nitrogen, and oxygen. Future users will have to build their own correlations of specific heat and temperature if different gases are to be tested. Nist.gov is an indispensable resource for this purpose. A moving average is last applied to the output AHRR data by the function "filterme_mvavg.m."

Early on, the idea to run a fast Fourier transform on the pressure data was suggested as a way of possibly characterizing the knock events. This functionality was built into the software with the "fftcalc.m" function, but was not used extensively in this study.

With these operations complete, a new file containing all of the initial conditions, raw data, processed data, and measurements for the individual experiment is saved in the specified "mat" folder. The data is saved prior to a tiled figure appearing with the calculated pressure and AHRR profiles. Measurements of the flame speed and the f_{EGAI} can be made next, but are done using separate scripts. Flame speed measurement procedure is described in Appendix B. F_{EGAI} is determined using the "fEA_EXE_experiments_superimposed.m" script found in the "fea" folder of the main "Experiment Processing Package" directory.

The f_{EGAI} measurement code requires the user to enter the name of the saved MAT file that was created with the main processing software. Upon running the script, a figure will appear that depicts the derived AHRR profile along with the code's best guess as to where EGAI occurs. The command prompt then displays the calculated *f*$_{\mathrm{EGAI}}$ that corresponds with the shaded area under the AHRR profile displayed. Note that the deconvolution of the AHRR profile, as described in §3.3, has not yet been performed and requires user interaction. The code first asks if the *f*$_{\mathrm{EGAI}}$ should be overridden to a value of 0. If not, the user enters "0" for "no" and the prompts continue. Next, the user is asked if they would like to "Override fEA start time? Enter 0 if no." If the code's first guess as to where EGAI began was demonstrably wrong, the user can override the EGAI start time here by entering the time value at which they believe corresponds with EGAI. Similarly, the user is prompted to change the EGAI end time. Upon doing so, the plot updates and now shows the deconvolution of the AHRR profile. This process is described graphically in Figure D2.

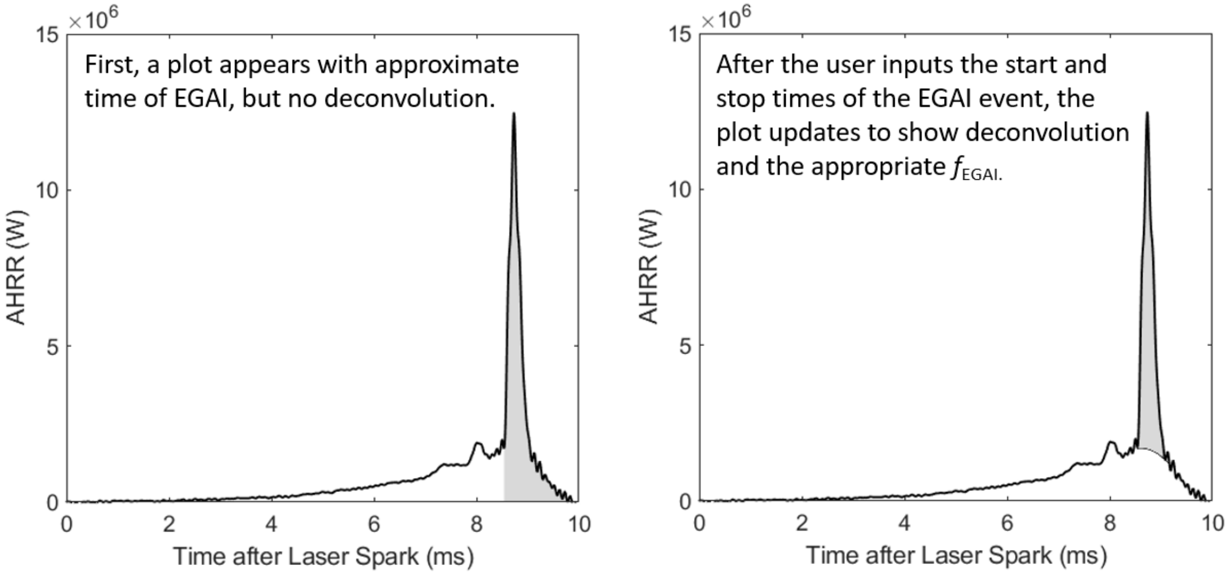

Figure 67. Illustration of the iterative steps of the *f*$_{\mathrm{EGAI}}$ evaluation code.

The process of specifying EGAI start and stop times can be iterative. Once the user is satisfied, they enter "0" for the override prompts and then "1" for the "would you like to save?" prompt. Doing so modifies the original MAT file containing the experiment data with the additional field of *f*$_{\mathrm{EGAI}}$.

The result of all of this being repeated for each individual experiment, is a massive folder containing all of the MAT files and collected experimental data. Note that scripts can easily be written to modify how calculations were made and update the dataset each file in the folder. However, the size of the dataset eventually becomes too large for an ordinary computer to load and analyze all at once. Techniques to condense relevant data into manageable matrices were developed in response.

Two files of critical importance here are the “addintocondensed.m” and “condenseddatarecord.mat.” The former allows the user to initialize a new matrix corresponding with some parameter of interest and then pan through each file in the dataset to extract that parameter and save it accordingly. Doing so significantly reduces computational expense when analyzing the greater dataset. Condensed data matrices are saved in the “condenseddatarecord.mat” file specified. A description of the condensed data matrix structure here is necessary and a screenshot of an example matrix is shown in Figure D3 for this purpose.

Each condensed data matrix represents a single measured parameter evaluated over the entire data set. Different experimental conditions are delimited by row and the first three columns of every matrix represent the experiment’s ON, index, and number of replicate trials. Thus, in the compressed pressure condensed data matrix shown in Figure D3, row 1 corresponds to an experiment featuring an ON of 0 with an experiment index 1 (15% CO_2 included in the inert) wherein 10 replicate trials were performed. To the right of those three columns is the recorded data for that parameter over those 10 trials.

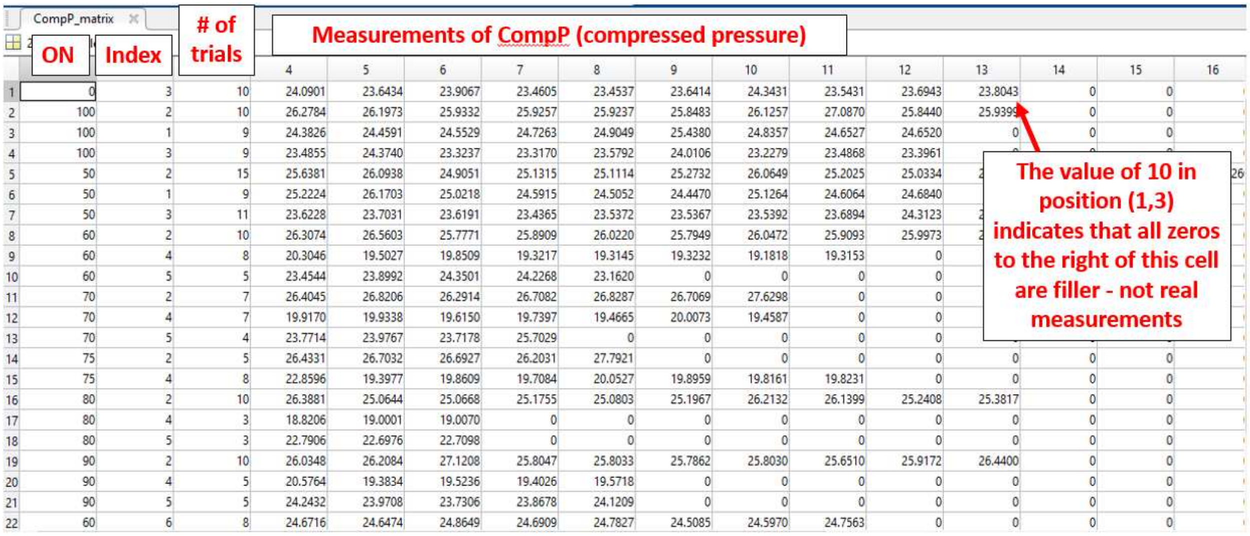

Measurements of CompP (compressed pressure)

	ON	Index	# of trials	4	5	6	7	8	9	10	11	12	13	14	15	16
1	0	3	10	24.0901	23.6434	23.9067	23.4605	23.4537	23.6414	24.3431	23.5431	23.6943	23.8043	0	0	
2	100	2	10	26.2784	26.1973	25.9332	25.9257	25.9237	25.8483	26.1257	27.0870	25.8440	25.9399	0	0	
3	100	1	9	24.3826	24.4591	24.5529	24.7263	24.9049	25.4380	24.8357	24.6527	24.6520	0	0	0	
4	100	3	9	23.4855	24.3740	23.3237	23.3170	23.5792	24.0106	23.2279	23.4868	23.3961	0	0	0	
5	50	2	15	25.6381	26.0938	24.9051	25.1315	25.1114	25.2732	26.0649	25.2025	25.0334				
6	50	1	9	25.2224	26.1703	25.0218	24.5915	24.5052	24.4470	25.1264	24.6064	24.6840				
7	50	3	11	23.6228	23.7031	23.6191	23.4365	23.5372	23.5367	23.5392	23.6894	24.3123				
8	60	2	10	26.3074	26.5603	25.7771	25.8909	26.0220	25.7949	26.0472	25.9093	25.9973				
9	60	4	8	20.3046	19.5027	19.8509	19.3217	19.3145	19.3232	19.1818	19.3153	0				
10	60	5	5	23.4544	23.8992	24.3501	24.2268	23.1620	0	0	0	0				
11	70	2	7	26.4045	26.8206	26.2914	26.7082	26.8287	26.7069	27.6298	0	0				
12	70	4	7	19.9170	19.9338	19.6150	19.7397	19.4665	20.0073	19.4587	0	0				
13	70	5	4	23.7714	23.9767	23.7178	25.7029	0	0	0	0	0				
14	75	2	5	26.4331	26.7032	26.6927	26.2031	27.7921	0	0	0	0	0	0	0	
15	75	4	8	22.8596	19.3977	19.8609	19.7084	20.0527	19.8959	19.8161	19.8231	0	0	0	0	
16	80	2	10	26.3881	25.0644	25.0668	25.1755	25.0803	25.1967	26.2132	26.1399	25.2408	25.3817	0	0	
17	80	4	3	18.8206	19.0001	19.0070	0	0	0	0	0	0	0	0	0	
18	80	5	3	22.7906	22.6976	22.7098	0	0	0	0	0	0	0	0	0	
19	90	2	10	26.0348	26.2084	27.1208	25.8047	25.8033	25.7862	25.8030	25.6510	25.9172	26.4400	0	0	
20	90	4	5	20.5764	19.3834	19.5236	19.4026	19.5718	0	0	0	0	0	0	0	
21	90	5	5	24.2432	23.9708	23.7306	23.8678	24.1209	0	0	0	0	0	0	0	
22	60	6	8	24.6716	24.6474	24.8649	24.6909	24.7827	24.5085	24.5970	24.7563	0	0	0	0	

The value of 10 in position (1,3) indicates that all zeros to the right of this cell are filler - not real measurements

Figure 68. Example condensed data matrix for compressed pressure measurements of the full data set. Shown for matrix structure description.

What is crucial to this data structuring technique is that the matrix position of a measurement corresponding to a specific experiment remains the same for all condensed matrices. That is CompP_matrix(1,4) and LasTimeATDC_matrix(1,4) refer to the compressed pressure and ignition timing of the same experiment. The trialmatrix(1,4) returns the value of 1, so this experiment is PRF 0, index 1, trial 1.

It is not argued that this is the best way to structure the condensed version of the full dataset, but it is effective. Matrices are filled automatically via scripts, such as "addintocondensed.m." This script opens the individual MAT files, finds the relevant parameters, identifies the matrix position corresponding to that file, and fills the matrix cell appropriately. Further, such a platform allows sensitivity analysis to be performed with ease.

The author recognizes that the "Experiment Processing Package" folder is a bear. There are 128 scripts, functions, and saved files, but many of those files are purposed for specific plots or operations that will be of little interest. Rest assured that the core of the program is just a few simple operations. Nonetheless, future researchers are encouraged to contact the author with questions they may have regarding the data processing package and its auxiliary functions.